Probing local thermodynamical properties of a nanomechanical resonator in a scanning electron microscope

Thesis submitted to the University of Nottingham for the degree of
Doctor of Philosophy, 4th July 2023.

Clément Chardin

Student ID: 20124301

Supervised by

Andrew Armour
Pierre Verlot

Abstract

Micro and nano-mechanical devices have attracted increasing interest from scientists and engineers over the last few years because of their promising fundamental and technical applications. Their extremely low masses make them very sensitive to noises and forces, making them perfectly suited to act as detectors of weak forces or for testing new physics and potentially bringing quantumness towards the macroscopic world. Both the fabrication processes for producing nanomechanical resonators and the detection schemes used to monitor their motion have greatly improved recently. In particular, unprecedented sensitivities have been achieved with optomechanical detection systems and ultra-high mechanical quality factors.

In this thesis, we explore a detection method based on the interaction between a nanomechanical resonator, in the form of an InAs nanowire, and the electron beam inside a Scanning Electron Microscope (SEM). Although SEMs were first used as nanomechanical motion sensors more than 20 years ago, there has been a renewed interest in their use in the last few years as the back-action mechanisms are better understood thanks to related work on optomechanical systems and the potential of the technique has been demonstrated more clearly. This work extends the SEM measurement technique to provide "hyper-spectral images", i.e. local information on the dynamics of the resonator obtained by tracking several mechanical modes simultaneously as the SEM beam is moved across and along the nanowire. This new technique provides important new insights into unique features of the SEM-mechanical system: we describe how it can be used to study three aspects of the interplay between the dynamics of the nanowires, the heating supplied by the electron beam and the structural properties of the resonator. Firstly, we show that the SEM is a strong source of heating, causing a remarkably strong temperature gradient inside the nanowire, driving it far from equilibrium. Secondly, we explored the properties of self-sustaining oscillations in the nanowire which the SEM can induce in much more detail than has been possible before. Finally, we also investigated the severe irreversible structural changes of the nanowire that the SEM beam causes via etching. Theoretical modelling provided valuable insights into the observed behaviours, but could not capture all of the features. Most significantly, the experiments and modelling together provide valuable evidence that localised defects within the wire can play an important role in mediating its response to the SEM. This could lead to the SEM being used to detect structural defects inside nanowires.

Acknowledgements

This thesis would not have been possible without a number of people who helped me and supported me during all this time. First of all, my thesis supervisors Pierre Verlot who took me in and taught me most of what I know in physics to this day, and Andrew Armour who took over after Pierre left the University of Nottingham and brought me a whole lot of invaluable structure and advice, while remaining positive in every situation.

Many of the results presented in this work are the fruit of a collaboration with many people who have my eternal gratitude, most of all Sébastien Pairis and his fairy fingers for his amazing patience, his delicacy when placing an electron beam along a nanowire and for taking me to rugby matches when I visited, and Moïra Hocevar who created sample after sample whenever I asked, but also many other people who I have worked with, Sabine Doucet and Thomas Gilibert, Ludovic Bellon and Alex Fontana, An-Hsi Chen, Jean-Philippe Poizat, Fabrice Donatini, Julien Claudon, and the amazing Aurélie Laurent who did all the paperworks for my missions.

My journey into physics started some time ago, but one of the most important persons I met along this path is Thomas Antoni who was my professor at École Centrale Paris, and gave me the great advice of starting this PhD project. Speaking of professors, I had the opportunity to attend the summer school in Les Houches where lectures where incredibly inspiring and helpful for formalizing some parts of this thesis, especially those given by Eva Weig, Pierre-François Cohadon and Samuel Deléglise.

This PhD was also for me the opportunity to move abroad and discover new cultures and people. The house I shared during a year and a half with Rahul, Daniele, Juan and William was as multicultural as could be, and lead to great discoveries with great people. I'd also like to thank the rugby club of the Nottingham Casuals for welcoming a frenchie among them and making me feel right at home even when I rooted for South Africa in the final. COYC ! A huge thank you to the students of the cold atoms lab in Nottingham for some really nice conversations during lunch breaks, Fabio, Elisa, Bethany, Vilius, Nathan, Sindhu, Tadas, Jamie...

During these years of work, I had up and downs, and I cannot express enough my gratitude to my mother Evelyne, my father Jean and my brother Renaud for their support, their encouragements and their amazing advice. And finally, the biggest thank you to Valérie, who supports me and pushes me forward when I need it.

Contents

List of Figures

Abbreviations

AFM Atomic Force Microscope.
CNT Carbon Nanotube.
CZT Chirp-Z Transform.
DFT Discrete Fourier Transform.
DSP Digital Signal Processing.
FDT Fluctuation-Dissipation Theorem.
FESEM Field-Effect Scanning Electron Microscope.
FFT Fast Fourier Transform.
MBE Molecular Beam Epitaxy.
NEMS Nano-Electromechanical Systems.
NMS Nano-Mechanical Systems.
NW Nanowire.
PSD Power Spectral Density.
RBW Resolution Bandwidth.
RSA Real-time Spectrum Analyser.
SE Secondary Electrons.
SEM Scanning Electron Microscope.
SQL Standard Quantum Limit.
SSA Swept Signal Analysers.
TEM Transmission Electron Microscope.
UQL Ultimate Quantum Limit.
VLS Vapor-Liquid-Solid.
VSA Vector Signal Analysers.
WGMC Whispering Gallery Mode Cavity.

Chapter 1

Introduction

Miniaturization of physical systems has been a huge drive in the development of science and technology in recent decades. Fabrication techniques have tremendously improved, leading to the development of Micro- and Nano-Mechanical Systems (NMS), which contain mechanical resonators with dimensions on the micron scale or below and vibration frequencies in kHz to MHz range. Such devices have important technological applications with the potential to have significant impact on our everyday lives [1]. In science, and in particular in fundamental physics, nanomechanical resonators have been of increasing interest [2, 3]. The exceptional mechanical properties of NMS led to the development of new fields of research, such as exploring the crossover between quantum and classical behaviour in mechanical systems [4, 5] or the fundamental limits of ultra-sensitive measurements [6].

The extremely low mass of NMS which leads to low thermal noise, together with developments in fabrication techniques that facilitate very low levels of dissipation and rapid improvements in detection techniques, have all helped researchers to develop devices with exquisite sensitivities to a range of external forces [2]. These techniques often involve optics, leading to the development of optomechanical systems [7], though electrical detection methods have also been explored, leading to Nano-Electromechanical Systems (NEMS) [4]. Moreover, as we will see later on, nanomechanical systems can be driven far from equilibrium, raising a number of new questions on their dynamics.

In the present thesis we will discuss the dynamics and thermodynamics of a nanomechanical device, namely an indium arsenide (InAs) nanowire, using a detection scheme based on a Scanning Electron Microscope (SEM) whose potential has never been explored in detail. We will begin with a brief history of ultra-sensitive measurements of motion, starting with the origins of optomechanics as a research subject before describing the steps that led to the proposal of this detection method.

1.1 The origins of optomechanics

Light has been identified as the best way to measure distances for a long time. Telemetry originated in the 18th century, and nowadays it lets us know the distance from the earth to the moon with an imprecision of just a few millimetres [8]. However, it was later established that interferometry was the best way to measure a small displacement and its dynamics.

The development of these techniques was led by historically important scientific questions: What is light? What limits the sensitivity of a displacement measurement? The answer to the former is the well-known wave-particle duality of light, which took centuries to be established. The corpuscular aspect, brought forward by Newton [9] and Gassendi [10], is responsible for the dynamical effects of the light-matter interaction, through what was later identified as the radiation pressure. On the other hand, the wave properties of light, formulated by the work of Huygens [11] and demonstrated by Young [12] and Fresnel [13], are responsible for the sensitivity of the interferometric measurement.

The union of these two sets of properties came much later, with Einstein, Planck and others [14], and wave-particle duality is the key to understanding what limits the sensitivity of a displacement measurement. The quantitative study of the limits of sensitivity started during the second half of the 20th century, with the objective of measuring gravitational waves. These waves of the intensity of gravity, predicted by Einstein in 1916 [15, 16] as the effect of accelerated masses of an orbital binary system, deform space-time. On earth, this leads to relative variations in lengths of the order of $\delta L/L \simeq 10^{-22}$. It was realized that for such precise measurements the impact of quantum effects had to be accounted for [17]. Following an enormous effort involving a large team of scientists, an interferometer with sufficient sensitivity was developed and the first confirmed gravitational wave signal was detected in 2016 [18].

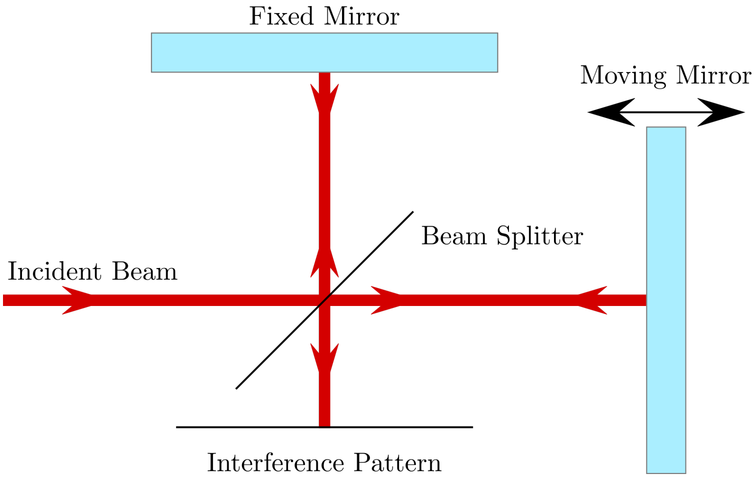

Figure 1.1: Basic schematics of a Michelson interferometer. A beam splitter is used to generate an interference pattern between light reflecting off two mirrors: a movable one and a fixed reference. This provides a sensitive way of monitoring the displacement of the movable mirror.

1.2 Interferometric measurements

An interferometric measurement relies on a coherent light beam, which is reflected off the object whose motion is measured, and interferes with itself, thus creating an interference pattern depending on the position of the reflector. An early example of such a measurement was performed by Michelson and Morley in 1887, with the objective of detecting æther [19], and their method is still in use nowadays.

A Michelson interferometer consists of a semi-reflecting plate which separates an incident laser beam into two arms. Each beam then reflects off a mirror, before they are recombined through the beam splitter and form the interference pattern which depends on the difference of length between the two arms. If one of the two mirrors is moving, its motion can thus be detected. This setup is shown in fig. 1.1.

This measurement relies on detecting the phase difference between the two beams, which varies with the motion of the mirror. As such, the sensitivity of the basic Michelson interferometer is determined by the wavelength, λ, of the beam: the phase has its maximal variation when the mirror moves by $\lambda/2$. This was vastly insufficient for the detection of gravitational waves, which led to the research of means of improving this sensitivity. The first possibility was to increase the size of the arms of the interferometer, since the gravitational waves signal scales with storage time of the light in the arms. However, for obvious technical reasons, there is a limit on the attainable length, which is probably close to the size of the state-of-the-art gravitational waves interferometers (4 km for LIGO). Another possibility is to increase the laser power to improve the performance of the interferometer.

In order to combine both these solutions, a powerful tool was developed: the Fabry-Pérot cavity [20]. It consists of two mirrors facing each other, thus ”trapping” light for an extended period of time before releasing it. This results in an increase in the effective length of the interferometer, or equivalently increases the output signal with the same input power. In other words, the Fabry-Pérot cavity can be seen as a low noise amplifier for optics, and reduces the technical noise of a laser by decreasing the incident power. Fabry-Pérot cavities were used to enhance the sensitivity by the LIGO and VIRGO collaborations in their efforts to detect gravitational waves.

The Fabry-Pérot cavity has also proved a valuable tool in exploring the fundamental limits of sensitivity in optical measurements. To illustrate this, let us first consider a laser beam reflecting from a single movable mirror, as in fig. 1.2a. When the mirror moves by an amount δx, the beam travels an extra distance $2\delta x$ and the phase of the reflected beam is shifted by a quantity

$$\delta\phi^{out} = 4\pi\frac{\delta x}{\lambda}. \tag{1.1}$$

The phase is then sensitive to displacement of the order of half the wavelength λ of the laser.

This sensitivity can be improved by placing a second fixed mirror in front of the first one, thus forming a cavity which supports resonant modes with wavelengths $\lambda = 2L/n$, with n an integer and L the cavity length [21, 22]. These resonances are seen as sharp peaks in the reflected intensity when the laser frequency matches that of one of the modes, $\omega/2\pi = nc/2L$. The figure of merit of a Fabry-Pérot cavity is the finesse of the cavity, defined as the ratio between the free spectral range (i.e. the spectral range between two resonances, $\Delta\omega_{fsr} = \omega_{n+1} - \omega_n$) and the width of each resonant peak: $\mathcal{F} = \Delta\omega_{fsr}/\Delta\omega_c$. It represents the number of round trips a photon will experience inside the cavity before exiting and enhances the sharpness of the peaks and the sensitivity of the measurement of the mirror's displacement, as we will see in the following paragraphs.

Fabry-Pérot measurement with the intensity. To measure the displacement of the end mirror, one can focus on its effects on the reflection of the

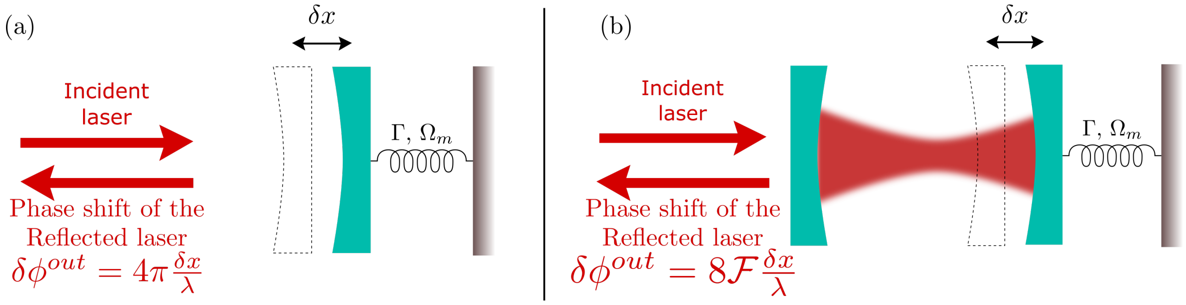

Figure 1.2: (a) Phase shift of a reflected laser beam due to the displacement δx of the reflecting mirror of resonant frequency Ω_m and a damping rate Γ. (b) Fabry-Pérot cavity. The phase shift of the reflected beam due to the displacement of the end mirror is amplified by the finesse of the cavity, and its amplitude as well as that of the transmitted and intracavity fields are modulated.

cavity, as illustrated in fig. 1.2b, or on its transmission which is sharply peaked around the resonances of the cavity. Figure 1.3a highlights how, when the rest position of the end mirror is located at the side of a resonant peak, a displacement $\delta x(t)$ of the mirror will be transduced into an intensity variation. If the displacement is small enough, the amplitude of the modulation measured in the transmission will be proportional to the slope of the intensity profile, which is directly linked to the finesse of the cavity.

Fabry-Pérot measurement with the phase. In many cases it can be preferable to instead have the highest intensity signal, and hence to measure the displacement of the mirror around a position corresponding to the centre of a given resonance. In that case, the derivative of the transmitted (or reflected) beam is null, canceling the sensitivity of an intensity-based measurement. However, it is possible to use the phase of the beam, which varies by 2π from one side of the resonance to the other (see fig. 1.3b). Similarly to the previous case, the transduction factor is the slope on the phase profile, which is proportional to the finesse of the cavity: it can be shown [23] that the phase shift $\delta\phi^{out}$ experienced by the output of the cavity is linked to the displacement of the mirror via

$$\delta\phi^{out} = 8\mathcal{F}\frac{\delta x}{\lambda}. \tag{1.2}$$

Equation 1.2 highlights the importance of maximizing the finesse of the cavity, which is directly linked to the reflectivity and the losses of the mirrors used.

The cavity enhanced method of measurement dates back to the first attempts at interferometric measurements of gravitational waves and lead to various results including the demonstration of the optical bistability [24], the optical spring

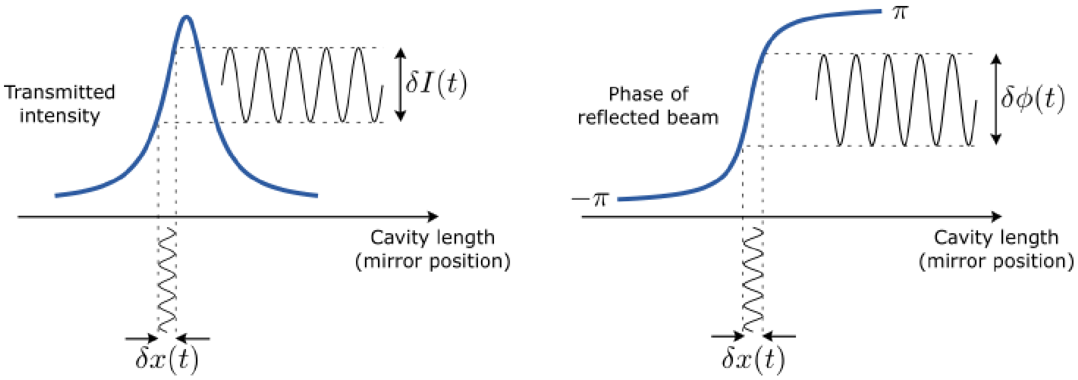

Figure 1.3: Fabry-Pérot transmitted intensity and phase of the reflected beam. The displacement $\delta x(t)$ of the end mirrors define the cavity length and can either be measured on the side of fringe through the transmitted intensity $\delta I(t)$ or at resonance through the phase of the reflected beam $\delta\phi(t)$.

effect [25, 26] or optical cooling [27–29]. More details on Fabry-Pérot cavities and their applications can be found for example in [7].

1.3 Limits of sensitivity

The previous section explains how the sensitivity of the measurement of small displacements can be very significantly enhanced by the use of an optomechanical cavity. However, it still has some limits. Indeed, if the displacement is small enough, Heisenberg's uncertainty principle has to be taken into account. This principle, which sets a lower limit on the product of the uncertainties in position and momentum, becomes relevant when we want to measure position over a finite period of time since reducing the position uncertainty at one instant increases the momentum uncertainty which leads to a higher position uncertainty at later times.

The way in which a measuring device acts to disturb the system being measured is known as back-action. In the case of optomechanics, back-action arises from the radiation pressure force, that is the exchange of momentum between the photons of the probe and the mechanical resonator. One of the main contributions of research in optomechanics is the formalization of the concept of back-action, first by Braginsky [30], and then Caves [31, 32], and later its experimental demonstration [27, 33, 34].

An important limit is the Standard Quantum Limit (SQL) [6], which represents the optimal sensitivity obtained when using a coherent state of light. The SQL is achieved when there is an optimal balance between the noise in the detector itself, which arises from the shot noise of the laser and is prominent at high frequencies, and the back-action of the measurement coming through radiation pressure, prevalent at lower frequencies [35]. The SQL can be beaten by a number of methods, including back-action evading techniques [36] or squeezed states [37] for example. However, other limits exist such as the Ultimate Quantum Limit (UQL), obtained when the squeezing can be optimized at each frequency [38].

It is important to note that the SQL is defined for a conservative measurement. In this case, the thermodynamical state of the system is conserved, i.e. there is no absorption of energy causing heating of the mirrors. The optomechanical measurement is also conservative from the point of view of the measurement probe: the number of photons is conserved during the measurement and there is no loss of information. Most optomechanical experiments aim to achieve this conservative measurement, as we will see in section 1.4.

However, in spite of the best efforts of experimentalists to place their systems in the conservative measurement framework, some losses still occur which require an increase in the probe power in order to maintain the sensitivity of a measurement. This issue becomes more significant as the mechanical resonators tend to the nanometric scale and is symptomatic of the difficulties involved in adapting the Fabry-Pérot cavity to those scales. The consequence is that the mechanisms of back-action are now multiple whereas there was only one in a conservative measurement. In an interferometric measurement, these effects are known and involve for example the photo-thermal effect [33, 39] and a lowered quantum efficiency of measurement [40], and lead to a degraded optimal sensitivity, when compared with a conservative measurement.

1.4 Innovations in optomechanical systems

In order to explore the limits of physics, researchers have deployed a number of innovations for both the mechanical resonator part of their experiments, and for the cavities. To obtain higher and higher sensitivities and overcome the thermal noise of the resonator, the general trend was to miniaturize the system, in order to have lower masses and higher frequencies. We can make a distinction between two types of systems, depending on how they were designed: top-down or bottom-up. Comparisons between these two designs can be found for example in [2] or [4].

Top-down systems. These systems are created by defining a set of criteria they should match, and tailoring a system accordingly using nanofabrication techniques. These objects usually have very low dissipation rates and are very well coupled to their probe. However, they often have a comparatively large mass, and the strength of the thermal noise force in these systems typically remains a lot higher than for bottom up systems. They require a demanding experimental environment: high vacuum, cryostats, etc. They are often used in fundamental physics research such as ground state cooling or in efforts to produce non-classical states.

A good example of a top-down system is the high-stress nano-string that has been used to reach unprecedented mechanical quality factors, a key figure of merit in nano-mechanics (see section 2.1). The development of Si_3N_4-based resonators was a major advance [41, 42], and allowed for quality factors as high as a billion [43]. High-stress nano-strings have been used to demonstrate measurement imprecision below the standard quantum limit [44] or to show evidence of classical noise squeezing in a driven nanomechanical mode [45].

Similarly, high internal stress materials have been used in 2D resonators, and membranes have been used either as the end mirror of optical cavities by increasing their reflectivity with a photonic crystal [46], or as a membrane-in-the-middle configuration [47]. These resonators have shown mechanical quality factors as high as 10^8 [48–50] and were used for example in the experimental observation of radiation pressure shot noise [51].

Even though the high-stress membranes with embedded photonic crystals have massively improved the optical and mechanical properties available to optomechanical measurements, they were not yet able to step into the quantum regime. Indeed, an upper bound was set on the product of their quality factor and resonant frequency $Qf < 6 \times 10^{12} Hz$, due to the acoustic mismatch between the membrane and its substrate [52]. An approach was proposed to address this issue by using the so-called "trampoline drum" system, consisting of four thin strings suspending a small and light central pad [48, 50]. However, another approach proved to be more efficient: the so-called "soft clamping" of the membrane, using a phononic crystal to prevent the vibrational energy of the modes to exit the resonator, leading to Qf product as high as $10^{14} Hz$ [53], opening the way to quantum back-action evasion [36], measurement below the standard quantum limit [54] and phonon counting near the ground state [55], among others.

In addition to soft clamping, other techniques were developed to further improve the Q-factor of nanomechanical resonators: strain engineering and dissipation dilution [43]. By colocalizing strain and mechanical motion within a non-uniform phononic structure, exceptionally high quality factors have been reached [56]. Note that the same type of techniques have also been used for 2D membranes [57, 58].

Another system worth mentioning is the Atomic Force Microscope (AFM) and its cantilever, since it is one of the most used imaging techniques. Since it appeared in 1986, AFM has become one of the most precise imaging technologies [59], reaching atomic [60], then subatomic [61] resolution. It allowed the manipulation of single atoms [62], probed chemical structures of molecules [63, 64] and allowed imaging in biologically relevant environments [65]. Even though it is not usually used for fundamental physics research, it heavily relies on optomechanics. Indeed, it uses the measurement of the mechanical resonant frequency of a cantilever, which is shifted due to the interaction with the sample under study. This resonance is usually measured through the deflection of a reflected beam detected with a quadrant photodiode, thus resolving the displacement of the cantilever. The interaction with the laser leads to strong photothermal effects, the understanding and control of which is critical. These effects have been studied for a long time [66, 67], including in a liquid environment [68–70], in order to improve the performance of the AFM. Additionally, the AFM cantilever is a prime system to study thermodynamics of resonators out of equilibrium [71–73], as we will see in section 2.5.

Bottom-up systems. These systems are based on nanomechanical components that are formed in their final shape from their atomic constituents e.g. by a chemical process, rather than by etching away parts of a larger system. Such systems often have very interesting properties which makes them worth studying, and they can be incorporated into an optomechanical set-up to sense their motion. The property of interest is often the very low mass of these objects, which leads to low thermal noise and makes them good force detectors for example [74].

The best example of bottom-up system is the Carbon Nanotube (CNT), which has a mass in the attogram (10^{-21} kg) range. If the first optical [75] and capacitive [76] detection attempts led to modest sensitivity results, more recent improvements in the quality of the samples fabricated (with Q-factors up to 5 million [77]) have allowed for unprecedented force sensitivity in the $zN/\sqrt{Hz}$ range [74, 78], and mass sensors with yoctogram ($10^{-27}kg$) sensitivity [79].

Nanotubes however, present difficulties for the measurement read-out. Indeed, their extremely small size makes it difficult to couple them with a laser, which motivated the use of other detection techniques such as capacitive coupling. Recently, an alternative was proposed, which is to "functionalize" them by adding a nanoparticle close to their tip. This process is performed by focused electron beam-induced deposition [80] and allows for optomechanical measurement [81].

New optical cavities. While the improvement of the mechanical resonator was the object of a lot of research, optical cavities were also subject to a number of changes and innovations in recent years. Some of the main propositions were to use the cavity itself as the mechanical resonator, or to use its evanescent field to couple to an external resonator such as a (possibly strain-engineered) nanobeam.

By coupling light into a spherical or circular cavity, one can excite the so-called whispering gallery mode [82]. Such a system presents a number of mechanical modes distorting the structure of the cavity, directly modifying the optical path length, thus shifting its optical resonance frequency and generating optomechanical coupling. The classes of cavities referred to as Whispering Gallery Mode Cavity (WGMC) include circular cavities [83, 84], spherical cavities [85–87] and toroidal cavities [88, 89]. In particular, the latter allowed demonstration of radiation-pressure driven optomechanical parametric amplification [90], sideband-resolved operation [91] or controllable coupling with a graphene monolayer [92].

Another relatively recent type of cavity relies on photonic crystals, i.e. periodic arrangements of materials with different optical properties, to create a bandgap in which only certain optical modes can propagate. It is possible to insert a defect in the crystal such that light will propagate inside this defect but not out of it. If defects form a line through the crystal, one gets a waveguide [93], which can be used for slow light [94], pressure sensors [95] or bio-sensing [96]. Alternatively, if the defect is localized, for example a missing dot in the crystal, the result is an optical cavity able to reach high quality factors [97]. The optomechanical coupling of such cavity relies on the deformations of the cavity boundaries and the stresses due to its motion. It has been studied both with waveguides [98] and localized defects [99]. The results obtained using photonic crystal cavities include high optomechanical cooperativity [100], topological phonon transport [101] or the study of nonlinear optomechanics [102].

In conclusion, feats of engineering have been deployed to adapt the techniques of optomechanics to the most sensitive devices, with regard to both the mechanical resonators and the optical cavities, and to retain the conservative properties of optomechanical coupling. However, as the dimensions of resonators were reduced below the diffraction limit, it proved to be increasingly difficult. The difficulties of fabrication degraded the optical properties of the samples, and the conservative nature of the measurement was hard to maintain, if only because of diffraction which induces a loss of information.

1.5 SEM as a motion detection tool

In order to avoid the diffraction limit and reduce the detection noises, another detection scheme was proposed, using a focused electron beam to measure the motion of a resonator inside a Scanning Electron Microscope (SEM). This method was first used more than 20 years ago [103, 104], but with the increased understanding of back-action in the optomechanical context, it regained popularity recently with extended goals of fundamental research [105–108]. This is the first cavityless system which does not rely on an electromagnetic resonance, and the measurement system which was used during this thesis. Here, we will briefly explain how the SEM can be used to measure the displacement of a mechanical resonator. The functioning of the SEM itself will be further discussed in section 3.3.

The experimental setup used to turn the SEM into a displacement measurement tool is shown in fig. 1.4. The SEM is used in spot mode, and the Secondary Electrons (SE) – that is electrons arising from a strongly inelastic collision with the material – are detected. It is important to note that this places this measurement in a purely dissipative regime, which raises a number of questions about the thermodynamics of the system.

When the electron beam is placed in a high intensity gradient position (i.e. a position on the edge of the mechanical system so that a small change in position leads to a large change in scattered electron intensity), any displacement δx of the resonator around a position x_0 will be converted into an intensity variation δI_{SE} of the SE emission proportional to its derivative $\partial I_{SE}/\partial x$ (see fig. 1.4b)

$$\delta I_{SE}(t) \simeq \left(\frac{\partial I_{SE}}{\partial x}\right)_{x_0} \delta x(t). \tag{1.3}$$

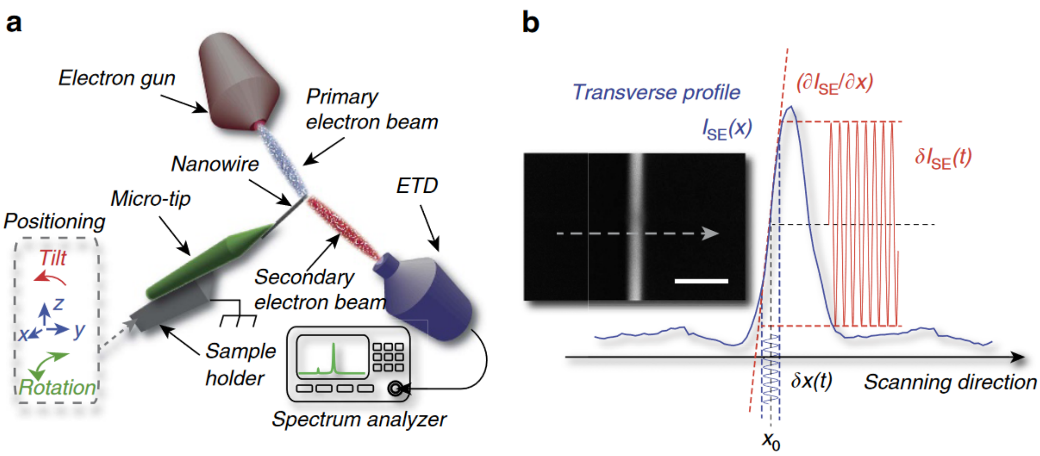

Figure 1.4: (a) Schematic of the experimental set-up. The electron beam is focused onto the nanomechanical resonator, and the SE emission is detected, allowing the measurement of its dynamical motion around its equilibrium position (EDT: Everhart–Thornley detector). (b) Using Secondary Emission for nanomechanical motion detection. The very high contrast of SEM imaging (illustrated here with a 20 nm gold nanowire, scale bar, 200 nm) results in a highly peaked evolution of the SE rate as a function of the transverse displacement. The nanomechanical motion δx around its equilibrium position x_0 is therefore transduced into large oscillations of the SE emission rate. Image and caption adapted under Creative Commons Licence from [105]

The signal $I_{SE}(t)$ can then be used to measure the dynamics of motion of the resonator, for example by plugging it into a Real-time Spectrum Analyser (RSA) which performs a Fast Fourier Transform (FFT), revealing the spectral structure of the motion and more particularly the resonances of the resonator (see section 2.1).

The key ingredients for the sensitivity of the measurement with this method are the contrast of the image at the measurement point $(\partial I_{SE}/\partial x)_{x_0}$ (as shown by eq. (1.3)), and the high confinement of the incident beam (the electron beam of a SEM can be as small as 1 nm). In this regard, the choice of an optimal working point of the SEM is crucial as the acceleration voltage, the current intensity and the working distance all have an impact on the result.

In summary, the main difference compared to standard optomechanical measurement is the absence of cavity and the reliance on a purely dissipative interaction: the secondary electrons originate from the sample itself, and are emitted after inelastic collisions with the primary electrons. The energy dissipation generates heating inside the resonator which, as was discussed earlier, limits the sensitivity of the measurement. The other difference is obviously the fact that a different particle is used: electrons are fermions and not bosons, and have a mass. This means that the back-action of the measurement can be parametrized by the acceleration voltage applied to the incident electrons, whereas the speed of light is fixed.

1.6 Objectives of the thesis & outline

The present thesis takes place in a context of fundamental research of physics studying the intrinsic limitations of a measurement of the motion of a nanowire resonator, for which the SEM is a relatively new and unexplored tool. The first objective of this work is to develop this technique in order to study how the effects of the beam on the nanowire depend on the details of exactly where the electron beam is applied along the length of the nanowire in a systematic way. The SEM-based detection scheme also presents a number of technical and fundamental limits, which require investigating in their own right, including strong dynamical-back-action effects (including the development of instabilities in the dynamics of the nanowire) that we will aim to characterize.

Another objective is to contribute to the understanding of thermal transport at the nano-scale, which is still very much an unknown territory for resonators of the size of CNT, although they have have very appealing mechanical properties. On the contrary, at the microscale thermal properties of AFM cantilevers have been thoroughly studied [71, 72, 109]. This has motivated interest in studying nanomechanical devices with dimensions in between. The first studies using the SEM demonstrated back-action cooling on SiC nanowires of lengths of the order of 100 µm [105], and we now aim for lower dimensions with InAs nanowires, with lengths of order 10 µm. We will thus study the thermodynamical state of the nanowire, which as we will see can be far from equilibrium.

Finally, while pursuing these objectives, another effect became visible: the electron beam alters the structure of the nanowire during the measurement process. Studying and quantifying this effect became another goal of this work.

Outline of the thesis. In chapter 2, we will provide the relevant theoretical background for the rest of this thesis, exploring the behaviour of a nano-beam as a mechanical resonator and introducing the concepts of dynamical back-action and non-equilibrium states more thoroughly. We will also review recent results making use of the SEM, which are the basis of the present work. Chapter 3 presents the methods used during this thesis, including the growth of the samples, the instruments used and the steps of software development that were necessary to perform the measurements. Then, in chapter 4 we will present the experimental results obtained and discuss them. These results include dynamical back-action based on thermo-mechanical effects, a study of the self-sustained oscillation regime of a nanowire, study of the local temperature distribution and its effect on the fluctuational temperature of each mode, and a structural effect identified as etching of the sample.

Chapter 2

Theoretical background and review of recent work

The aim of the present chapter is to provide the necessary theoretical background for the rest of this thesis. We will start by discussing the motion of a damped harmonic oscillator, which is the corner stone of the description of mechanical resonators, and in particular, the one which will be the subject of this thesis: an InAs nanowire. We will then define and review the properties of the damped harmonic oscillator's spectrum, i.e. the Power Spectral Density (PSD) of its displacement. In section 2.2, the concept of measurement backaction will be introduced, and illustrated with the example of a Fabry-Pérot cavity. In section 2.3 we will see how the damped harmonic oscillator framework links with the description of a cantilevered beam, which is an accurate description of a singly clamped nanowire. Section 2.4 will focus on the losses inside the nanowire, and different ways of modeling them. We will then delve into thermodynamics in section 2.5 to see how non-equilibrium situations can be modeled in our system. Finally, in section 2.6 we will review some recent works involving the Scanning Electron Microscope (SEM) as a measuring probe for the fluctuations of displacement of a nanowire.

2.1 Damped harmonic oscillator

The most commonly studied system in physics is the harmonic oscillator. It provides the starting point for describing the displacement of any mechanical resonator, and in particular a nanowire. In this section we will consider a point-like object of mass m, with a stiffness k leading to its mechanical resonant angular frequency $\Omega_0 = \sqrt{k/m}$. In this thesis we will often omit the "angular" term and refer to Ω_0 as simply the resonant frequency. If we assume the resonator to be subject to viscous damping at a rate Γ and some external force F_{ext}, its equation of motion takes the form

$$\ddot{X} + \Gamma \dot{X} + \Omega_0^2 X = F_{ext}/m, \tag{2.1}$$

where X is the displacement of the resonator and $\dot{X}$ is its temporal derivative.

When in thermal equilibrium with its environment, the resonator is subject to a random Langevin force F_T characterized by

$$\langle F_T(t) \rangle = 0 \tag{2.2}$$

$$\langle F_T(t) F_T(t') \rangle = 2m\Gamma k_B T \ \delta(t - t'), \tag{2.3}$$

where $\langle ... \rangle$ is the statistical average over a large number of realizations, k_B is Boltzmann's constant, T the temperature and δ the Dirac function.

The displacement of the resonator will thus fluctuate around its average value $\langle X(t) \rangle$. However, in order to fully understand the behaviour of the system, one needs to go beyond the averages and use statistical tools like the autocorrelation function and the Power Spectral Density (PSD), which we will now define.

2.1.1 Spectral analysis: definitions and properties

A key concept in the study of the dynamics of an oscillator is what we call its spectrum, or more formally its Power Spectral Density (PSD), which describes the distribution of the power of a given signal in the frequency domain. This quantity, which is relatively easy to measure (see section 2.1.4), is a great source of information about both the fluctuations of the system and its underlying dynamics. In this section, we will define the quantities needed to perform the spectral analysis of a signal and see how this relates to the practical aspects of the experiment.

First of all, we need to define the Fourier transform of a signal X(t). In this thesis, we will use the following convention:

$$\tilde{X}[\Omega] = \int_{-\infty}^{+\infty} X(t) e^{-i\Omega t} dt. \tag{2.4}$$

However, for the sake of simplicity we will use the notation $X[\Omega] = \tilde{X}[\Omega]$ in the following. We can then define the inverse Fourier transform to get the temporal signal from a frequency domain spectrum as

$$X(t) = \int_{-\infty}^{+\infty} X[\Omega] e^{i\Omega t} \frac{d\Omega}{2\pi}. \tag{2.5}$$

The Power Spectral Density (PSD) of a signal represents the distribution of power into the frequencies composing this signal. More formally, it is a function $S_{XX}[\Omega]$ such that [110]

$$S_{XX}[\Omega] = \lim_{T\to\infty} \frac{1}{T} \left| \int_0^T X(t) e^{-i\Omega t} dt \right|^2 . \tag{2.6}$$

The PSD is closely related to a quantity named the autocorrelation function of the signal, which describes the influence of the value of a signal at time t_1 on its value at another time t_2. It is defined as $C_{XX}(t_1, t_2) = \langle X(t_1)X(t_2)\rangle$, and in the case of a stationary process – which we will be considering here – the autocorrelation function only depends on the time difference $\tau = t_2 - t_1$. Thus, it can be expressed as

$$C_{XX}(\tau) = \langle X(t)X(t+\tau)\rangle . \tag{2.7}$$

The link between the PSD and the autocorrelation is a result known as the Wiener-Khinchin theorem which states that [110]

$$S_{XX}[\Omega] = \int_{-\infty}^{+\infty} C_{XX}(\tau) e^{-i\Omega\tau} d\tau, \tag{2.8}$$

i.e. the PSD is the Fourier transform of the autocorrelation function. This result was derived independently in 1930 and 1934 and is central to signal processing theory. A proof of this theorem can be found for example in [110]. Inversely, the autocorrelation function can be inferred from the PSD by:

$$C_{XX}(\tau) = \int_{-\infty}^{+\infty} S_{XX}[\Omega] e^{i\Omega\tau} \frac{d\Omega}{2\pi} \tag{2.9}$$

It is interesting to note that, since C_{XX} is the inverse Fourier transform of S_{XX}, by evaluating it for zero time shift we find that the variance of the signal ΔX^2

is the integral of its PSD over all frequencies:

$$\Delta X^2 = \int_{-\infty}^{+\infty} S_{XX}[\Omega] \frac{d\Omega}{2\pi}. \tag{2.10}$$

Another property of the PSD concerns the linear response. If a signal $Y(t)$ is related to $X(t)$ via a susceptibility χ such that $Y[\Omega] = \chi[\Omega]X[\Omega]$, then the PSD of Y is

$$S_{YY}[\Omega] = |\chi[\Omega]|^2 \, S_{XX}[\Omega]. \tag{2.11}$$

The frequency correlations $\langle X[\Omega]X[\Omega']\rangle$ are also of interest, as they can be expressed as a function of the PSD. To do so, we will use a double change of variables $\tau = t - t'$ and $s = (t + t')/2$:

$$\begin{aligned} \langle X[\Omega]X[\Omega']\rangle &= \int_{-\infty}^{+\infty} \int_{-\infty}^{+\infty} \langle X(t)X(t')\rangle \, e^{-i\Omega t} e^{-i\Omega' t'} dt dt' \\ &= \int_{-\infty}^{+\infty} e^{-i(\Omega+\Omega')s} ds \int_{-\infty}^{+\infty} C_{XX}(\tau) e^{-i(\Omega-\Omega')\tau/2} d\tau. \end{aligned}$$

The first integral reduces to a Dirac function $2\pi\delta[\Omega+\Omega']$, which lets us evaluate the second integral only when $\Omega' = -\Omega$, in which case it is equal to the Fourier transform of the autocorrelation function, that is the Power Spectral Density. Finally, we have the equality:

$$\langle X[\Omega]X[\Omega']\rangle = 2\pi\delta[\Omega + \Omega']S_{XX}[\Omega], \tag{2.12}$$

which in particular, for $\Omega' = -\Omega$ leads to

$$S_{XX}[\Omega] = \left\langle |X[\Omega]|^2 \right\rangle, \tag{2.13}$$

where we used that since $X(t)$ is real, $X[-\Omega] = X[\Omega]^*$. In other words, for real signals the PSD is equal to the statistical average of the square of the Fourier transform.

2.1.2 Power Spectral Density of an oscillator in thermal equilibrium

We now have all the tools required to describe the dynamics of a resonator in thermal equilibrium, that is subject to a random Langevin force described by eqs. (2.2) and (2.3). Many textbooks treat this subject, see for example [111, chapter 8]. In this section we will only provide a brief summary of this topic. Having defined the Fourier transform, we can now switch to the frequency domain and write eq. (2.1) as

$$\left(\Omega_0^2 - \Omega^2 - i\Gamma\Omega\right) X[\Omega] = F_{ext}[\Omega]/m. \tag{2.14}$$

According to linear response theory, we can then define the mechanical susceptibility of the resonator as the transfer function of the external force: $X[\Omega] = \chi[\Omega]F_{ext}[\Omega]$, leading to the expression for the susceptibility of a damped harmonic oscillator

$$\chi[\Omega] = \frac{1}{m\left[\Omega_0^2 - \Omega^2 - i\Gamma\Omega\right]}. \tag{2.15}$$

The imaginary part of the susceptibility describes the effects of dissipation in the resonator. When the resonator is coupled to a thermal bath in equilibrium at temperature T, the resonator is acted on by the Langevin force, that is characterized by the Fluctuation-Dissipation Theorem [112]:

$$S_{FF}[\Omega] = -\frac{2k_BT}{\Omega}\Im\left[\frac{1}{\chi[\Omega]}\right], \tag{2.16}$$

which can be simplified using eq. (2.15):

$$S_{FF}[\Omega] = 2m\Gamma k_BT \tag{2.17}$$

Finally, the PSD of the displacement of the resonator is

$$S_{XX}[\Omega] = \left|\chi[\Omega]\right|^2 S_{FF}[\Omega] = \frac{2\Gamma k_BT}{m\left[\left(\Omega_0^2 - \Omega^2\right)^2 + \Gamma^2\Omega^2\right]}. \tag{2.18}$$

Equations (2.17) and (2.18) have many implications. First of all, the thermal force applied to a resonator at equilibrium is a white noise, which means that the power spectral density of the displacement of the resonator is directly proportional to that of its susceptibility, which has a Lorentzian shape, as is plotted in fig. 2.1. Secondly, it highlights the routes available if one wants to reduce the thermal noise of a resonator: one would have to either reduce the mass of the resonator – which opened the field of nano-mechanics – or reduce the damping rate – by working in high vacuum, or engineering the losses in the resonator for example – or reduce the temperature of the environment, leading to cryogenic experiments with all the constraints they impose on the set-up.

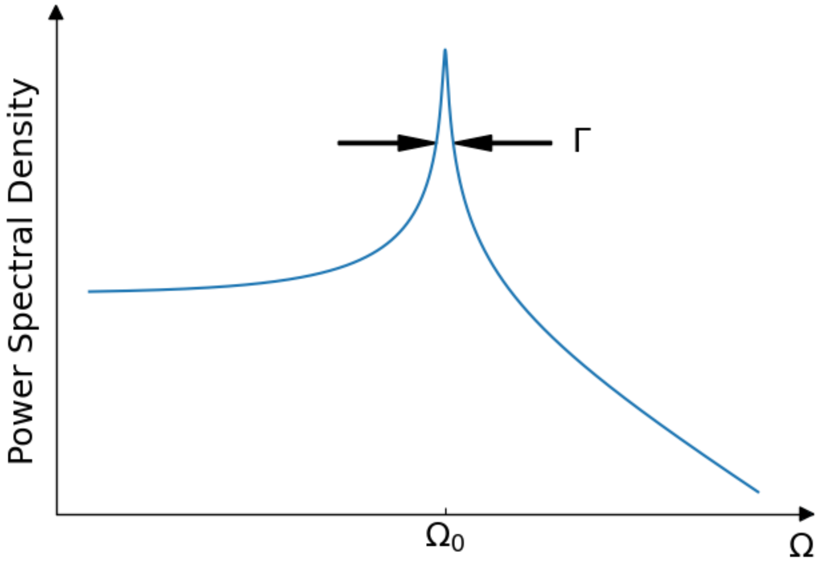

Figure 2.1: Power Spectral Density $S_{XX}[\Omega]$ of the displacement of a resonator of resonant frequency Ω_0 and damping Γ. The full width at half maximum (FWHM) is equal to the damping rate. Both axes are on logarithmic scale.

2.1.3 Equipartition of energy

Another key result concerning the damped harmonic oscillator is known as the equipartition theorem [113]. This result originated from statistical physics and the study of gases in the 19th century, and links the temperature of a system with its average energies, of different forms such as kinetic energy, elastic energy, etc. The theorem states that, in thermal equilibrium, the contribution of each of these energies is equal and the total energy is proportional to $k_B T$ with T the temperature.

In the case of a harmonic oscillator, the rule of "$(1/2) \times k_B T$ per degree of freedom" applies. In particular, for the resonator described so far, we have

$$\frac{1}{2} m \Omega_0^2 \left\langle \Delta X^2 \right\rangle = \frac{1}{2} k_B T, \tag{2.19}$$

where the left hand side of eq. (2.19) is the average potential energy of the resonator, with ΔX the displacement of the resonator around its equilibrium position.

This theorem is particularly relevant for a mechanical oscillator, as it allows one to evaluate its temperature by measuring its PSD, using eq. (2.10)

$$\Delta X^2 = \frac{1}{2} \frac{k_B T}{m \Omega_0^2} = \int_{-\infty}^{+\infty} S_{XX}[\Omega] \frac{d\Omega}{2\pi}. \tag{2.20}$$

2.1.4 Measuring the Power Spectral Density: duration and spectral resolution

When compared with practical conditions, the formal definition of the Power Spectral Density presents two difficulties. The first one is the statistical average in the definition of the autocorrelation function, meaning that a large number of realizations is required. The second problem comes from the infinite times needed to calculate the PSD, which in practice are not obtainable.

The solution to these issues lies in the ergodicity principle, which allows – for stationary processes only – to approximate the statistical average in the definition of the autocorrelation function (eq. (2.7)) by a time average, provided the measurement time T is much larger than the characteristic time of the signal ($2\pi/\Gamma$ for a mechanical resonator):

$$C_{XX}(\tau) = \langle X(0)X(\tau)\rangle \simeq \frac{1}{T}\int_0^T X(t)X(t+\tau)dt. \tag{2.21}$$

Then, since the Fourier transform is a linear operation, it commutes with the integral, and the PSD of a signal can be approximated in a finite time T as the Fourier transform of the finite time autocorrelation function. Therefore the Wiener-Khinchin theorem still applies when the statistical average is replaced by a time average over a finite window.

The measurement time T is a crucial parameter to acquire a good measurement of a spectrum. Indeed, it defines the Resolution Bandwidth, $RBW = 1/T$, which determines the minimal peak width that one is able to resolve, or the spectral resolution. Figure 2.2 illustrates this problem with the same signal measured for different RBWs. A trade-off has to be made between a shorter acquisition time, which has the advantage of requiring less computing power and has a lower impact on the sample, and a higher RBW which resolves the peaks, and allows an accurate measurement of the damping rate of the resonator. Indeed, if the RBW is too large, the peak will have the shape of the bandpass filter used by the spectrum analyser – a Gaussian of width equal to the RBW, see section 3.4 – and the dynamics of the resonator will not be accessible to the experimentalist.

Finally, in order to improve the signal-to-noise ratio of the measurement, one can average spectra. The uncertainty of the signal will decrease as $1/\sqrt{N}$ where N is the number of averages. This is a way of estimating the statistical average by accumulating realizations of the trajectory of the system. Averaging

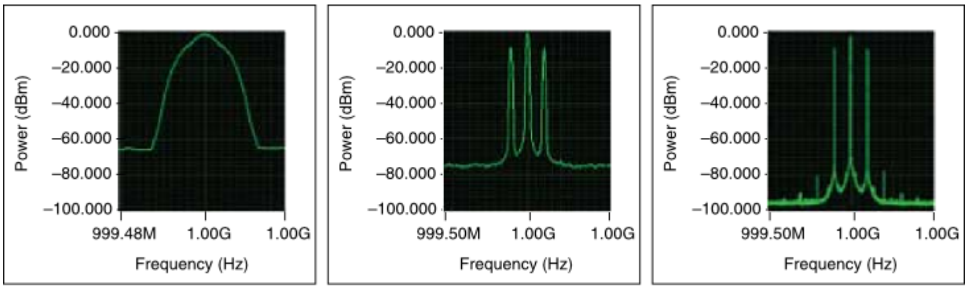

RBW = 100 kHz RBW = 10 kHz RBW = 100 Hz

Figure 2.2: Spectra acquired with different resolution bandwidth, revealing more details about the internal structure of the peaks as the bandwidth is decreased. ©National Instruments[1]

over many trajectories is equivalent through the ergodicity principle to taking a long enough acquisition time. One can then define the Video Bandwidth as $VBW = 1/NT$, which is the rate at which the measurement is actually repeated.

2.1.5 Quadratures and phase space

Another way of studying the dynamics of a resonator is to use a reference frequency Ω_{ref} and focus on the sine and cosine components of the signal generated by its displacement. One can thus define the quadratures of the displacement X_1 and X_2 such that

$$X(t) = X_1(t)\cos(\Omega_{ref}t) + X_2(t)\sin(\Omega_{ref}t). \tag{2.22}$$

This is particularly relevant for an underdamped oscillator as it allows one to focus on the slowly varying quadratures without the oscillating terms, if the reference frequency is the resonant frequency of the system. Indeed, the characteristic evolution time of the resonator is the inverse of its damping rate and for an underdamped oscillator $\Gamma \ll \Omega_0$. One can then neglect the high frequency components of the quadratures' Fourier transform and use the expressions

$$X_1[\omega] = X[\Omega_0 + \omega] + X[-\Omega_0 + \omega] \tag{2.23}$$

$$X_2[\omega] = -\,i\left(X[\Omega_0 + \omega] - X[-\Omega_0 + \omega]\right). \tag{2.24}$$

The frequency ω is thus the difference between the frequency of analysis of the displacement of the resonator and its resonant frequency, and the spectra of

---

[1] A short explanation of RBW by National Instruments can be found at https://www.ni.com/docs/fr-FR/bundle/ni-rfsa/page/nirfsa/resolution-bandwidth.html

the quadratures at zero frequency are linked to the spectrum of X at Ω_0.

The quadratures can be extracted from the displacement $X(t)$ using a demodulation scheme. For example, in order to get X_1, one must multiply $X(t)$ by a function $\cos(\Omega_0 t)$. The result is the sum of $X_1(t)/2$ and high frequency terms oscillating at $2\Omega_0$. By applying a low-pass filter, one can then exclude these terms and obtain X_1. Similarly, X_2 is obtained by multiplying $X(t)$ by a sine function.

At thermal equilibrium. Using the mechanical susceptibility as defined in eq. (2.15), one can deduce the values of $X[\Omega_0+\omega]$ and $X[-\Omega_0+\omega]$, assuming the resonator is underdamped ($\Gamma \ll \Omega_0$) and the analysis frequency is small compared to the resonant frequency ($\omega \ll \Omega_0$):

$$X[\Omega_0+\omega] = -\frac{1}{m\Omega_0\,(2\omega+i\Gamma)}F[\Omega_0+\omega] \tag{2.25}$$

$$X[-\Omega_0+\omega] = \frac{1}{m\Omega_0\,(2\omega+i\Gamma)}F[-\Omega_0+\omega], \tag{2.26}$$

where F is an external force applied to the resonator. One can define quadratures for F in a similar fashion as in eqs. (2.23) and (2.24):

$$F_1[\omega] = F[\Omega_0+\omega] + F[-\Omega_0+\omega] \tag{2.27}$$

$$F_2[\omega] = -i\left(F[\Omega_0+\omega] - F[-\Omega_0+\omega]\right). \tag{2.28}$$

Inserting eqs. (2.25) and (2.26) into eqs. (2.23) and (2.24) and eqs. (2.27) and (2.28), one obtains the following expressions for the quadratures of the displacement of a resonator subject to an external force

$$X_1[\omega] = -\frac{1}{2m\Omega_0}\left(\frac{1}{-i\omega+\Gamma/2}\right)F_2[\omega] \tag{2.29}$$

$$X_2[\omega] = \frac{1}{2m\Omega_0}\left(\frac{1}{-i\omega+\Gamma/2}\right)F_1[\omega]. \tag{2.30}$$

We now want to calculate the Power Spectral Density of the quadratures. In the case of a resonator at thermal equilibrium with its environment, the external force is the Langevin force F_T defined in eq. (2.17). It is thus necessary to calculate the quadratures of the force and their respective PSD. The correlation function of the Langevin force (eq. (2.3)) can be written in the form

$$\langle F_T[\Omega]F_T[\Omega']\rangle = 2m\Gamma k_B T \; 2\pi\delta(\Omega+\Omega') \tag{2.31}$$

where δ is the Dirac function. From this expression, we can deduce the cross-correlations between F_{T_1} and F_{T_2}:

$$\langle F_{T_1}[\omega]F_{T_2}[\omega']\rangle = -2i \; m\Gamma k_B T \left[2\pi\delta(2\Omega_0+\omega+\omega') - 2\pi\delta(-2\Omega_0+\omega+\omega')\right] \tag{2.32}$$

Since ω and ω' are small compared with Ω_0, the two Dirac delta functions are always null, which means that F_{T_1} and F_{T_2} are two independent random variables. Similarly, the autocorrelation functions are

$$\langle F_{T_1}[\omega]F_{T_1}[\omega']\rangle = \langle F_{T_2}[\omega]F_{T_2}[\omega']\rangle = 4m\Gamma k_B T \; 2\pi\delta(\omega+\omega'). \tag{2.33}$$

As a consequence, PSDs of both quadratures are frequency-independent and equal twice the PSD of the Langevin force: $S_{T_1} = S_{T_2} = 4m\Gamma k_B T$. Using eq. (2.11), the PSD of the quadratures of the displacement become

$$S_{X_1}[\omega] = S_{X_2}[\omega] = \frac{\Gamma k_B T}{m\Omega_0^2\,(\omega^2+\Gamma^2/4)}. \tag{2.34}$$

In conclusion, in thermal equilibrium the PSDs of the quadratures of the motion of the resonator are Lorentzian-shaped, of widths determined by the damping rate of the oscillator. The area of these spectra is directly related to the variances of the quadratures

$$\Delta X_1^2 = \Delta X_2^2 = \frac{k_B T}{m\Omega_0^2}. \tag{2.35}$$

This result is simply a re-expression of the equipartition theorem in terms of the two quadratures.

Finally, it is interesting to represent the quadratures of the resonator in the so-called "phase space", that is a parametric representation $(X_1(t), X_2(t))$ on a plane. Indeed, for a given time t, the value of $X_1(t)$ and $X_2(t)$ fully characterize the vibrational state of $X(t)$, with an amplitude $\sqrt{X_1^2+X_2^2}$ and a phase ϕ given by $\tan(\phi) = X_2/X_1$. Tracking the trajectory of the movements in phase space will allow one to map the distribution of probability of the two random variables X_1 and X_2.

If the trajectory is studied for a duration that is large compared with the characteristic time of evolution of the autocorrelation functions (i.e. $1/\Gamma$),

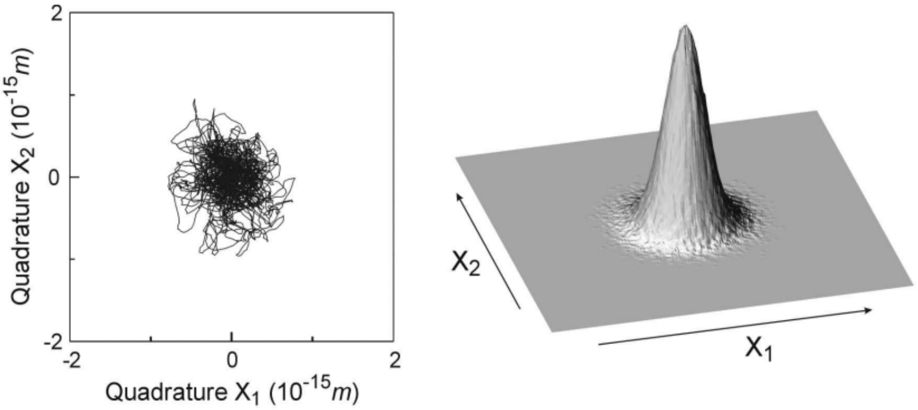

Figure 2.3: Left: Time trace of the trajectory of a Brownian motion in phase space, measured for a Fabry-Pérot cavity with a movable end mirror of millimetre dimensions. Right: Histogram of the trajectory. Reprinted with permission from [114].

it will reveal a Gaussian shape centred on the origin when the resonator is in thermal equilibrium, as illustrated in fig. 2.3. This is expected since the autocorrelation function for the quadratures, C_{ii} (with $i = 1$ or 2), can be calculated by taking the inverse Fourier transform for S_{X_i}:

$$C_{ii}(\tau) = \Delta X_i^2 \exp(-2\tau/\Gamma). \tag{2.36}$$

In other words, the motion of a mechanical resonator at thermal equilibrium with its environment is not a completely random march across phase space: it is centred around the origin by the restoring force of the harmonic oscillator.

Coherently driven oscillator. When a coherent drive (i.e. an external force oscillating at the resonant frequency) is applied to the resonator it leads to a new state in phase space, with amplitude and phase determined by the force applied. Thermal fluctuations will be superimposed on the state defined by the drive, as illustrated in fig. 2.4. The thermal state is shifted by by an amount $\left\langle X_{osc,2}^2 \right\rangle^{1/2}$ determined by the amplitude of the drive [115]. The amplitude noise of this new state remains equal to the initial thermal noise of the resonator (provided the drive itself does not fluctuate). However, the phase noise of the resonator is defined by the angle subtended by the distribution from the origin. It can thus be reduced by applying a bigger drive on the system. If the oscillator is subject to additional noise that leads to phase diffusion, for example because of frequency noise in the drive or because the system is self-oscillating, the thermal distribution spreads out in phase, leading to a limit circle of radius determined by the strength of the excitation, and eventually gives the phase

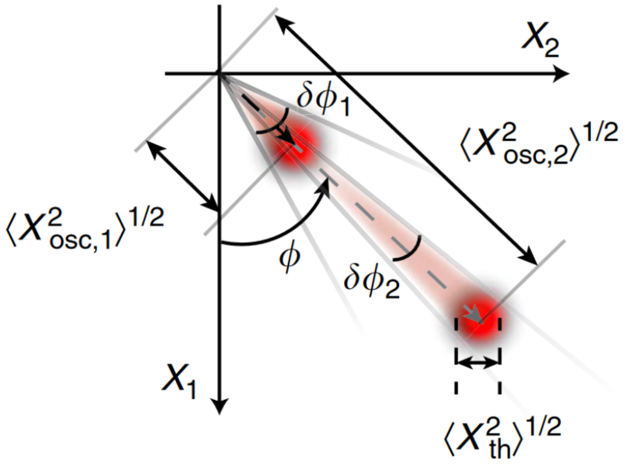

Figure 2.4: Thermal state of a coherently driven mechanical oscillator in phase space. This thermal state is displaced from the origin by the driven displacement amplitude $\left\langle X^2_{osc}\right\rangle^{1/2}$ and the phase noise $\delta\phi$ simply corresponds to the angle subtended by the thermal distribution measured from the centre. By increasing the drive amplitude, this angle, and thus the phase noise of the system, is decreased, as visualized here by two thermal state corresponding to displacement amplitudes $\left\langle X^2_{osc,1}\right\rangle^{1/2}$ and $\left\langle X^2_{osc,2}\right\rangle^{1/2}$. Reprinted with permission from [115].

space a doughnut-like shape [116]. The width of the doughnut is determined by the variance of the thermal motion.

Parametrically driven oscillator. A parametric drive – that is a drive at twice the resonant frequency of the system – is another interesting situation which can be analysed with the phase space. This drive can be achieved for example for an optical cavity through radiation pressure by modulating the input power, or more prosaically by a kid on a swing who goes up and down and modifies the effective length of the swing twice per period. This translates into a modulation of the effective damping of the resonator, and eqs. (2.29) and (2.30) become

$$X_1[\omega] = -\frac{1}{2m\Omega_0}\frac{1}{-i\omega+\Gamma_1/2}F_{T_2} \tag{2.37}$$

$$X_2[\omega] = \frac{1}{2m\Omega_0}\frac{1}{-i\omega+\Gamma_2/2}F_{T_1}, \tag{2.38}$$

with $\Gamma_1 = \Gamma(1+g)$ and $\Gamma_2 = \Gamma(1-g)$, g being the gain of the actuation [23]. Since the Langevin forces are not correlated, these equations mean that the two quadratures are still independent, and their PSD can be written as:

$$S_{X_1}[\omega] = \frac{\Gamma k_B T}{m\Omega_0^2\left(\Omega^2 + \Gamma_1^2/4\right)} \tag{2.39}$$

$$S_{X_2}[\omega] = \frac{\Gamma k_B T}{m\Omega_0^2\left(\Omega^2 + \Gamma_2^2/4\right)}. \tag{2.40}$$

We see from eqs. (2.39) and (2.40) that the variances of both quadratures are different, contrary to eq. (2.34), and that one of them can be squeezed, that is its variance is reduced compared with the standard thermal case, while the other is anti-squeezed (its variance is increased) as the gain is increased.

When the gain reaches 1, the system reaches an instability threshold and becomes bistable [114]: it oscillates between two stable states and switches from one to the other at a random rate determined by the gain. If the gain is further increased, the probability of switching from one state to the other becomes minimal, and the system remains in one state and displays variances that are similar to the thermal state. This is an interesting example of how, when the oscillator is supposed to be unstable, the non-linear terms of its response intervene to keep its motion bound in phase space. Similarly to the previous case, if the oscillator presents some frequency noise, the resulting phase space will have a doughnut shape. Figure 2.5 shows the phase space of a resonator under parametric excitation, for increasing values of the gain.

2.2 Dynamical back-action in a Fabry-Pérot cavity

Whenever a measurement takes place, it influences the object on which the measurement is being performed. It is well known in quantum physics, where the Heisenberg's uncertainty principle states that one can only increase the accuracy of a given measurement by decreasing that of a conjugated variable.

This phenomenon is known as back-action, which was introduced in section 1.3 in the context of the Standard Quantum Limit for continuous measurements (determined by back-action effects together with measurement imprecision). However, the concept of back-action (by which a measuring device affects the measured system) is not limited to quantum systems and is in fact a pervasive feature of classical physics, and it plays an important role in the classical systems studied in this thesis. Back-action has been predicted and measured

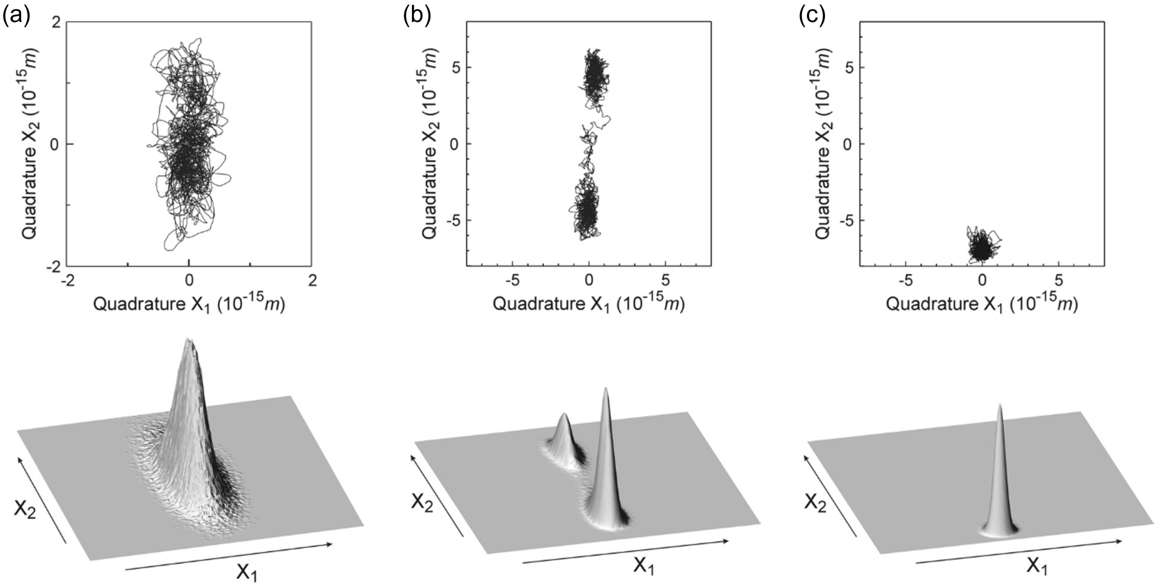

Figure 2.5: Evolution of the phase space for different gain of parametric excitation. Top: temporal traces; bottom: corresponding histograms. (a) For $g = 0.8$, the state of the resonator is squeezed. (b) For $g > 1$, the system becomes bistable, and jumps between two states. (c) For $g \gg 1$, the probability of switching to the second state is very low. Reprinted with permission from [114].

in multiple situations, with multiple objects and measurement systems, both quantum [117, 118] and classical [105, 107, 119]. The aim of the present section is to provide a general understanding of the topic with very basic principles which will be relevant for the rest of this thesis.

2.2.1 Dynamical back-action and retardation effects

As was mentioned in section 1.2, the system that is perhaps the most studied in optomechanics is the Fabry-Pérot cavity. As with any other system, it is not free from back-action mechanisms, whereby the very fact of measuring displacement of the end mirror of the cavity acts back on its mechanical motion. We will now study a simple, classical case of such back-action, in which retardation effects arising from the delay between the relaxation of the cavity field and the mechanical motion play a key role.

Let us consider a high-finesse Fabry-Pérot cavity, supporting a number of standing waves of the electro-magnetic field. Let us then assume that one of these modes, at frequency $\omega_c/2\pi$, is driven by a laser at frequency $\omega_L/2\pi$. When the laser frequency is close to the resonant frequency of the cavity, the amplitude of the mode grows dramatically.

Now let us consider that one of the mirrors is moving, to obtain a system similar to the one described in section 1.2. In this case, the mechanical motion of the mirror affects the cavity mode frequency and hence its response to the laser. This means that the response of the cavity can be used to measure the mechanical position, as discussed in section 1.2. However, the pressure exerted by the radiation acts back on the mechanics, affecting its position. The interplay of these elements is known as dynamical back-action, and it was predicted by Braginsky in the 1970s [30]. Additionally, if the finesse of the cavity is good, it presents a sharp resonance with a steep slope, which is used for high sensitivity measurements.

Equation of motion. For each laser frequency – actually for each value of the detuning $\Delta = \omega_L - \omega_c$ – the cavity has an equilibrium value of the amplitude, characterized by the mean number of photons in the mode $\bar{n}(\Delta)$ [7]. So for a fixed value of ω_L, the mirror has an equilibrium position x_0, leading to the photon number $\bar{n}(x_0)$.

Let us now assume that the cavity relaxes to its equilibrium at rate γ, due to losses through the interaction with electromagnetic modes outside of the cavity. When the position is changed to $x(t)$, the cavity will relax towards $\bar{n}(x(t))$. We then have a simple equation of motion:

$$\frac{dn}{dt} = \gamma \left(\bar{n}(x(t)) - n(t) \right). \tag{2.41}$$

where $n(t)$ is the number of photons at time t. The other part of the optomechanical coupling is a force experienced by the mirror, proportional to the number of photons: $F = \lambda n$, with λ a constant. Assuming the mirror's mass to be m, its resonant frequency Ω_0 and its intrinsic damping rate Γ, its equation of motion is

$$m\ddot{x} + m\Gamma\dot{x} + m\Omega_0^2 x = \lambda n(t). \tag{2.42}$$

Equilibrium solution. Solving eq. (2.42) for a fixed mirror, we have $x = x_0$, $\ddot{x} = \dot{x} = 0$ and $n = \bar{n}(x_0)$, which leads to

$$m\Omega_0^2 x_0 = \lambda \bar{n}(x_0). \tag{2.43}$$

Expanding around equilibrium, assuming small displacement, we have $x(t) = x_0 + \delta x(t)$ and $n(t) = \bar{n}(x_0) + \delta n(t)$. We can then expand $\bar{n}(x(t))$ as

$$\bar{n}(x_0 + \delta x) \simeq \bar{n}(x_0) + \left.\frac{d\bar{n}}{dx}\right|_{x=x_0} \delta x. \tag{2.44}$$

Combining the previous equation with eqs. (2.41) and (2.42) and noting $\bar{n}' = \left.\frac{d\bar{n}}{dx}\right|_{x=x_0}$, we get the following system of equations:

$$\begin{cases} \dot{\delta n} = \gamma(\bar{n}'\delta x - \delta n) \\ m\ddot{\delta x} + m\Gamma\dot{\delta x} + m\Omega_0^2\delta x = \lambda\delta n, \end{cases} \tag{2.45}$$

which in Fourier space becomes

$$\begin{cases} -i\Omega\delta n = \gamma(\bar{n}'\delta x - \delta n) \\ -m\Omega^2\delta x - im\Omega\Gamma\dot{\delta x} + m\Omega_0^2\delta x = \lambda\delta n. \end{cases} \tag{2.46}$$

The first equation of this system gives us

$$\delta n = \bar{n}'\frac{1 + i\Omega/\gamma}{1 + \Omega^2/\gamma^2}\delta x, \tag{2.47}$$

which we can substitute into eq. (2.46), to obtain

$$m\left[\Omega_{eff}(\Omega)^2 - \Omega^2 - i\Omega\Gamma_{eff}(\Omega)\right]\delta x = 0, \tag{2.48}$$

where we have written the effective resonant frequency and damping rate, respectively:

$$\Omega_{eff} = \sqrt{\Omega_0^2 - \frac{\lambda\bar{n}'}{m}\frac{1}{1 + \Omega^2/\gamma^2}} \tag{2.49}$$

$$\Gamma_{eff} = \Gamma + \Gamma_{ba}, \tag{2.50}$$

where we defined the back-action contribution to damping as

$$\Gamma_{ba} = \frac{\lambda\bar{n}'}{m\gamma}\frac{1}{1 + \Omega^2/\gamma^2}. \tag{2.51}$$

We see here that the result is similar to that of an uncoupled oscillator, but the delayed response of the cavity to a change in the position of the mirror translates into the appearance of an effective damping rate Γ_{eff} and frequency Ω_{eff}. Those two quantities depend on the frequency, which means that the dynamics of the position at a given time depends on the previous positions. Additionally, we can see from eq. (2.50) that the effective damping can become negative. Indeed, the sign of Γ_{ba} depends on that of $\bar{n}'$, which can be changed depending on the value of Δ. This situation corresponds to an amplification of the movement, and eventually leads to instability when Γ_{eff} reaches zero.

In order to regain a simpler picture of the problem, one can assume that the quality factor of the resonator is large ($Q = \Omega_0/\Gamma \gg 1$), and notice that the resonance will then be sharply peaked around Ω_0. In this case and assuming that the displacement δx remains small, eqs. (2.49) and (2.50) can be approximated by replacing Ω by Ω_0.

Effect of temperature. Let us now consider that the resonator is coupled to a thermal bath of temperature T, and neglect the fluctuations of n. As presented in section 2.1, this is represented by a random force $F_T(t)$, which satisfies eqs. (2.2) and (2.3).

We want to calculate the Power Spectral Density of the displacement δx of the mirror. To do so, we start from the equation of motion which takes the form

$$m\ddot{\delta x} + m\Gamma\dot{\delta x} + m\Omega_0^2\delta x = \lambda\delta n + F_T(t). \tag{2.52}$$

If we pass the term $\lambda\delta n$ to the left of the equation, we can used the effective susceptibility which was previously derived for zero temperature $\chi_{eff}^{-1}(\Omega) = m\left[\Omega_{eff}^2 - \Omega^2 - i\Gamma_{eff}\Omega\right]$ to write, in Fourier space:

$$\delta x[\Omega] = \chi_{eff}[\Omega]F_T[\Omega]. \tag{2.53}$$

Using the frequency correlations of δx and F_T, we can use eqs. (2.11) and (2.53) to write the PSD of the displacement of the resonator as

$$\begin{aligned} S_{xx}[\Omega] &= \left|\chi_{eff}[\Omega]\right|^2 2m\Gamma k_B T \\ &= \frac{2\Gamma k_B T}{m\left[(\Omega_{eff}^2 - \Omega^2)^2 + \Gamma_{eff}^2\Omega^2\right]}, \end{aligned} \tag{2.54}$$

which is very similar to the expression of the PSD of displacement for a damped oscillator without cavity. Actually, it can be put under the exact same form, provided we define an effective temperature $T_{eff} = \frac{\Gamma}{\Gamma_{eff}} T$:

$$S_{xx}[\Omega] = \frac{2\Gamma_{eff} k_B T_{eff}}{m\left[(\Omega_{eff}^2 - \Omega^2)^2 + \Gamma_{eff}^2 \Omega^2\right]}. \tag{2.55}$$

In conclusion, the delayed response of the cavity to the displacement of the mirror has the effect of shifting the resonant frequency of the cavity to an effective value Ω_{eff}, with an effective damping rate Γ_{eff} and an effective temperature T_{eff}. However, it is worth noting that here we have not included the quantum fluctuations of the cavity photons number. Including them leads to fundamental limits to measurement imprecision and modifies the effective temperature of the system, setting what is in effect a small but non-zero minimum value [7]. However, this can be safely neglected in what follows.

2.2.2 Consequences of back-action: cooling, heating, etc.

The previous derivation of the dynamical back-action effect is very generic: it only involves an arbitrary quantity n which can be the photon number in a cavity – but also any quantity coupled to the position of the oscillator – and decays to equilibrium at a given rate γ. These simple assumptions lead to the generic result that the resonator experiences an effective temperature and damping whose values will depend on the details of the system. In particular, the strength and even the sign of the back-action contribution to the damping Γ_{ba} can be changed by varying the set-up. As mentioned in section 2.2.1, for the cavity one can change the sign of Γ_{ba} by changing the laser detuning.

If $\Gamma_{ba} > 0$, then $T_{eff} < T$, i.e. the resonator is being cooled down. This effect can be used to reach to study quantum limits of measurement, for example by reaching the quantum ground state of an oscillator [120]. Alternatively, if $\Gamma_{ba} < 0$, the resonator will reach an effective temperature higher than its original temperature – provided that Γ_{eff} remains positive overall. In this case the amplitude of fluctuations in the system will increase until the system reaches a self-oscillating regime where Γ_{eff} is negative [85].

Another noteworthy effect is the so-called optical spring effect: the resonant frequency is shifted due to the dynamical back-action effect, as shown in eq. (2.49). This can be viewed as a spring constant added to the resonator. If this additional spring is positive, the resonator is said to be spring hardened, if it is negative the resonator is spring softened. This translates into a frequency shift of the resonator.

2.3 Euler-Bernoulli beam theory

The theory given in section 2.1 is very general and can be applied to any kind of mechanical oscillator, provided it is weakly damped and at thermal equilibrium with its environment. In this section, we will consider a specific mechanical system, a cantilevered beam, and see how a description in terms of simple harmonic motion emerges. The cantilevered beam is important as it provides a good description of the singly clamped nanowires studied in this thesis.

A very accurate description of a cantilevered beam can be obtained through Euler-Bernoulli theory. A detailed picture of this topic can be found for example in [111, chapter 6]. In this section we will derive the expressions for the mode shapes and resonant frequencies of such a beam, starting from general assumptions:

(i) The material we consider is assumed to be isotropic, homogeneous and elastic.

(ii) The system is long and thin (its length L is much bigger than its transverse dimensions) and possesses rotational invariance around its axis (we can limit ourselves to a two dimensional problem).

(iii) We only consider transverse flexural vibrations, i.e. we neglect shear and rotational inertia, as well as elongation.

(iv) We assume unidirectional strain (along the longitudinal direction).

(v) We use the Euler-Bernoulli hypothesis: there exists a neutral axis in which bending-induced stresses compensate. Cross-sections that are orthogonal to this plane will then remain orthogonal.

We wish to describe the field of displacement ($u_x(x, y)$, $u_y(x, y)$) of the beam under an arbitrary but small deformation along the transverse and longitudinal axes, respectively. The situation is illustrated in fig. 2.6. Let us consider a point P on the neutral axis, with coordinates (0, y). P is displaced into P', and the plane orthogonal to the axis remains orthogonal to it after the deformation, defining the deflection angle θ, which is assumed to be small. The displacement of P along y can then be neglected, i.e. $u_y(0, y) = 0$.

Consider now a second point Q separated from P by a distance dy along the neutral axis. Q is displaced into Q' by $u_x + du_x$, where u_x is the displacement of P. Using hypothesis (iii), the distance between P' and Q' along the neutral axis is still equal to dy, leading to

$$\sin\theta \simeq \theta = \frac{du_x}{dy}. \tag{2.56}$$

Let us then consider R with coordinates (x, y), located on the plane orthogonal to the neutral axis. The coordinate x does not need to be infinitesimal here, as this is valid for any point. Since θ is small, the displacement of R along x is approximately equal to the displacement of P, thus $u_x(x, y) = u_x(y)$ is only defined by the longitudinal coordinate. In the following, we will simplify the notation to $u(y)$, as this displacement is the quantity of interest for the study of the vibrational modes. Using hypothesis (v), we have the equality

$$u_y(x, y) = -x\sin\theta, \tag{2.57}$$

where the minus sign is included to respect the conventions adopted in fig. 2.6.

Finally, combining eqs. (2.56) and (2.57), we have

$$\begin{cases} u_x = u(y) \\ u_y = -x\sin\theta \simeq -x\frac{du}{dy}. \end{cases} \tag{2.58}$$

Strain and stress tensors. In the linear case, the strain tensor is generally defined as

$$\epsilon_{ij} = \frac{1}{2}\left(\frac{\partial u_i}{\partial r_j} + \frac{\partial u_j}{\partial r_i}\right), \tag{2.59}$$

with $u_i = (u_x, u_y, u_z)$ and $r_i = x, y, z$. In particular, the yy component of the strain tensor is expressed as

$$\epsilon_{yy} = \frac{\partial u_y}{\partial y} = -x\frac{\partial^2 u}{\partial y^2}. \tag{2.60}$$

Note that limiting ourselves to the linear part of the strain tensor includes the bending strain, but excludes elongation which is consistent with hypothesis (iii). This means that we consider a case in which there is bending, but the length of the beam remains constant which can be counter-intuitive and is obviously an approximation. However, this approximation remains accurate as long as the

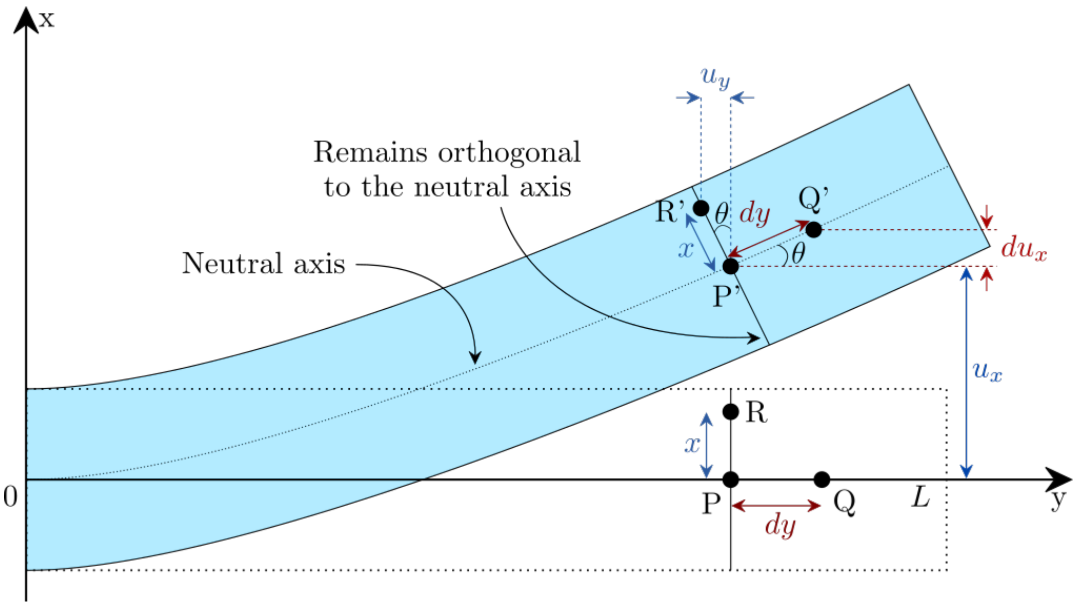

Figure 2.6: Displacement of the neutral axis of a beam under the effect of an arbitrary deformation. The original points P and Q are displaced into points P' and Q', defining the angle θ with the original neutral axis.

aspect ratio of the beam is large, and the amplitude of deflection small. In the following we will only consider bending moments and neglect any axial force affecting the displacement.

We can then define the stress tensor as

$$\sigma_{ij} = \sum_{k,l} C_{ijkl}\epsilon_{kl}, \tag{2.61}$$

where the C_{ijkl} terms form the stiffness matrix of the material. In the most general case, due to symmetries in the definition of ϵ, the stiffness matrix has 21 independent terms. However, assuming the simplest case of an isotropic material, this number is reduced to only two: Young's modulus E and Poisson's ratio ν. In particular we have the following stress-strain relation:

$$\sigma_{yy} = E\epsilon_{yy}. \tag{2.62}$$

Equilibrium conditions. In order to write the equation of motion of the beam, we need to consider the bending moments applied on a cross-section A, defined as

$$M_z = \int_A \left(\vec{r} \times \sigma_{yy} d\vec{A}\right)_z, \tag{2.63}$$

where $\vec{r} = x\vec{e_x} + z\vec{e_z}$ is the position vector and $\vec{dA} = dA\vec{e_y}$ is the elementary vector perpendicular to the cross-section. M_z is thus the z component of the bending vector $\vec{M}$. However, it is sufficient to only consider M_z since we limited ourselves to displacements along the x axis.

We can then write the equation of motion of an elementary volume $dV = Ady$ as

$$\rho A \frac{\partial^2 u}{\partial t^2}(y,t) = \frac{\partial^2 M_z}{\partial y^2}(y,t), \tag{2.64}$$

where ρ is the mass density of the material. Using the definitions in eq. (2.63) and assuming flexural rigidity (that is the product EI_z being constant, with I_z the moment of inertia for rotations about the z axis (orthogonal to the xy plane containing the displacement), $I_z = \int_A x^2 dA = \frac{\pi}{4}R^4$ for a cylindrical beam, with R the radius of the circular cross-section), the previous expression simplifies to what is known as the Euler-Bernoulli equation [111]:

$$\rho A \frac{\partial^2 u}{\partial t^2} = -EI_z \frac{\partial^4 u}{\partial y^4}. \tag{2.65}$$

Solutions of Euler-Bernoulli equation. In order to solve eq. (2.65), we will use a separation ansatz: $u(y,t) = u(y)e^{i\omega t}$. We then have $\partial u/\partial t = -i\omega u$ and solving for the spatial term we obtain

$$u(y) = C_1 \cos(\beta y) + C_2 \sin(\beta y) + C_3 \cosh(\beta y) + C_4 \sinh(\beta y). \tag{2.66}$$

where $\beta = \left(\rho A E \omega^2 / EI\right)^{1/4}$ and $C_{1,..,4}$ are constants that will be determined using the boundary conditions. However these constants are not unique, and will take different values, leading to a spectrum of eigenmodes. In our case, we will use the boundary conditions for a cantilevered beam:

$$\begin{cases} u = 0 \\ \frac{du}{dy} = 0 \end{cases} \quad \text{at } y = 0 \qquad \begin{cases} \frac{d^2u}{dy^2} = 0 \\ \frac{d^3u}{dy^3} = 0 \end{cases} \quad \text{at } y = L. \tag{2.67}$$

The solution of eq. (2.65) using eq. (2.67) is then the set of eigenmodes (u_n, ω_n) given by

$$\begin{cases} u_n(y) = C_n \left(\cosh(\beta_n y) - \cos(\beta_n y) + \frac{\cos(\beta_n L) + \cosh(\beta_n L)}{\sin(\beta_n L) + \sinh(\beta_n L)} \left(\sin(\beta_n y) - \sinh(\beta_n y) \right) \right) \\ \omega_n = \beta_n^2 \sqrt{\frac{EI}{\rho A}}, \end{cases} \tag{2.68}$$

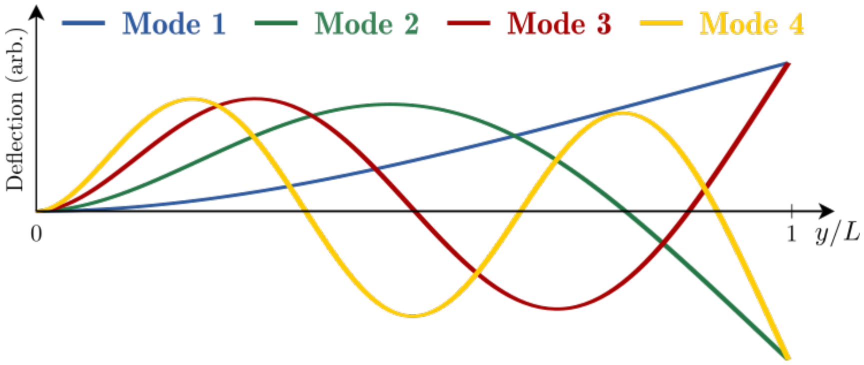

Figure 2.7: Spatial evolution of the first four mode shapes $u_n(y)$ for $n = 1, 2, 3, 4$ for a cantilevered beam.

where C_n is a normalization constant. The values of β_n are the solutions of $\cosh(\beta_n L)\cos(\beta_n L) + 1 = 0$ which can be numerically computed. The first values are $\beta_1 = 0.596864\pi/L$, $\beta_2 = 1.49418\pi/L$, $\beta_3 = 2.50025\pi/L$ and $\beta_4 = 3.49999\pi/L$. We can then define the "mode shape" ϕ_n of each mode as $u_n(y) = C_n \times \phi_n(y)$. The first four mode shapes are plotted in fig. 2.7.

Equivalence to the Harmonic Oscillator. In the general case, the displacement of a cantilever is not confined to a single mode. However, since eq. (2.65) is a linear differential equation and the modes u_n form an orthogonal base, the general solution can be expressed as a superposition of all the modes [121, page 73-75]

$$u(y,t) = \sum_{n=0}^{\infty} a_n u_n(y) e^{i\omega_n t}, \tag{2.69}$$

where $a_n(t)$ is the amplitude of each mode, dependent on the forces applied to the beam.

In practice, each mode can be considered separately, provided that their eigenfrequencies are distant enough from each other and that the damping is low (the peaks of each Lorentzian do not overlap in the PSD of the oscillator). Each mode then behaves as an independent harmonic oscillator whose restoring force is due to the internal rigidity of the beam. The derivations of section 2.1 are then valid using the displacement distribution $u(y,t)$ as the variable, provided an effective mass $m_n(y)$ is defined for each mode and position y along the beam [122]

$$m_n(y) = M_n \frac{u_n(L)^2}{u_n(y)^2}. \tag{2.70}$$

Here M_n is a position-independent effective mass for the mode corresponding to the displacement of the free end of the beam, defined by

$$M_n = \int_0^L \rho A \frac{u_n(y)^2}{u_n(L)^2} dy. \tag{2.71}$$

For example, for the first flexural mode of a cylindrical beam, we have $M_1 \simeq 0.23M$ with M the physical mass of the beam.

Degeneracy of the solution. The development proposed so far assumed a perfect rotational invariance of the beam. This let us consider the vibrations along the x axis only, and discard those along the z axis as they have the exact same resonant frequencies. The same would be true for a beam with a perfectly square cross-section.

However, in the real world the samples are never perfectly symmetric, and the cross-sections are elliptical or rectangular instead of circular or square. The presence of imperfections and defects in the structure lifts the degeneracy of the resonances, and each each pair of nearly degenerate modes presents a doublet of peaks separated by a quantity dependent on the actual geometry of the resonator, with each peak corresponding to a different direction of vibration. These directions are always orthogonal, and are often referred to as the in-plane and out-of-plane mode. Qualitatively, the closer the frequencies of the doublet are, the "more symmetric" the resonator is.

2.4 Modeling the losses

The dissipation of energy plays a crucial role in the dynamics of a resonator. In this section, we will see how this dissipation, often referred to as losses, is usually modeled. Phenomenologically, it can be accounted for by introducing a loss angle $\phi[\Omega]$ in the imaginary part of the mechanical susceptibility so that

$$\chi[\Omega] = \frac{1}{m\left(-\Omega^2 + \Omega_0^2(1 + i\phi[\Omega])\right)}. \tag{2.72}$$

Since we deal with resonant systems, it is safe to assume that $\phi \ll 1$.

The definition of the loss angle is thus crucial to the description of the dynamics of the system, and different models exist. In section 2.1, we assumed that the losses arise from a viscous damping that is a force inversely proportional to the velocity of the resonator. This leads to a definition the loss angle as

$$\phi[\Omega] = \frac{\Omega}{Q\Omega_0}, \tag{2.73}$$

where Q is the mechanical quality factor of the resonator and Ω_0 its resonant frequency. This leads back to the familiar expression for the susceptibility as defined in eq. (2.15).

Another possibility is to include the viscoelastic damping of the resonator, also known as internal or structural damping. Assuming these losses are uniformly distributed, they can be accurately modeled by introducing a frequency-independent imaginary part in the stiffness of the resonator [123], leading to a susceptibility

$$\chi[\Omega] = \frac{1}{m\Omega_0^2\left(1 - \frac{\Omega^2}{\Omega_0^2} + i\phi\right)}. \tag{2.74}$$

In this case, the loss angle defines the quality factor $\phi = \frac{1}{Q}$, and induces a $1/\Omega$ behaviour at frequencies below the resonance.

When both phenomenon are included, the quality factor is the combination of the two values:

$$Q_{eff}^{-1} = Q_{viscous}^{-1} + Q_{structural}^{-1}. \tag{2.75}$$

In general, if multiple sources of dissipation are considered, each of them will generate a quality factor, and the effective Q for the whole system will be a combination of all of them, and generally dominated by the smallest

$$Q_{eff}^{-1} = \sum_n Q_n^{-1}. \tag{2.76}$$

The case of losses inhomogeneously distributed along the beam is also worth considering. In this case, the linear description in terms of independent harmonic oscillators that we have used so far is no longer valid. Its generalization leads to an effective coupling between mechanical modes [124, 125]. The distribution of the losses can then lead to either increased or decreased thermal motion, and therefore becomes a crucial parameter that needs to be determined in order to obtain a precise picture of the dynamics of a resonator. It has an even more important role when the thermal effects are taken into account, as it defines the effect that heating has on the dynamics, as we will see in section 2.5.

2.4.1 Loss mechanisms in InAs nanowires

In the case of InAs nanowires measured in a SEM, the loss mechanisms that should be considered are viscous damping, clamping losses and thermo-elastic losses. However, the first one can be ruled out as the main source of losses due to the high vacuum in which the measurements are performed.

Clamping losses are defined as the power radiated by the nanowire into its basis or substrate. While they can have an important impact, especially when the substrate and the resonator have different crystalline structure, this not the case here. Indeed, the amount of clamping losses for a singly clamped beam whose material is the same as the substrate decreases as the inverse of the aspect ratio to the power four [126]. The large aspect ratio of our nanowires is thus a critical point to ensure a good quality factor and minimize clamping losses.

Finally, thermo-elastic losses are generally identified as the main loss mechanism in this kind of systems. These losses occur when there is a mismatch between the equilibrium state of the phonon bath inside the resonator and its geometry, for example because the nanowire has bent. In this situation, the phonons will relax to the new equilibrium conditions, which will change dynamically in the case of vibrations. There is then a phase delay between the phonons and the mechanics which, similarly to what is described in section 2.2, induces a damping, i.e. losses.

A formal description of thermo-elastic dissipation can be found in [127] for the diffusive thermal phonons regime,i.e. when the relaxation rate of the phonon distribution is much faster than the frequency of the acoustic mode. The coupling mentioned above is described by introducing a complex, frequency-dependent Young's modulus in Euler-Bernoulli's equation, which leads to complex eigen-frequencies, the imaginary part of which corresponds to thermo-elastic damping.

2.5 Non-equilibrium thermal models

The interaction between a focused electron beam and a nanowire includes some dynamical back-action similar to the development of section 2.2. However, it goes beyond the strict application of these results as it involves actual heating of the resonator, in addition to the increase of the effective temperature. This interaction sets the resonator far from equilibrium, which requires the development of new models to understand the evolution of its internal temperature, as we will discuss later on in the thesis. In this section, we will see how the Fluctuation-Dissipation Theorem (FDT) can be expanded from its usual form given by eq. (2.16) to a version adapted to non-equilibrium states. These non-equilibrium states are of great interest for topics beyond mechanical resonators, as this situation occurs for example in living systems [128, 129], glasses [130], active matter [131], or materials subject to a heat flux [132].

In our case, we will start by extending the FDT from a single harmonic mode to a continuous system. We will consider a one-dimensional, singly clamped cantilever. Following a development proposed in [71], the Euler-Bernoulli equation eq. (2.65) can be extended by replacing the flexural rigidity with a position-dependent stiffness $k_(y, \Omega)$. According to section 2.4, k can be decomposed into the local stiffness k^r and the internal dissipation k^i as $k(y, \Omega) = k^r(y, \Omega) + ik^i(y, \Omega)$. The equation of motion in Fourier space then reads [109]

$$-m\Omega^2 u(y, \Omega) + \frac{\partial^2}{\partial y^2}\left(k(y, \Omega)\frac{\partial^2 u}{\partial y^2}\right) = F(y, \Omega), \tag{2.77}$$

where $u(y, \Omega)$ is the local deflection of the beam, y being the longitudinal position along the beam and $F(y, \Omega)$ an arbitrary external force. Note that in general the stiffness depends on the frequency, however in the following we will assume this dependency to be slow around the resonances, so that $k(y, \Omega) \simeq k(y, \Omega_n)$ for mode n.

Constant temperature. If the temperature is assumed to be uniform along the nanowire, eq. (2.77) leads to an extension of the FDT [71]

$$S_{FF}(y, y', \Omega) = \frac{2}{\pi}\frac{k_B T}{\Omega}\frac{\partial^2}{\partial y^2}\left[k^i(y, \Omega)\frac{\partial^2}{\partial y^2}\delta(y - y')\right], \tag{2.78}$$

where the two point PSD is defined as

$$\langle F(y, \Omega)F(y', \Omega')\rangle = S_{FF}(y, y', \Omega)\delta[\Omega + \Omega']. \tag{2.79}$$

Non-uniform temperature. However, if the cantilever is subject to heat fluxes – as will happen when measured by a laser beam as in [71] or an electron beam as will be discussed later – we need to consider a non-uniform temperature profile $T(y) = T_0 + \Delta T(y)$ with T_0 the room temperature. In this case, eq. (2.78) generalizes to

$$S_{FF}(y,y',\Omega) = \frac{2}{\pi}\frac{k_B}{\Omega}\frac{\partial^2}{\partial y^2}\left[T(y)k^i(y,\Omega)\frac{\partial^2}{\partial y^2}\delta(y-y')\right]. \tag{2.80}$$

Mode distribution and effective temperature We will now concentrate on the resonant modes of the resonator, which offer a global description of the cantilever's motion. We will seek to define an effective temperature associated with the fluctuations of each mode. The modes are characterized by their mode shape ϕ_n defined in section 2.3. Each ϕ_n is an eigenvector of the operator $\mathcal{L} = \frac{\partial}{\partial y}\left[k^r(y,\Omega)\frac{\partial^2}{\partial y^2}\right]$ associated with the eigenvalue $k^r_n[\Omega]$ such that $\mathcal{L}\phi_n(y) = k^r_n[\Omega]\phi_n(y)$ [71].

The conjugated force F_n is then defined as the projection of F on the mode shape: $F_n[\Omega] = \int_0^L F(y,\Omega)\phi_n(y)dy$. The power spectral density of F_n can then be expressed as

$$\begin{aligned} S_{F_nF_n}[\Omega] &= \int_0^L dy \int_0^L dy'\phi_n(y)\phi_n(y')S_{FF}(y,y',\Omega) \\ &= \frac{2}{\pi}\frac{k_B}{\Omega}\int_0^L dy\phi''_n(y)^2T(y)k^i(y,\Omega). \end{aligned} \tag{2.81}$$

Each mode then has a susceptibility similar to eq. (2.74), with the internal damping of mode n $k^i_n[\Omega] = \int_0^L \phi''_n(y)k^i(y,\Omega)dy$ taking the role of the loss angle:

$$\chi_n[\Omega] = \frac{1}{k^r_n[\Omega] - m\Omega^2 + ik^i_n[\Omega]}. \tag{2.82}$$

Once again, the slow dependency of k on Ω around the resonances lets us approximate $k^r_n[\Omega] \simeq k^r_n[\Omega_n]$ and $k^i_n[\Omega] \simeq k^i_n[\Omega_n]$.

The effective temperature of each mode, T^{eff}_n, will be defined using an extended equipartition theorem:

$$\frac{1}{2}k^r_n\left\langle u_n^2\right\rangle = \frac{1}{2}k_BT^{eff}_n \tag{2.83}$$

where $\langle u_n^2\rangle$ is the mean deflection of mode n, which can be measured by integrating the PSD of thermal noise:

$$\begin{aligned} \left\langle u_n^2\right\rangle &= \int_0^\infty d\Omega\left|\chi_n[\Omega]\right|^2 S_{F_nF_n}[\Omega] \\ &\simeq \frac{k_B}{k^r_n[\Omega_n]k^i_n[\Omega_n]}\int_0^1 dy\phi''_n(y)^2T(y)k^i(y,\Omega_n). \end{aligned} \tag{2.84}$$

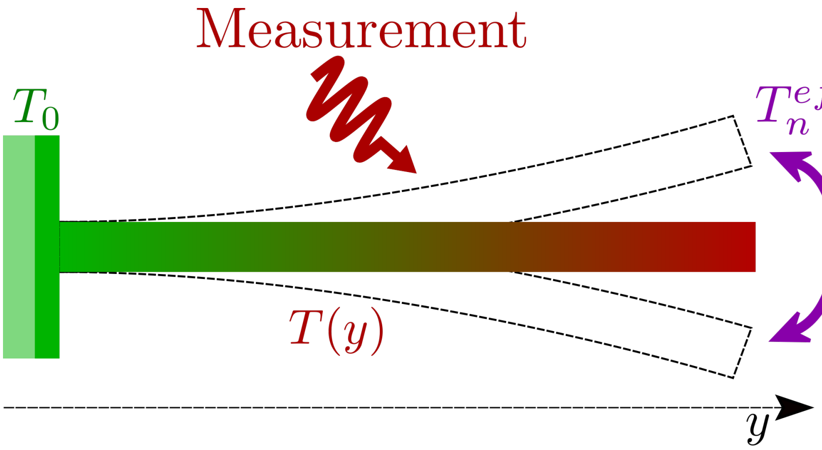

Figure 2.8: Different temperatures are involved in the measurement process: the environment temperature T_0, the local temperature field $T(y)$ and the fluctuational temperature T_n^{eff}.

We can note that using eq. (2.84) with constant temperature T, one recovers the classic equipartition theorem $k_n^r \langle u_n^2 \rangle = k_B T$, similar to eq. (2.19). Finally, we can express the effective temperature as

$$T_n^{eff} = \int_0^1 dy T(y) w_n(y), \tag{2.85}$$

where $w_n(y)$ is a localized dissipation rate, defined as

$$w_n(y) = \frac{\phi_n''(y)^2 k^i(y, \Omega_n)}{\int_0^1 dy' \phi_n''(y')^2 k^i(y', \Omega_n)}. \tag{2.86}$$

The mode-dependent temperature is thus a spatial average of the temperature profile, weighted by the local dissipation of the considered mode.

In conclusion, in order to describe a mechanical resonator in a non-equilibrium steady state, one needs to define several temperatures, as summarized in fig. 2.8:

- The environment temperature T_0, which is the temperature of the clamping point of the cantilever
- The local temperature along the nanowire $T(y)$
- The average temperature of the cantilever $T_{avg} = (1/L) \int_0^L T(y) dy$
- The effective temperature T_n^{eff} of each mode, also called the fluctuational temperature

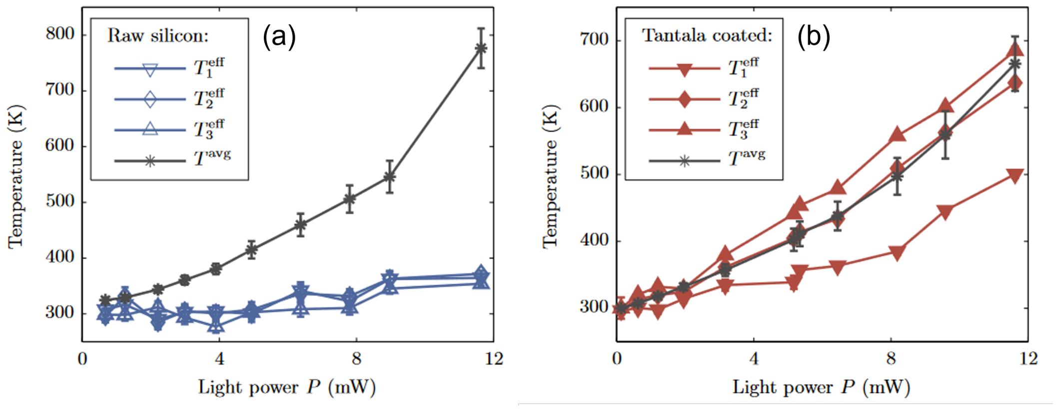

Figure 2.9: Effective temperatures of the first three modes of an AFM cantilever and its average temperature, as a function of the power of the probe laser. (a) Raw silicon cantilever: T_n^{eff} is mode independent and almost constant (equal to room temperature), when T avg raises by 400 K. (b) Tantala coated silicon cantilever: T_n^{eff} is mode dependent, and increases with P similarly to T avg for $n > 1$. Reprinted with permission from [71].

In general, all these quantities can differ. This was illustrated in [71] on a system consisting of a microcantilever illuminated at its tip by a focused laser beam. In such a system, the fluctuational temperature associated with the vibration, was measured to match the environment temperature, whereas the cantilever itself has an internal temperature close to its melting point. Because the losses are localized around the anchor point of the cantilever, in this case $k_n^i(y) = k_{n,0}^i$ at $y = 0$ and 0 elsewhere and using eq. (2.85), the effective temperature of all modes equals the clamping temperature, i.e. $T_n^{eff} = T_0 \ \forall n$, as illustrated in fig. 2.9a. Another example is provided using a tantala (Ta_2O_5) coated cantilever. The coating consists of an amourphous layer which introduces a uniform mechanical damping along the beam, thus creating the dependency of the effective temperature on the mode number, as shown in fig. 2.9b.

2.6 Electromechanical coupling from an electron beam

Having provided the necessary theoretical background, we will now discuss two recent results obtained using the Scanning Electron Microscope (SEM) as a measurement device for nano-resonators, both concerning dynamical back-action effects and using an experimental setup similar to the one described in section 1.5. The first result we will present was the first experimental demonstration of dynamical back-action cooling of a SiC nanowire using a SEM [105].

The second is the demonstration of radiation pressure back-action from the electron beam [107].

2.6.1 Electrothermal back-action

The electrothermal back-action derives from the extremely dissipative nature of the interaction between the nanowire and accelerated electrons, whose incident energy is mainly converted into very slow secondary electrons and subproducts dominated by an increase in temperature of the wire. This heat creation leads to deformations that are equivalent to nanomechanical motion in one direction.

The experiment described in [105], the first dynamical back-action cooling experiment not mediated by an electromagnetic resonance, was performed in 2015. It demonstrated that under the illumination of a continuous focused electron beam, a nanowire can spontaneously reach an equilibrium with drastically reduced effective temperature of fluctuations. One key element of this experiment is the sub-nanometre confinement of the electron beam, yielding very high electromechanical force gradients. The object studied here is a cylindrical silicon carbide (SiC) nanowire with length L = 150 µm and diameter d = 250 nm, and the detection process is similar to the one described in section 1.5. Resonant frequencies were measured around 20 kHz.

The deformations of the nanowire under the effect of the electron-matter interaction can be described by a static force F_{ext} applied at a position $(x_p,\, y_p)$ on the nanowire. However, due to the motion of the nanowire, this position depends on time. Assuming that the displacements are small and orthogonal to the electron beam, we will consider that only x_p varies, and we will note δx_p its displacement with respect to its equilibrium position $x_{p,eq}$ (see notations in fig. 2.10a). The time-varying part of the force can thus be written $\delta F_{ext}(t) \simeq \partial F_{ext}/\partial x|_{x_{p,eq}}\, \delta x_p(t)$. Additionally, the response of the nanowire to the force can be delayed, and we will define its time response function, $R(t)$. Note that $R(t)$ is treated phenomenologically at this point, allowing us to include the possibility of a delayed response, we will return to consider how it may actually arise later on.

In Fourier space, displacement of the tip of the nanowire can thus be described by

$$\chi^{-1}[\Omega]\delta x[\Omega] = F_T[\Omega] + R[\Omega] \left.\frac{\partial F_{ext}}{\partial x}\right|_{x_{p,eq}} \delta x_p[\Omega], \tag{2.87}$$

where δx denotes the transverse displacement of the tip of the nanowire with respect to its equilibrium position, χ its mechanical susceptibility and F_T the thermal Langevin force. Note that χ^{-1} involves the effective mass of the mode estimated at the tip of the nanowire $m_{eff}(L)$, defined previously in eq. (2.70).

The second term of eq. (2.87) corresponds to the induced force related to the measurement probe (i.e. back-action), which is modulated due to the motion of the nanowire around the point of incidence of the electron beam. This equation is very similar to eq. (2.52), though here the back-action is mediated by the temperature of the nanowire, instead of the photon number inside an optical cavity.

The displacement δx_p is related to the displacement of the tip of the nanowire through the mode shape ϕ_n: $\delta x_p = (\phi_n(y_p)/\phi_n(L))\delta x$, which allows us to rewrite eq. (2.87) as $\delta x[\Omega] = \chi_{eff}[\Omega] F_T[\Omega]$ with χ_{eff} an effective susceptibility given by

$$\chi_{eff}^{-1}[\Omega] = \chi^{-1}[\Omega] - \frac{\phi_n(y_p)}{\phi_n(L)} R[\Omega] \left. \frac{\partial F_{ext}}{\partial x} \right|_{x_{p,eq}} . \tag{2.88}$$

In order to better understand this susceptibility, it is necessary to understand the nature of the delayed response function R. The authors of [105] noticed that the dissipation increased when the electron beam was moved to the tip of the nanowire, as shown in fig. 2.10b.

This suggests that important delays are involved in the dynamical interaction between the primary electron beam and the resonator and led to to the interaction being identified as having a thermal origin, i.e. the heating due to the interaction with the electron beam deforms the nanowire, giving rise to F_{ext}. The characteristic time of this interaction is defined by the time required for the heat produced to propagate along the whole nanowire: $\tau_{th} = L^2 \rho c_p \kappa$ with ρ the density, c_p the specific heat capacity and κ the thermal conductivity (τ_{th} is a worse case estimate, when the heating source is at the tip of the nanowire, hence the presence of L instead of y_p for example). The response function can then be written as

$$R(t) = \frac{H(t)}{\tau_{th}} e^{-t/\tau_{th}} \tag{2.89}$$

$$R[\Omega] = \frac{1}{1 + i\Omega\tau_{th}}, \tag{2.90}$$

with $H(t)$ the Heaviside step function. In the case of an SiC nanowire, we have $\Omega_0 \tau_{th} \gg 1$, which allows to retain only the dissipative contribution of the back-action force. We can then write last term of eq. (2.88) as purely imaginary:

$$R[\Omega] \left.\frac{\partial F_{ext}}{\partial x}\right|_{x_{p,eq}} = i m_{eff}(L)\Omega\Gamma_e(x_{p,eq}), \tag{2.91}$$

where Γ_e is the maximum dissipative coupling strength, when the probe hits the edge of the nanowire and is assumed to vary only along the transverse axis.

The effective mechanical damping rate and temperature can thus be written as:

$$\Gamma_{eff}(y_p) = \Gamma_m + \frac{\phi_n(y_p)}{\phi_n(L)}\Gamma_e(x_{p,eq}) \tag{2.92}$$

$$T_{eff}(y_p) = \frac{\Gamma_m}{\Gamma_{eff}}T. \tag{2.93}$$

Note that $\phi_n(y_p)/\phi_n(L)$ is inversely proportional to the square root of the effective mass $m_{eff}(y_p)$, which diverges quickly as y_p tends to 0. As such, it is convenient to plot Γ_{eff} and T_{eff} as a function of the effective mass instead of y_p. The corresponding experimental results are presented in fig. 2.10, exhibiting a temperature and damping rate dependency on the longitudinal position, as expected from eqs. (2.92) and (2.93). These results establish the first self-induced cooling mechanism that is not mediated by an electromagnetic resonance, but entirely relies on the local force field spatial confinement, i.e. large values of $\left.\frac{\partial F_{ext}}{\partial x}\right|_{x_{p,eq}}$.

Another important result established by Niguès et. al is the dependency of the back-action effect on the transverse position of the beam with respect to the nanowire. Indeed, the SE response reflects the primary electrons absorption rate, which is itself proportional to the force exerted by the electron beam. As a consequence, the strength of the dynamical back-action is expected to be proportional to the gradient of the SE emission rate, $(\partial F_{ext}/\partial x) \propto (\partial I_{SE}/\partial x)$. Since this gradient can change sign depending on the transverse position of the electron beam, so can the strength of the back-action, which can possibly lead to instability of the nanowire and self-sustained oscillations. Figure 2.11 displays a line scan across the nanowire, and the corresponding derivative of the intensity signal proportional to Γ_{ba}, highlighting the lateral asymmetry of the effect. Spectra acquired at different positions show either cooling or amplification of the motion, as expected.

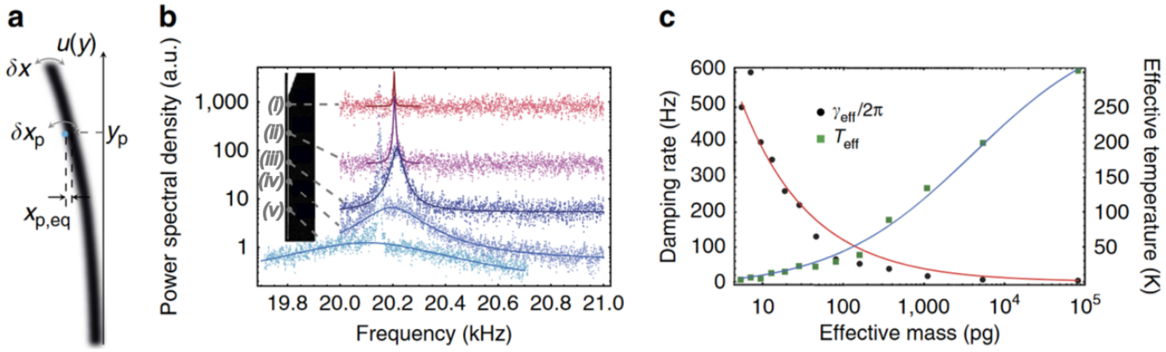

Figure 2.10: Dynamical back-action cooling with electrons. (a) Schematic introducing the notations used in the text. (b) Dynamical back-action cooling using an electron beam. The longitudinal position of the electron spot is scanned along the entire nanowire length, ranging y_p from 0 to L, with the transverse coordinate $x_{p,eq}$ being fixed. For each point, the corresponding fluctuation spectrum is recorded. The presented data are normalized to the same effective mass, to better visualize the drastic decrease of the effective temperature. Solid lines are a Lorentzian fit of the experimental data. (c) Effective temperature (green squares) and effective damping rate (black dots) as functions of the effective mass. The straight lines correspond to plots of the theoretical model (eqs. (2.92) and (2.93)), yielding $\Gamma_e(x_{p,eq}) = 604$Hz. The environment is at room temperature. Reprinted under Creative Commons license from [105].

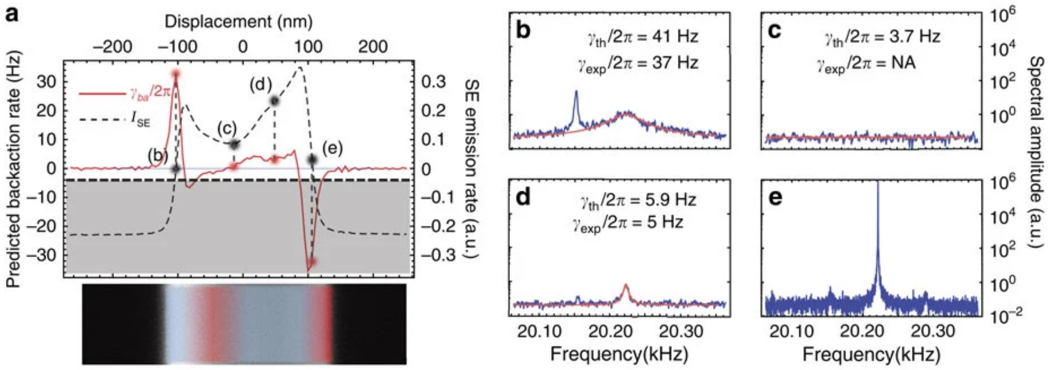

Figure 2.11: (a) Line scans of the SE emission rate (dashed, black line) and theoretically expected back-action rate $\Gamma_{ba} = \Gamma_{eff} - \Gamma_M$ (straight, red line) obtained at the longitudinal position $y_p = 40$ µm. The grey zone represents the parametric instability region, where the dynamical back-action cancels the intrinsic mechanical damping rate. Dots with abscissa (b–e) emphasize the values taken by I_{SE} and Γ_{ba} at the four acquisition spots. Heating and cooling regions are represented in red and blue on the SEM slice. Right panel: the SE emission rate fluctuation spectrum is measured at transverse positions x_p (b–e). The straight lines are Lorentzian adjustments to the experimental data. Reprinted under Creative Commons license from [105].

2.6.2 Momentum exchange

The electro-thermal effect described in the previous section is not in fact the only contribution to the back-action. It turns out that momentum exchange associated with the scattering of secondary electrons leads to back-action effects beyond the heating that arises from energy exchange.

A second experiment [107] demonstrated the presence of the momentum exchange back-action force by tracking the frequency shifts in two nearly degenerate modes of a nanowire (with circular cross-section) when the direction of the SEM beam was rotated around the nanowire. This allowed a radial back-action force to be identified which is believed to be solely due to radiation pressure effects.

The spectrum of the displacement of the nanowire was this time measured at its tip, with the electron beam aligned with the nanowire's axis. The two near-degenerate modes are visible on the spectra (see fig. 2.12b), with amplitudes depending on the position of the beam on the circumference of the resonator. Calculating the fluctuations spectrum of the SE signal and comparing the ratio of the peaks amplitude allows to identify these fluctuations to be of thermal origin, as well as to identify the directions of vibration of each mode (fig. 2.12c).

Additionally, the resonant frequencies of the modes are shifted when the electron beam is moved on the detection annulus, with a 2π-periodicity (see fig. 2.12d). This behaviour essentially reflects the contribution of temperature changes due to the residual angle of the electron beam and the nanowire, which causes variations in absorption. Finally, analyzing the splitting between the two modes reveals a π-periodicity (see fig. 2.12e), which is identified as the contribution of the radiation pressure. The detailed calculations for this result can be found in [107].

It is also interesting to note that the authors of [107] showed that this detection scheme is shot noise limited, i.e. the out-of-resonance fluctuations reflect the discrete nature of the secondary electrons. Furthermore, the displacement sensitivity of the measurement was found to be improved by a factor 2 compared with the most sensitive optical cavityless detection schemes for freestanding resonators with comparable dimensions [133]. This highlights the potential of the SEM-based setup for future ultra-sensitive measurements.

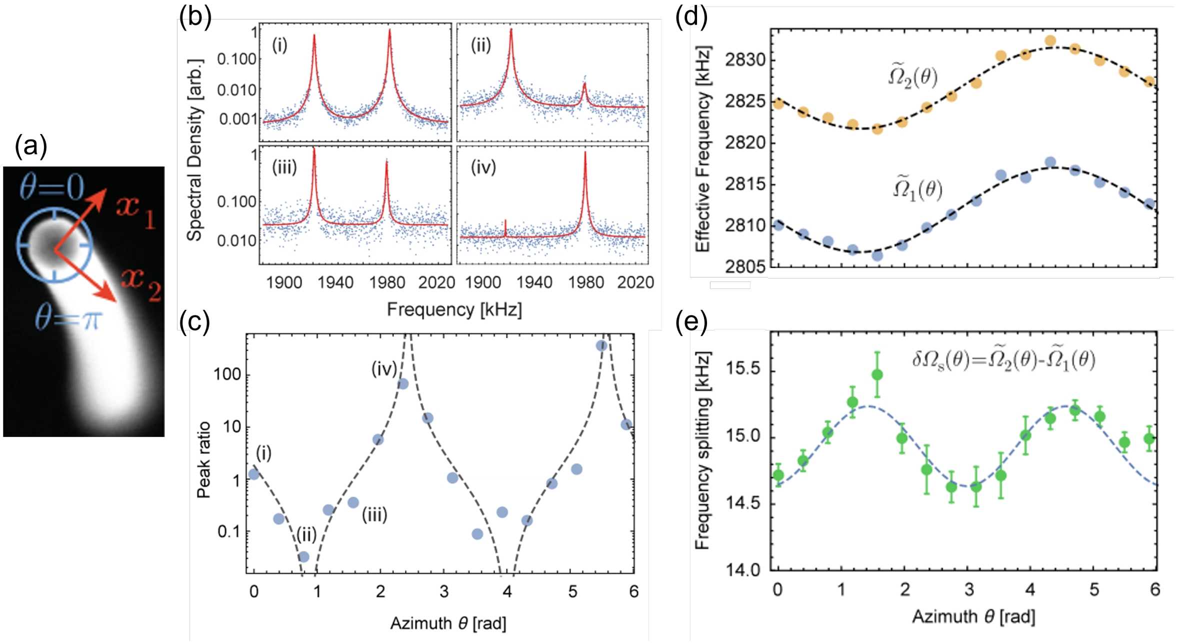

Figure 2.12: Momentum exchange and radiation pressure in a SEM. (a) SEM image of the nanowire and notations. The two directions of vibration are represented by the red arrows. (b) Four electromechanical fluctuation spectra acquired at four distinct azimuthal positions of the beam on the circumference of the nanowire [$\theta = \pi/16$, $3\pi/16$, $5\pi/16$, and $7\pi/16$ from (i) to (iv)]. (c) Ratio of the spectral amplitudes of the two peaks as a function of the azimuth. The experimental data points (dots) are fitted using a tangent squared model (dashed line), whose asymptotes enable to determine the direction of the eigenaxis of vibration. (d) Evolution of the effective mechanical resonance frequencies as a function of the azimuth. (e) Frequency splitting as a function of the azimuth. The experimental data (dots) are fitted using a π-periodic sinusoidal model, characteristic of the (radial) radiation pressure back-action force (reprinted with permission from [107].)

Estimation of radiation pressure back-action. The authors of [107] measure a radiation pressure force of 34 fN. One can then wonder how important this effect is compared with the electro-thermal effect described above, or any other back-action effect.

In this context, it is important to remember that for back-action effects, the crucial point is the delay between the force applied on the resonator and its reaction. That was illustrated in section 2.2 with the optical force λn and the relaxation rate γ of a Fabry-Pérot cavity. It is this delay that induces damping. The same holds for the electro-thermal effect, where the delay is created by the heat propagation time τ_{th}.

However, in the case of radiation pressure induced by the electron beam of a SEM, there is no cavity and therefore no delay between the force and its effect. In other words, the time scale is much faster than for thermal effects and thus no back-action damping is expected.

2.6.3 Conclusion

To summarize, we have shown that the SEM-based measurement of the displacement of a nanowire presents two important mechanisms of back-action. First, due to the very high spatial confinement of the electron beam and the highly dissipative nature of the interaction, the force gradients lead to an electrothermal effect akin to the photothermal effect observed for example in an optomechanical cavity. This effect is dependent of the longitudinal position of the electron beam on the nanowire, and acts mostly on the effective damping rate and temperature of the resonator.

Secondly, the electrons transfer a fraction of their momentum to the nanowire, creating a radiation pressure force which shifts the mechanical frequency. This contribution is dependent on the azimuthal incidence of the electron beam and thus requires us to take into account the directions of vibration of the doublet corresponding to each mechanical mode. The signature of this effect is visible in the mode splitting.

However, a number of questions remain open. How does the the cooling or heating described in section 2.6.1 relate to the description of mode temperature in section 2.5, as the dissipative nature of the interaction suggests that the nanowire is strongly out of equilibrium during the measurement ? What about the negative damping back-action? Can it lead to instabilities and self-sustained oscillations? How does the position of the electron beam along and across the nanowire impact its dynamics? Is it possible to probe higher modes, and do they reveal something new? Doe the SEM damage the nanowire, and how?

In the rest of this thesis, we will describe our progress towards the answer to these questions, relying on the tools we presented in this chapter. In the next chapter, we will discuss the experimental protocols used to explore these effects.

Chapter 3

Methods

The present chapter is dedicated to the material and methods used in this thesis, as a major part of this work was to develop new protocols and tools to carry out our measurements. We will begin by reminding the reader of the objectives of this thesis and list the requirements that they impose on our experimental setup, as well as the limits that appeared. In section 3.2, we will describe the growth protocol for the nanowires we used. Sections 3.3 and 3.4 will briefly introduce the reader to the main elements of the experimental setup, i.e. the Scanning Electron Microscope (SEM) and the Real-time Spectrum Analyser (RSA). Finally, in section 3.5 we will describe how these tools were adapted and interfaced together to work as the local probe for thermodynamical studies that we desire. Each of the successive iterations of the software lead to an adaptation of the experimental protocol that will be described.

3.1 Experimental strategy

One of the objectives of this thesis is to measure local thermodynamical properties of a nanowire subject to local heating. In order to do so, we need to record two quantities: the local temperature distribution inside the resonator, and the dynamical properties of its displacements. As exposed in section 2.5, those quantities have a very close relationship which we can use to reconstruct the distribution of losses, and hence the local temperature inside the nanowire, from its dynamics. To do so, our strategy is to use the Nanowire (NW) itself as a thermometer. A change of temperature will modify the elastic properties of the material (mostly its Young modulus), and hence modify the nanowire's resonant frequency.

However, as was demonstrated in earlier works [71–73, 109], the link between the resonant frequency and the temperature is highly non-trivial as it depends on the mechanical mode considered and the overlap between its field of displacement and the distribution of the losses inside the resonator (see section 2.5). Furthermore, the back-action mechanisms described in section 2.6 need to be taken into account since the SEM is used both for heating and measuring. To maximize the chances of uncovering the links between temperature and frequency, we will seek to measure the frequency shift of the resonances for different positions of the heating point, which we will achieve by scanning the longitudinal direction of the nanowire with the electron beam.

3.1.1 Experimental requirements

We now consider the properties that our experimental set-up needs to have in order to fulfill the strategy we have just outlined.

First of all, the measurement needs to be spatially resolved. The Scanning Electron Microscope is a perfectly suited tool for achieving this as it generates a beam of size close to a nanometre (see later, section 3.3), much smaller than the length and width of the typical resonators used in this thesis and allows relatively sharp resolution as a function of the point along the length of the wire at which the SEM beam is focused.

Secondly, the heating needs to have a large enough effect to be noticeable during the measurement. In our case, the electron beam is also used as a heating source: the incident electrons exchange energy with the sample during the inelastic collisions which generate the secondary electrons (see for example [134] for a study of this effect on a bulk sample). The heating thus generated can be estimated (see section 4.2.1). However, the electron beam also has some irreversible structural effects on the nanowire [135, 136], as will be demonstrated in chapter 4. The right balance needs to be found between those two effects.

Additionally, we also to be able to resolve the frequency shifts induced by the measurements. This sets constraints on the damping rate of the resonator on the one hand and the length of time over which the measurements are made on the other, as it takes several time the mechanical coherence time $2\pi/\Gamma$ in order to have an accurate picture of its dynamics (see section 2.1.4). This measurement time will also affect the energy exchange between the electron beam and the resonator, and the aforementioned structural effects. Once again, a compromise needs to be found between a faster (and less structurally destructive) measurement and a more accurate measurement.

In order to study the local temperature of a cantilever, one needs to be able to make measurements with the SEM focused as close to the clamping point of the resonator as possible. This is because, as shown in section 2.5, the increase of the effective temperature for each mode is strongest where the curvature of the mode shape is largest, which is at the clamping point for the fundamental mode. However, the effective mass of the resonator is proportional to the inverse of the displacement amplitude (at the point along the beam where the SEM is focused), squared (see eq. (2.70)). This means that it will diverge extremely fast as the measurement point gets closer to the clamping point, making it increasingly difficult to resolve the resonances. The very high confinement of the electron beam in the SEM is again the key advantage of our setup, as it generates a very high contrast and hence a very good sensitivity to small displacement amplitudes.

Finally, the aspect ratio of the resonator can be optimized to ensure a good sensitivity, with larger displacement amplitudes for longer and thinner nanowires. This can be seen at equilibrium from the equipartition theorem (eq. (2.20)) and the expression of the resonant frequency of a cantilever (eq. (2.68)): the amplitude of thermal displacement is proportional to $1/\Omega_0^2$, i.e. to L^4/R^2, with L the length of the cantilever and R its radius. Hence, when the aspect ratio L/R increases, the amplitude of displacement increases as well.

3.1.2 Experimental limits

For almost all of the requirements listed in the previous section, the SEM detection method generates a limitation which means that we have to find a middle ground. In this section we will list the most important ones, their origins and how they impact the measurement.

Electrothermal forces. The electron beam generates heating in the resonator, and leads to electrothermal forces which tend to bend the nanowire in one direction (see section 2.6.1). This results in an apparent lateral drift of the sample when a scan along the nanowire length is measured, thus limiting the ability to position the beam at a precise transverse position long enough for the measurement to be performed, which in turn limits the sensitivity of the measurement. Since the transverse position of the beam is such an important parameter, our solution was to measure at all positions across the nanowire, so that we make sure the maximum sensitivity is attained.

Irreversible effects of the e-beam. In addition to the possible drifts induced by heating, the measurement has a number of irreversible consequences on the structure of the nanowire. First, it is well known that the observation in a SEM generates a contamination of the sample by carbon deposition [137]. This can be mitigated by cleaning the vacuum chamber with an oxygen plasma beforehand, and this effect was in general negligible in our experiments. Another unexpected effect is an alteration of the structure of the nanowire. Indeed, it is clearly visible that the sample is etched during the measurement (see fig. 4.21), and that this effect becomes more important as the incident power and the exposure time increase. The exact mechanism involved in the process is not well understood, so we made the exploration of this effect one of the objectives of the thesis. The corresponding results we obtained are described in detail in section 4.4.

Mechanical coherence time. As was previously discussed, the mechanical properties of the nanowire fix a lower bound on the measurement duration. Indeed, in order to make sure that the dynamics of the displacement are accurately measured, it is necessary to spend a time longer than a few times the mechanical coherence time defined by $2\pi/\Gamma$ with Γ the damping rate of the resonator. This conflicts with the etching effects which require the exposure time of the nanowire to be minimized, thus the necessity for a compromise.

Parametric instability. Finally, the dynamical back-action phenomenology introduced in chapter 2 implies the presence of an instability [105]. Under certain conditions, the damping rate goes down to zero, leading to virtually infinite coherence times. It then becomes impossible to perform the thermal study that was the objective of this study. To make things even more intricate, the sensitivity to instability is enhanced by the intrinsic quality factor of the resonator [34]. Optimizing the probe power and measurement time, and finding nanowires with adapted mechanical properties to avoid this phenomenon was a main aspect of the experimental process. In parallel, characterizing the state of an unstable resonator and understanding the underlying mechanism leading to this instability was another aspect of this work, as presented in section 4.3.

3.1.3 Summary

Taking into account the requirements, and limits that have been described in the previous sections, the strategy adopted was the following. We want to preform longitudinal scans of the resonator in order to extend previous studies (section 2.5) to the nano-scale. However to ensure we get the best sensitivity we also need to scan the transverse direction. Therefore, it was decided to acquire 2D images of each nanowire under study, and to synchronize the acquisition of spectra of displacement of the nanowire with the displacements of the electron beam. This required developing a new program interfacing the spectrum analyser with the SEM, which required multiple iterations, each improving the measurement protocol. This process is detailed in section 3.5.

The probe power should be optimized for the measurement, to provide a good enough sensitivity without triggering the instabilities of the system. Similarly, the dwell time for each position of the beam should allow to probe the dynamics but not be long enough to have significant structural effects on the sample. Concerning the resonator itself, the quality factor need to be sufficient to allow the measurement, but not so large that it would lower the instability threshold and make the measurement duration excessively long. The aspect ratio need to be large enough to allow the measurement to be performed as close to the clamping as possible, but the longest an thinnest nanowires were found to be more prone to instabilities. A significant part of the experimental time was dedicated in tuning the relevant parameters to find the best compromise between all these competing effects.

3.2 Samples used

The resonators we used during this study are InAs nanowires grown perpendicularly to their substrate using the Vapor-Liquid-Solid (VLS) method. This geometry makes them very easy to place and study in the SEM, as compared to carbon nanotubes, in addition to their dimensions being in the intermediate range between CNT and larger systems previously studied such as AFM cantilevers. In this section, we will provide a quick explanation of the fabrication process, which was performed at Institut Néel (Grenoble) by Moïra

Hocevar and her student An-Hsi Chen. More details can be found in Chen's thesis [138]. We will then provide the typical properties and dimensions of the nanowires obtained during this process.

3.2.1 Nanowires growth

The VLS growth mechanism, first reported by Wagner and Ellis in 1964 [139], involves the use of Au catalysts. They consist of nanoparticles with sizes ranging from 5 to 100 nm, either drop casted on the semiconductor substrate from a colloid solution or nanopatterned by ebeam lithography.

Growth occurs by the supply of vapour of atoms or molecules in the vicinity of the heated catalyst. The atoms are incorporated into the liquid catalyst and once supersaturation is reached, they precipitate into a crystal at the interface between the liquid and the solid substrate. A continuous flow of vapour is necessary for the crystal to grow below the droplet, thus forming a nanowire. As nanowires grow in the (111) direction, we use InAs(111) substrates to produce nanowires oriented normal to the sample surface. The droplet has a double role: it collects atoms and catalyzes their crystallization.

During the growth process, the droplet is surrounded by a vapour of atoms. These atoms then have multiple paths available to reach the catalyst, shown schematically on fig. 3.1:

(i) Direct impingement to the droplet: the atoms are directly incorporated into the droplet. This path mostly contributes to the axial growth of the NW.

(ii) Sidewall diffusion: the atoms reach the side of the nanowire and can either incorporate into the sidewall, leading to radial growth, or diffuse to the catalyst and contribute to the axial growth.

(iii) Diffusion from substrate: a huge number of atoms will reach the substrate surface, before diffusing to the catalyst. This process is important during the initial steps of growth, when the side walls of nanowires are small.

Since our imaging technique requires low density of nanowires on the substrate to be able to measure each of them independently, the colloid solution was diluted prior to drop casting on the InAs(111) substrates. The samples were then inserted into the Molecular Beam Epitaxy (MBE) equipment for growth.

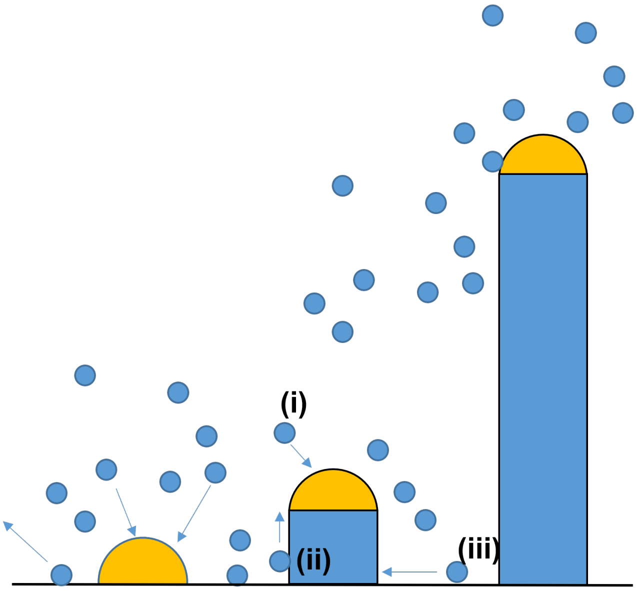

Figure 3.1: Growth process of an InAs nanowire by the VLS method. The atoms of the surrounding vapour contributed to the growth by either direct impingement (i), sidewall diffusion (ii) or diffusion from substrate (iii).

The air was pumped out to achieve ultra high vacuum, and the samples were heated up to 250℃ for further degasification. The sample is then heated to 500℃ for deoxidation, a temperature at which the catalyst droplet becomes liquid. An As_2 flux is supplied during deoxidation step to prevent roughening of the substrate surface because of As desorption above 400℃.

Once deoxidation is over, the sample is brought to 420℃ for the growth step. After opening the In shutters, nanowires start to grow. The parameters which control the growth are the flux of In, the substrate temperature (here fixed at 420℃), the V/III beam equivalent pressure ratio and the growth time.

3.2.2 Samples used in this thesis

Different geometries were tested during this work in order to meet the requirements described in section 3.1. The nanowires we studied had lengths ranging from 5 to 10 µm and diameters between 30 and 80 nm. This lead to physical masses of the order of 0.1 pg, and resonant frequencies ranging from 300 kHz to 2 MHz. SEM and TEM images of typical nanowires are presented in fig. 3.2.

The mechanical quality factor of the nanowires we studied was reliably of the order of 1000. This converted to a mechanical time $2\pi/\Gamma = Q/f_0 \simeq 2$ ms for a typical resonant frequency $f_0 \simeq 500$ kHz.

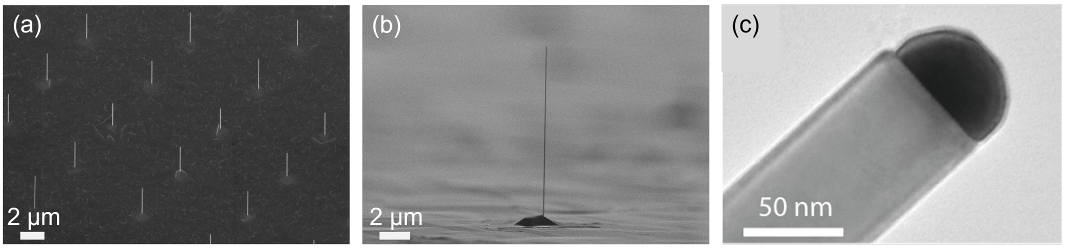

Figure 3.2: SEM (a-b) and TEM (c) images of a typical InAs Nanowires. In (a) the stage of the SEM is tilted 30°, leading to shorter apparent length, whereas in (b) the tilt is 4.7°. In (c) the dark hemisphere at the top of the nanowire is the gold catalyst. (c) is reprinted with permission from [107].

As was mentioned before, we selected longer and thinner nanowires whenever it was possible, in order to maximize the displacement amplitudes and allow for measurements as close to the clamping point as possible. The refinements of the experimental protocol also helped on this point, as the incident power and exposure time were reduced thus decreasing the risk of instability of the resonator (see section 3.5).

Fourier's model for heat transport can be used to estimate the local temperature gradient $T(y)$ reached for a given input power, taking into account the dependency of the thermal conductivity of the material to temperature. This study was performed for InAs nanowires grown in the wurtzite (hexagonal) crystalline phase, under 0.7 µW incident power and suggested that the temperature would reach up to 800 K (see section 4.2.1 for the detailed calculations), which is large enough to have very visible effects on the resonant frequency.

Other nanowires. Other types of nanowires were also tested, more or less successfully. For example, we tried GaAs nanowires, which were much shorter than our usual InAs nanowires. This lead to an increase of the resonant frequency which was an interesting prospect as it may have loosened the constraint on the dwell time necessary to acquire each spectrum. However, the amplitude of displacements was drastically reduced, and we were only able to measure the resonances on half of the length of the nanowires, which was not sufficient for our study.

Another type of sample that we tested was much larger SiC nanowires, with lengths in the 200-400 µm range. This choice was inspired by previous works describing the electrothermal back-action this system such as [105] and was intended as an intermediate scale between the AFM cantilevers which were used as a testing ground for the theoretical model and the much smaller InAs nanowires. However, the resonant frequencies of the SiC nanowires were of a few kHz while their quality factors remained well over 100, leading to increased measurement time which made our systematic study of the resonances for each position of the electron beam highly impractical, mainly due to drifts of the positional stage in the SEM.

As was mentioned in section 2.5, a key element in the modeling of the thermodynamics of nano-resonators is the distribution of losses inside the system. In the standard case of a crystalline resonator, the losses are defined by the local curvature, i.e. the second spatial derivative of each given mode. In order to reach different regimes, we tried to engineer our samples by adding a distributed source of losses. This was done by depositing in a metal evaporator a layer of gold on the InAs nanowires, either uniformly distributed of only located on one side of the sample. This amorphous layer of gold was inspired by other works such as [71], where they used tantalum pentoxide (Ta_2O_5) for this purpose. However, the nanowires treated this way seemed however to be much more prone to instabilities, and were discarded for our study.

3.3 Scanning Electron Microscope

The Scanning Electron Microscope (SEM) is an instrument which has spread in a lot of research and industrial areas since the first commercial instrument was released in 1965. It relies on the interactions of an electron beam with a sample which provides a broad range of detectors, for varied uses. In the present section we will provide a brief summary of its internal functioning. A more thorough description of its mechanisms and applications can be found for example in [140], [137] or [141] (in French).

The constituent elements of a SEM are shown in fig. 3.3, and can be summarized to the following:

- An electron gun, which produces the electrons. Different types exist, leading to output beam sizes ranging from a few nanometres to a few micrometres. The most common types use a tungsten filament, with or without a tip, the former relying on a field effect (see section 3.3.1).
- Condenser lenses and diaphragms, which product an effect similar to their optical counterparts and are used to shape the beam and control its size when it reaches the sample.

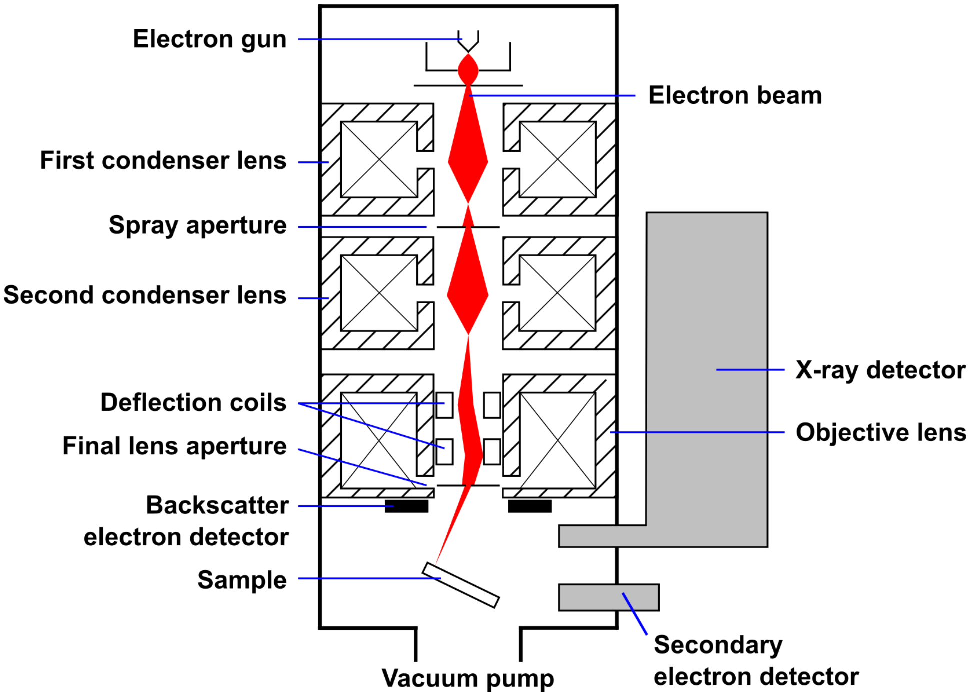

Figure 3.3: Schematics of a the major elements of a scanning electron microscope. Used under Creative Commons licence from Wikipedia).

- Scan coils, used to move the beam with respect to the sample.

- Electrons detectors, which gather the signal to actually generate the image. Multiple types of detectors can be used, depending on the type of interaction under study. More information about this will follow in sections 3.3.2 and 3.3.3.

- The vacuum system, necessary for the electron gun as well as for the column and the sample. Once again, different operating conditions exist, but for most applications ultra high vacuum is required.

3.3.1 Electron gun and lenses

The electron gun is the first element for the electronic column, responsible for the emission of electrons, as well as accelerating and focusing them. Several types of guns exist, the most common being thermionic guns and field-effect guns with either hot or cold cathode. Table 3.1 summarizes the figures of merit of different types of electron guns. Thermionic guns, which are historically the first type of gun developed, rely on a metallic filament – generally made of tungsten (W) or lanthanum hexaboride (LaB_6) – heated to extreme tempera-

Emitter type	Thermionic	Thermionic	Schottky FE	Cold FE
Cathode material	W	LaB_6	W-ZrO	W
Operation temperature (°C)	2,500	1,600	1,500	25
Effective source radius (um)	15	5	0.015[1]	0.0025[1]
Emission current density ($\mathrm{A\,cm^{-2}}$)	3	30	5,300	17,000
Normalized brightness ($\mathrm{A\,cm^{-2}\,sr^{-1}\,kV^{-1}}$)	10^4	10^5	10^7	2×10^7
Emitter lifetime (h)	100	1000	$\gg 1000$	$\gg 1000$
Emission current drift (%/h)	0.1	0.2	< 0.5	5

Table 3.1: Figures of merit of different electron guns. The first three types use a hot cathode, while the last one uses a cold cathode. The gun used in this thesis is the Schottky Field Effect W-ZrO.

tures (up to 2700 K for a W filament, 1900 K for LaB_6). The free electrons of the metal are then emitted due to their thermal motion.

In order to minimize the energy required to extract an electron from the Fermi level of a metal to a point outside the metal, another type of gun was developed: the field-effect gun. In this case, the potential barrier represented by the extraction energy is modified by applying a strong electric field. If the field is strong enough, the barrier will become thinner until eventually the electrons are able to cross it by tunneling. The main advantage of this type of guns is a theoretical brilliance up to 100 times higher than that of LaB_6 cathodes.

Finally, an intermediate type of electron guns is getting more and more common: the Schottky effect gun. It relies on both techniques, as a strong electric field is generated to lower the potential barrier, but the filament (usually tungsten single crystals coated in zirconium oxide, ZrO) is also heated close to 1700 K to lower the barrier further. An image of a typical Schottky effect gun is displayed in fig. 3.4. This is the type of electron gun present in the SEM which was used during this thesis.

As was mentioned before, the beam at the output of the electron beam has a diameter ranging from a few nanometres to a few micrometres. In order to improve the spatial resolution of the image, it is then necessary to focus the beam. This is achieved using magnetic lenses, which have a similar effect on the electron beam to that which an optical lens has on a laser beam. The magnetic lens consists of a circular coil which creates a magnetic field along the path

---

[1] Virtual source that would appear to form looking toward the gun from a point beyond the anode within the SEM column

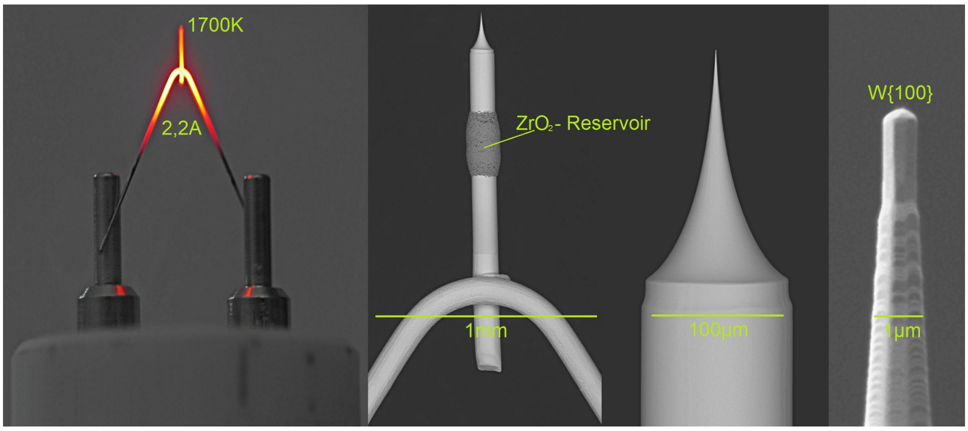

Figure 3.4: Images of a typical Schottky effect electron gun, with increasing magnification on the tip (used under Creative Commons licence from Wikipedia).

of the electrons, thus changing their trajectory accordingly. Several lenses are usually stacked to achieved the required reduction of the beam size. Due to the spherical aberration present in such lens, it can only be used in its central part, which means that the electronic column must include diaphragms, the aligning of which is critical to reduce astigmatism in the image.

3.3.2 Different imaging types

The Scanning Electron Microscope allows for a broad range of applications thanks to the multiple types of interactions between electrons and matter, as summarized in fig. 3.5. The most widely used detection type, and the one used in this work, relies on the Secondary Electrons (SE). It will be discussed in section 3.3.3.

Other types of detection include the following:

- Back-scattered electrons. These are high-energy electrons originating from the primary electron beam, and are reflected by the sample. They are mostly used for detecting different chemical species since heavier elements back-scatter more electrons, thus appearing brighter on the image.
- Electron Back-Scattered Diffraction (EBSD). This method is widely used in crystallography, to provide information about structure, crystal orientation, phase, or strain in the material. This method relies on Kikuchi bands, which correspond to each of the lattice diffracting crystal planes. If the system geometry is well known, it is possible to relate the bands

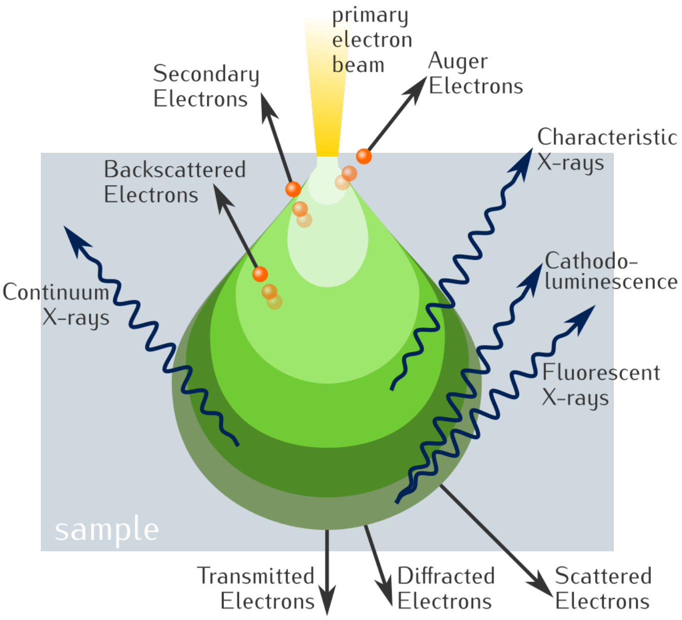

Figure 3.5: Electron–matter interaction volume and types of signal generated (used under Creative Commons licence from Wikipedia).

present in the diffraction pattern to the underlying crystal phase and orientation of the material within the electron interaction volume.

- Cathodoluminescence. When high-energy electrons interact with certain types of material (mostly semi-conductors), they can be inelastically scattered, generating secondary electrons which in turn can excite the valence electrons into the conduction band, and when these electrons recombine with a hole in the valence band, they emit photons. In the SEM, these photons will be collected by an elliptical mirror and either be used for spectral analysis or for imaging, revealing some structural properties of the material.
- X-ray analysis. When primary electrons interact with the inner shell of atoms within the sample, the inner shell electron can be ejected, thus exciting the atom in an ionized state. An electron from the outer shell will then fill this vacancy, bringing the atom back to its ground state and emitting a quantized x-ray photon. This signal can be used to map the distribution and estimate the abundance of elements in the sample.

3.3.3 Secondary Electrons and Detector

Secondary Electrons (SE) detection is the most widely used imaging method in a SEM. It relies on electrons originating from the sample, which are emitted

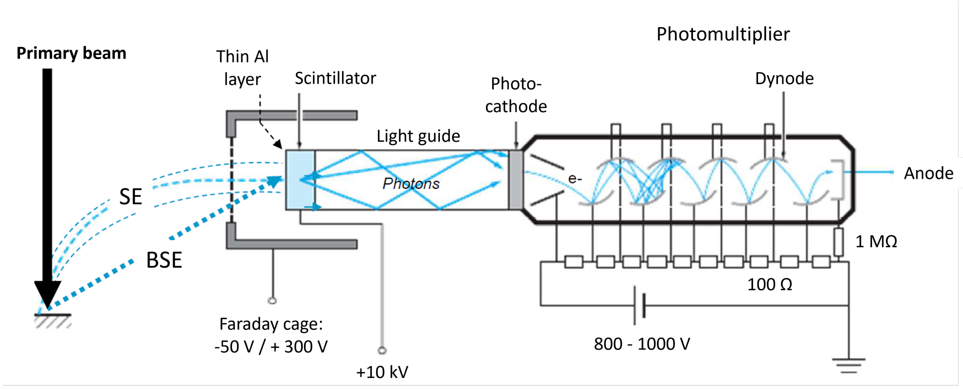

Figure 3.6: Schematic of an Everhart–Thornley detector. Back-scattered electrons are emitted in all directions, and are only collected if their trajectory takes them to the detector, whereas low energy secondary electrons are attracted by the Faraday cage.

after inelastic collisions with the incident primary electrons. Due to their weak energy (< 50 eV), only the electrons close to the surface ($\simeq$ 10-20 nm) of the material will be ejected into free space and be measured.

In order to measure these SE, the most common detector (also used for the present work) is the Everhart–Thornley detector. It uses a Faraday cage under a voltage of up to several hundred Volts to attract the low-energy SE and lead them to a scintillator, while other electrons will not be affected and only each the detector if their direction of travel takes them to it. The scintillator is under a high voltage of the order of 10 kV to accelerate the electrons and convert them into photons. These photons travel through a light guide until a photomultiplier which generates the final signal. The functioning of the detector is schematized in fig. 3.6.

The interaction of the electron beam with the sample generates multiple types of SE depending on whether they are the product of the primary electrons (SE_1), the back-scattered electrons which then interact with the sample (SE_2), or with the chamber walls (SE_3) or the diaphragm (SE_4), as shown in fig. 3.7(a).

In order to filter out the electrons that do not originate from the sample, it is possible to use the so-called in-lens, or through-the-lens detector. This device makes use of the magnetic field generated by the Field-effect electron gun, which reaches the sample and traps the SE. Due to their high initial velocity along the beam axis, they spiral up the column before being collected by an Everhart–Thornley detector placed above the objective lens, as schematized in fig. 3.7(b). This method is used to perform high-resolution imaging.

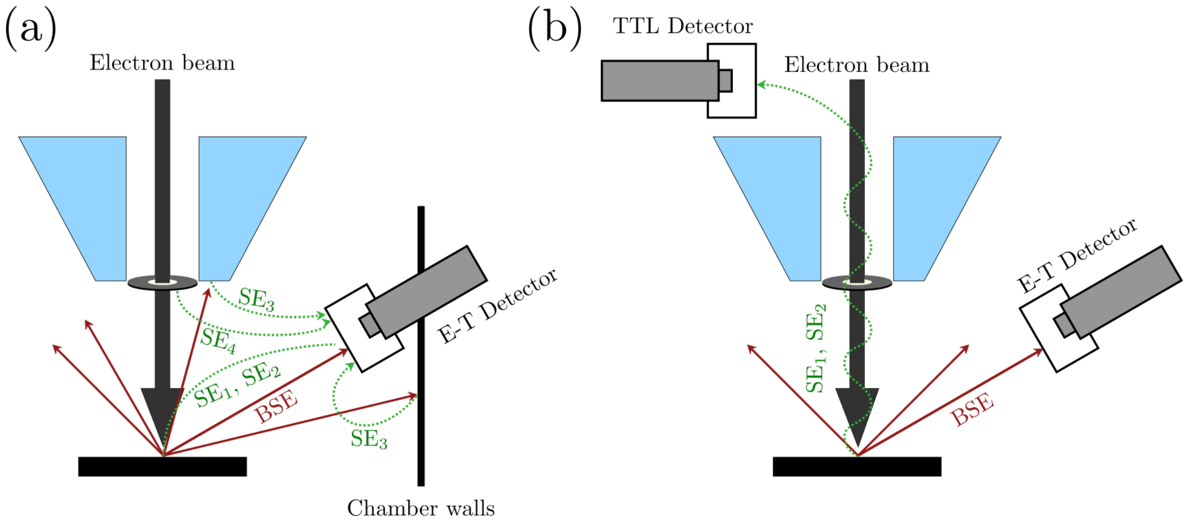

Figure 3.7: (a) Schematics of the generation of direct secondary electrons SE_1 and indirect secondary electrons SE_2 from within the specimen. Indirect SE_3 and SE_4 signals are produced when high-energy BSEs emanated from the specimen strike various microscope components inside the specimen chamber. SE_3 are generated from the walls of the specimen chamber. SE_4 signal originates from the final aperture. (b) Configuration of the in-lens detector, which improves the resolution by filtering out SE_3 and SE_4.

3.3.4 Effect of the measurement in a SEM

While the SEM is an incredibly powerful tool for imaging, a number of technical difficulties remain when imaging an object. In this section, we will list some that were – or could have been – encountered during this work, and how to circumvent them.

Sample charging

It is a well known phenomenon when studying semi-conductors in a SEM that the sample may charge, i.e. some electric charges will accumulate at some positions and subsequently disturb the trajectory of the electron beam which distorts the images acquired [137]. However, the charging can be limited by a number of techniques. Firstly, since it depends strongly on the incident current, working with lower beam intensity and acceleration voltages is beneficial. Then, the size of the sample is important, as larger samples tend to accumulate more charges. Finally, the grounding of the sample is crucial to allow charges to evacuate.

In our case, the sample is held by one or several pins that create a conducting junction to the sample holder, which is itself grounded. Additionally, the back

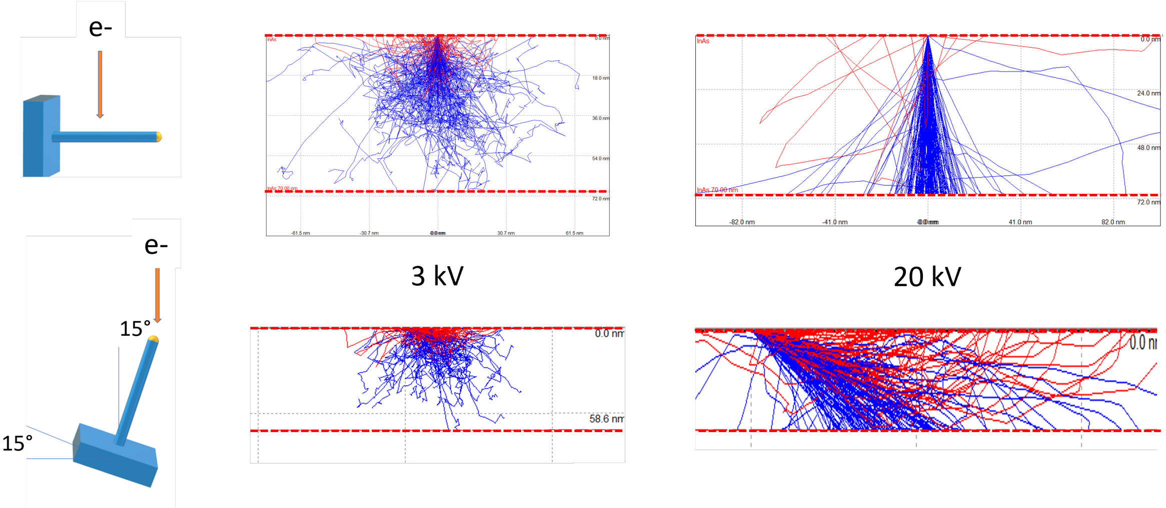

Figure 3.8: Monte-Carlo simulations of the electron-nanowire interaction, for an angle of incidence of 90° (top) and 15°(bottom). The trajectories of the primary electrons are shown in blue, the back-scattered electrons in red. The red dashed line highlight the limits of a 70 nm-thick InAs layer representing the nanowire. For a voltage of 3 kV (middle column), the interaction volume is fully contained in the nanowire for both incidences, whereas for 20 kV it is only partially contained.

side of the InAs substrate is directly in contact with the holder, thus allowing a current. Overall, by combining the methods described above, we were able to limit the effect of charging to the point where it was not perceived in our measurement.

Choice of operating conditions

The acceleration voltage and intensity of the electron beam must be chosen carefully to maximize the sensitivity of the measurement. Indeed, as the voltage increases, so does the velocity of the electrons and the volume of interaction (displayed in fig. 3.5) to the extent that it might exceed the thickness of the nanowire. This effect can be quantified by performing Monte-Carlo simulations for a slice of InAs of depth 70 nm representing the nanowire. The result of these simulations are shown in fig. 3.8 for different angles of incidence of the electron beam and voltages of 3 kV and 20 kV. The latter show that if the voltage is too large, most of the primary electrons go through the slice without interacting. In order to maximize the yield of secondary electrons, we want to avoid this phenomenon, therefore we elected to use relatively small voltages, mostly around 3 kV.

The choice of the current is also crucial, as it determines the number of pri-

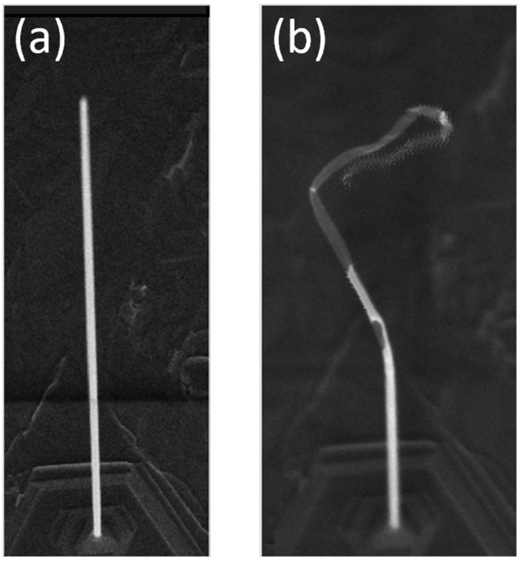

Figure 3.9: Effect of an excessive input power on a nanowire. A typical InAs nanowire before (a) and after (b) exposure to the maximal power available in the SEM. The nanowire is vaporized above a certain point, leaving only an oxide shell.

mary electrons and thus the strength of the interaction with the nanowire. As mentioned in section 3.1, a trade-off must be found between on the one hand a better signal to noise ratio when the current is high, and on the other hand the risk of altering the structure of the nanowire. Additionally, since the heating is also generated by the electron beam, we need enough current to have a detectable effect but not so much that the nanowire would be altered in a definitive way, or even destroyed.

This risk is illustrated in fig. 3.9, in which a nanowire is shown before and after exposure, at its tip, to an electron beam of maximal power ($P > 5\mu\text{W}$). The nanowire appears to have been vaporized above a certain point, which might be the point at which the melting point of InAs was reached. Interestingly, above that point it seems that a shell remains. This could be explain by the presence of an oxide layer on the nanowire [136], which did not vaporize and bends because it is much softer than the nanowire itself. The distribution of temperature inside the nanowire when exposed to the electron beam will be further discussed in section 4.2.

Joule heating

Another effect worth discussing, especially in the context of thermal studies in a SEM, is Joule heating, i.e. heat dissipation because of the resistance of the nanowires. In order to have an estimate of the amplitude of this effect, the resistance of typical nanowires were measured in collaboration with the University of Pittsburgh (measurements performed by Tasnum Reza, PhD student). The numerical result depends on the length and diameter of the nanowire considered, and varied between 2 and 16 kΩ.

The current used during this work were typically between 1 pA and 1 nA. Therefore, the power dissipated by Joule heating can be estimated, in the worst case, as $P = RI^2 \simeq 1.6 \times 10^{-14} W$ which is negligible compared to the power of the incident beam. In the rest of this thesis, Joule heating was thus ignored.

3.3.5 Cryogenic measurements

A SEM can be equipped for performing cathodoluminescence measurements. This type of measurements usually requires the sample to be cooled to cryogenic temperatures, and an elliptical mirror to gather the emission from the sample and focus it on a spectrometer. The Zeiss Ultra+ SEM we used for most measurements in this thesis was not equipped with such system, but we had the opportunity to use a FEI Inspect F50 Field-Effect Scanning Electron Microscope (FESEM) microscope. It is equipped with a liquid helium-cooled stage which let us explore the behaviour of our resonators at cryogenic temperatures, close to 4.2 K. We also studied the transitory phases during the cooling and heating of the nanowires in order to measure the dependency of the resonant frequencies on temperature. The results of this measurement are presented in section 4.3.5.

3.4 Spectrum analyser

The core signal analysis necessary for the experiments was done using a Tektronix RSA306B[1], which is a Real-time Spectrum Analyser. Its main features are the broad spectral range – 9 kHz to 6.2 GHz – which we chose because of its ability to study low-frequency signals, and the dynamic range from -160 dBm to +20 dBm. The versatility of this tool was very useful as, on top of being very affordable compared to other spectrum analysers, it allowed for multiple acquisition modes including averaging, recording full spectrograms, simultaneous measurements over multiple frequency ranges and quadrature demodulation.

---

[1] see https://www.tek.com/en/products/spectrum-analyzers/rsa306 for complete documentation and specifications.

Although a detailed guide on the fundamentals of RSA can be found online [142], we will provide a brief summary in the present section.

The RSA is a relatively recent technology, as opposed to more classical systems which either demodulate a signal around a frequency swept across a given range (Swept Signal Analysers) or perform a Discrete Fourier Transform (DFT) on a signal recorded over all the pass-band of the instrument (Vector Signal Analysers). Those systems provide a good dynamic range, with additional information about the phase for VSAs, but are unable to account for transient effects, either because they happen out of the frequency range corresponding to a given point for SSAs or because they happen during the processing time of the VSAs.

On the other hand, to analyse signals in real-time means that the analysis operations must be performed fast enough to accurately process all signal components in the frequency band of interest. This definition implies that we must both sample the input signal fast enough to satisfy Nyquist criteria (sampling frequency exceeding twice the bandwidth of interest) and perform all computations continuously and fast enough such that the output of the analysis keeps up with the changes in the input signal. This is achieved by performing the signal analysis prior to storing the signal in memory (as opposed to post-acquisition processing for the VSA). The data in memory can then be extensively analysed in multiple domains using batch processing. The differences between those methods are summarized in fig. 3.10.

Resolution Bandwidth (RBW) on the RSA. On traditional SSAs, the RBW determines the ability to resolve adjacent signals. For example, in order to resolve two signals of equal amplitude and 100 kHz apart in frequency, RBW needs to be less than 100 kHz. For spectrum analysers based on the DFT technique, the RBW is inversely proportional to the acquisition time, as discussed in section 2.1.4. Given the same sampling frequency, more samples are required to achieve a smaller RBW. In addition, windowing also affects the RBW. Indeed, the mathematics of DFT assume that the data analysed is a single period of a repeating signal. However, in reality this may cause discontinuities which generate spectral artifacts called spectral leakage. This phenomenon is illustrated in fig. 3.11.

The RSA minimizes this issue by multiplying the DFT frame by a window function that is the same length sample by sample. The window functions usually have a bell shape, reducing or eliminating the discontinuities at the ends

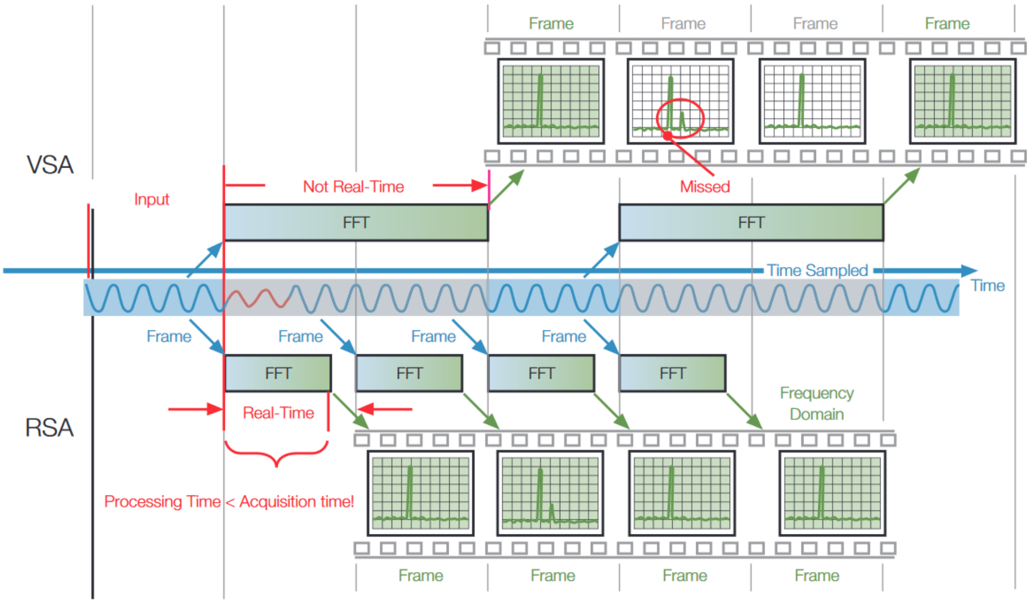

Figure 3.10: VSA processing vs. Real-Time Spectrum Analysers real-time engine processing. Since the processing time is shorter than the frame acquisition time, the transient effects are accounted for in a RSA, whereas in a VSA the calculations being done after the acquisition means that the transient signals can be missed. ©Tektronix

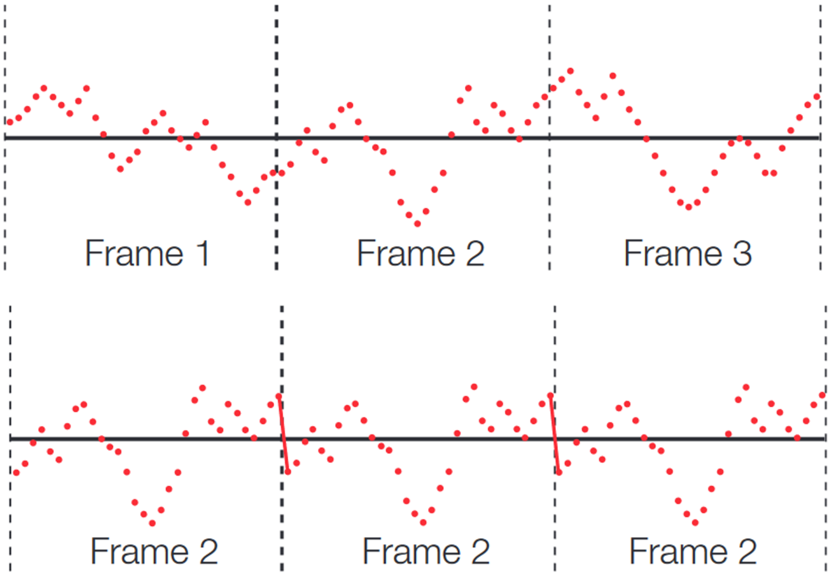

Figure 3.11: Discontinuities caused by windowing in a spectrum analyser. Top: the temporal signal is divided in frames. Bottom: when the periodic extension is applied to Frame 2, it creates discontinuities. ©Tektronix

of the DFT frame. The choice of the function depends on the characteristics of the signal and the type of analysis performed by the user. The default one provided with the RSA306B is the Kayser window, defined for a discrete signal of size N by [143]:

$$w[n] = \begin{cases} I_0\left[\beta\sqrt{1-\left(\frac{n-N/2}{N/2}\right)^2}\right]/I_0[\beta] & \text{if } 0 \leq n \leq N \\ 0 & \text{otherwise} \end{cases}$$

where I_0 the zeroth-order modified Bessel function of the first kind and β is a parameter that determines the shape of the window: in frequency domain it determines a trade-off between width of the main lobe and the level of the side lobes.

The window function determines the effective RBW, defined as the 3 dB bandwidth. It is related to the sampling frequency and samples in the DFT as follows:

$$RBW = \frac{k\ F_s}{N} \tag{3.1}$$

$$N = \frac{k\ F_s}{RBW} \tag{3.2}$$

where k is a window-related coefficient, N is the number of time-domain samples used in the DFT calculation, and F_s is the sampling frequency. For the Kaiser window used by this instrument (defined by $\beta = 16.7$), k is about 2.23. Equation (3.2) can be used to calculate the required number of samples for the DFT based on the input span and RBW settings.

Discrete Fourier Transform. In order to spectrally analyse a continuous signal $x(t)$, it is necessary to discretize it into a set $\{x[n] \mid n = 0 \,..\, N-1\}$ corresponding to the frame of acquisition. The DFT is then defined as:

$$X[\Omega] = \sum_{0}^{N-1} x(n) e^{-i\Omega n/N} \tag{3.3}$$

Although the input is a discrete function of n, the output is a continuous function of the frequency Ω.

Various practical methods exist to implement the DFT. The most commonly used are the Fast Fourier Transform (FFT) and the Chirp-Z Transform (CZT), the latter being the one employed in the RSA306B because of its greater flexibility in choosing the frequency range and the number of output points, even though it requires more computations than the FFT.

Digital Signal Processing. The DSP is the key element making the Real-time Spectrum Analyser possible. It includes a number of digital filters to select or reject frequencies depending on the application. This is achieved mathematically through the use of Finite Impulse Response, which emulates the impulse response of the desired filter transfer function with a discrete-time approximation that has finite time duration. Signal filtering is then performed by convolving the input signal with the impulse response of the filter, which is equivalent to multiplying the frequency domain spectrum by the filter thanks to Fourier theory.

In the case of the RSA306B, DSP is performed on an external computer. This was intended in the design of the instrument in order to have a light, transportable and power-efficient system. However, this comes at the cost of reduced computational capacity, as the laptop processors are less efficient than dedicated hardware. This means that the minimal length necessary for a pulse to be detected with a 100% probability is limited by the computer. As portable computer processing power increases (including implementation of GPUs for fast graphics processing), this number will be reduced (it was 100 µs in 2015, now 150 ns).

For the basic applications of the RSA, the software SignalVu provided by Tektronix is perfectly suitable, as it is able to perform the usual tasks required of a spectrum analyser. However, for more complex tasks it is necessary to create a new program using the Programmer's Interface provided. The signal processing program developed for the experiments discussed in this thesis is the topic of the next section.

3.5 Software developments and instruments interfacing

The process of measuring the nanowires produced a huge amount of data, which required a significant amount of post-processing in order to extract useful information. These processes evolved as the measurement process improved. In this section we will describe the different generations of measurement protocols

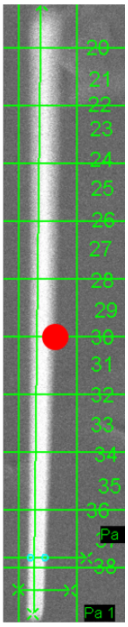

Figure 3.12: Early measurements: the beam is manually placed using the spot mode of the SEM (symbolized by a red dot here). To place it at equally spaced longitudinal positions, a grid is used.

and associated post-processing.

3.5.1 Early measurements: manually placed spot mode

The very first measurements made in this project were taken using a manually placed electron beam, simply by using the SEM in spot mode. It was placed at the edge of the NW, for relevant longitudinal positions. To ensure an equal spacing between points, a grid was used (provided by the SEM imaging software) as illustrated in fig. 3.12. The lateral position was then adapted to maximize the sensitivity of the measurement and the height of the resonance peaks measured on the spectrum analyser.

For each position, we thus obtained a spectrum, which was fitted with a double Lorentzian shape to extract the resonant frequency and the other parameters of interest (amplitude, damping rate...). This was carried out using a python script written by myself, using standard python libraries (numpy and scipy, mainly).

3.5.2 Second generation: “Hyperspectral Imaging”

The previous method gave promising results, but had many flaws. First of all, it was time-consuming: the position of the spot had to be fine-tuned for each desired measurement position, which proved tricky at best. It also made the measurement sensitive to position drifts of the stage holding the sample, if the spectrum analyser was parameterized to use a longer average time, or a lower Resolution Bandwidth (RBW). More precisely, we tried to place the beam at the edge of the nanowire, where the contrast and the peaks amplitude are maximal. However, due to the drifts of the system we would loose this sensitivity and end up with a degraded signal, i.e. the uncertainty in the actual position of the beam with respect to the nanowire was important, both in the longitudinal and transverse axes.

It was then decided to interface the spectrum analyser to allow a continuous acquisition while the position of the electron beam was scanned across the NW, with the longest dwell time at each position available. The results of this preliminary measurement are displayed in fig. 3.13. The dependency of the measurement sensitivity to the lateral position is clearly visible through the amplitude of the peaks (right panel). This is a confirmation of the dependency of the sensitivity of the measurement of motion on the contrast of the image, i.e. the spatial derivative of the intensity of the SE signal (see section 1.5 and eq. (1.3)).

What was more surprising is the dependency of the frequency to the lateral position, with seemingly a dip when the SEM was aligned in the middle of the NW. This is attributed to heating, and will be further explored in section 4.2. These results were encouraging and justified developing the full program for a complete two-dimensional image of the nanowire.

Principle of the software.

The idea was to be able to continuously acquire spectra as the electron beam scanned the NW. However, due to the lack of flexibility of the software provided by the manufacturer of the SEM, it was not possible to actually synchronize the spectrum analyser with the electron beam. The workaround we found was to set the dwell time of the SEM – the time the beam remains in position for each pixel – to the longest available value, 32 ms, while we tuned the parameters of the spectrum analyser to ensure an averaging time shorter than this for each

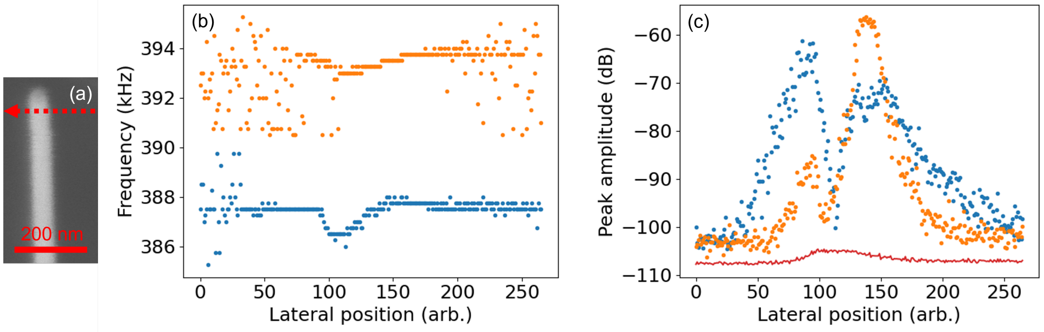

Figure 3.13: Preliminary measurement for continuous acquisition. (a) Magnified SEM image of the tip of the nanowire. The red arrow indicates the direction of the scan. (b) Evolution of the peak frequency for the two nearly degenerate modes (blue and orange dots) of the NW. (c) Evolution of the amplitude of the peaks (blue and orange). The red curve is the out-of-resonance amplitude, useful for locating the nanowire.

spectrum. The time stamp of each spectrum was also recorded by the script.

In order to link each spectrum with its corresponding position on the image, we needed a reference. This was provided by output voltages from the SEM which were proportional to the X and Y positions and the SE signal, and were recorded using a multi-channel oscilloscope.

The output of the measurement consisted of three files: the compiled spectra (which we named the spectrogram), their respective time stamps and the traces of the oscilloscope containing the data of the image. The total represented a memory size of roughly 300 MB for each scan of the NW. This huge size made the handling of data impractical, so I created another script to extract the useful information from the raw data. This information included the resonant frequencies, damping rates and amplitudes of the peaks at each position where a peak was actually measured. Additionally, one problem remained: the timebase of the spectrogram and the oscilloscope were not synchronized. This had to be assured during the post-processing.

Post-processing of the data.

The first step of this process is to synchronize the time axis between the spectrum analyser and the DC signal. In order to do so, we use the fact that the out-of-resonance noise level is proportional to the shot noise of the SE signal (i.e. the detection is shot noise-limited, as shown in [107]), which in turn is proportional to the DC signal. We can then reconstruct an equivalent image to

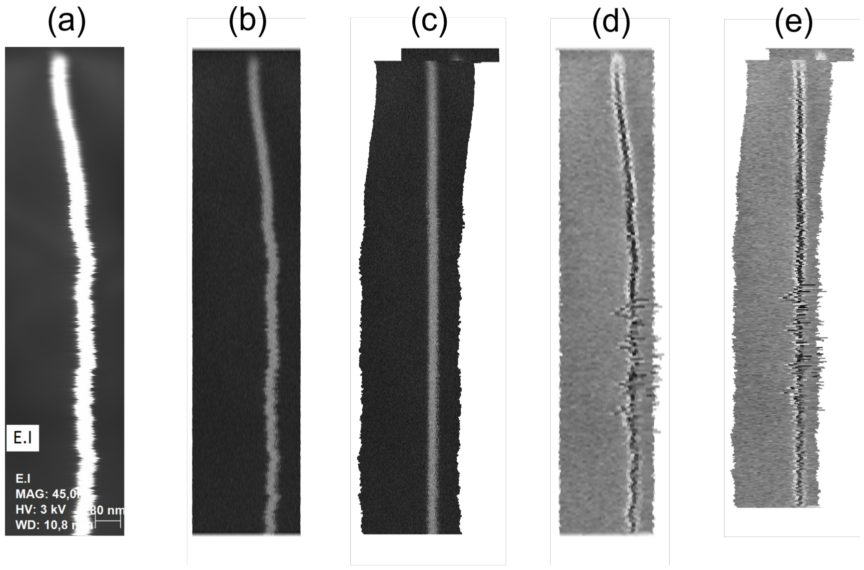

Figure 3.14: Different steps of the image reconstitution process. (a) The SEM image acquired by the software controlling the acquisition. (b) The image reconstructed from the DC level recorded on the oscilloscope. (c) The image after the drift correction assuming the nanowire was upright. The process relies on the detection of the edge of the nanowire, hence the shift at the top of the image. (d) and (e) The equivalent images from the out-of-resonance noise level on the RSA.

the one acquired by the SEM using the noise level and we have clear indicator of the passage of the electron beam across the nanowire.

We can usually correct the drifts that occur, because the lateral drifts we suffered from were mostly global drift of the sample, and the bending we noticed happened along the direction of the beam. In order to do so, we use the high contrast of the image to locate the edge of the nanowire for each line and shift the line accordingly. The reconstruction of the SEM image from the raw data and the synchronization with the spectrum analyser are summarized in fig. 3.14.

Finally, the resonant frequency needs to be extracted for each spectrum. A rough estimate can be extracted by taking the maximum of the spectrum if it is above a given threshold to make sure we actually measure a peak corresponding to the motion of the resonator and not some random noise. Alternatively, if the RBW of the spectrum analyser is low enough and the number of points is high enough, we can perform a Lorentzian fit for each peak. This approach gives more insight into the dynamics of the nanowires as it also gives access to the damping rate and the amplitude of the modes. This implicitly assumes that the system is linear, which is generally true except in some cases which will be discussed further in section 4.3.

Limitations of this method.

However promising, this method still had a number of flaws. On the data treatment level, the synchronization of the time axis was never perfect, and required a manual fine-tuning for each dataset, which lead to imprecision in the position corresponding to each spectrum. The criteria to detect the edges of the NW was not perfect and could be perturbed by inhomogeneities of the substrate. This caused the distortions visible in fig. 3.14d and e.

From the measurement itself, the acquisition rate of the spectrum analyser was not constant, which made choosing the averaging time difficult. We had to rely on longer dwell times to make sure that we had at least one spectrum per pixel. This made the total acquisition duration very long, which made the accumulation of data tedious for the experimentalist, but had another unforeseen consequence: the amount of energy deposited within the nanowire by he SEM was increased for each pixel, which lead to excessive heating and etching of the sample. These effects are explored further in sections 4.2 and 4.4.

3.5.3 Third generation: ViBR software

All the previously discussed problems could be solved if we could synchronize the electron beam with the spectrum acquisition during the measurement process, which was not possible with the SEM manufacturer's software. It was then decided to create our own acquisition software, which would control both instruments, and give the beam at a given position the exact time needed to acquire a spectrum, before moving on to the next pixel. In this context, an intern from IUT Grenoble, Thomas Gilibert, was hired by Institut Néel and supervised by Sabine Douillet, technical engineer, in order to help me design the software – subsequently named ViBR. They took care of the technical implementation in LabView while my role was the design of the specifications.

This software successfully tackles all the issues listed in the previous sections, notably decreasing the acquisition time down from over one hour to around 10 minutes. But it also did more: it allowed for a lot of flexibility by making the measurement possible up and down the nanowire, separately or as a round trip, without needing to physically turn the sample in the vacuum chamber. The first iterations of the software attempted to automatically detect the resonant peaks and to set the parameters of the spectrum analyser accordingly. However, this feature was not retained in the later versions as it often failed to set the

RBW. Instead, we opted to manually choose it. It is also possible to sequentially measure several nanowires, in a fully automated way. This will be useful in order to systematically characterize a batch of nanowires for example. Finally, the last version of ViBR lets us choose one peak among a list of detected frequencies, which for example lets the user lock onto the higher order mechanical modes.

The primary acquisition is done by plugging into the SEM directly using National Instrument's DAQ NI-USB-6363 board to make the physical interface between the software and the SEM and send it the appropriate voltages to control the beam position. The same type of programmer's interface tools as for the previous scripts are used to communicate with the spectrum analyser, and ensure a spectrum is acquired with the proper parameters before moving the beam to the next position.

Measurement process.

Once the sample is installed in the SEM, the vacuum pumped and the focus of the image assured, the procedure to measure a nanowire is as follows. First a preliminary, wide range image is taken. The user will then select one or several ”boxes” in which the actual acquisition is taken. This is useful to maximize the ratio between the number of useful pixels (on the NW) and the total size of the image, since a spectrum will be acquired anyway. The user will decide the resolution , i.e. the size of the step between each pixel during the measurement. Typically, we aimed for around 20 points inside the nanowire for each line (so pixel width $\simeq$ 2 nm) and 15 to 30 lines in the image, to ensure a good compromise between the duration of the acquisition and the spatial resolution of the measurement.

The software then performs a quick acquisition of a few lines close to the free end of the nanowire with a broad RBW and a large frequency range, in order to identify the resonant peaks. The user can then choose on which peak to ”lock” the acquisition, and the frequency range recorded around this peak, as well as the RBW. ViBR will then handle the measurement itself, and save the spectrogram along with the positions corresponding to each spectrum, and the image in SE signal.

During the measurement, an option can be activated to correct any drifts that might occur. This is based on the primary, broad image: at regular time intervals, ViBR will acquire the same image, then compare a few zones out of the nanowire to detect a position drift and correct them. Note that this only corrects global drifts of the sample, and not bending of the nanowire for example.

3.5.4 Measuring the higher order modes

A key point that emerged during our measurements was the ability to measure the higher order mechanical modes of the nanowire. The ability to choose which mode it could lock on, which let us do just that, was added in one of the latest versions. However, we were still only able to measure a single mode at any one time. This was a huge limitation because the nanowire is irreversibly changed during the measurement, as we will see in chapter 4. Measuring for instance the first mode then the second mode in succession is not equivalent to doing it in the other order.

However, we were able to circumvent this issue by using a second RSA, and splitting the output signal of the SEM thanks to a homemade power splitter provided by the electronic workshop of Institut Néel. One of the RSAs was then plugged into ViBR (which controlled the electron beam), and measuring one of the desired modes. The second used the method presented in section 3.5.2, relying on a python script to acquire spectra continuously with frequency ranges set manually.

This protocol was tested with the first two mechanical modes, and the results are presented in chapter 4. One of the main difficulties came from the difference in amplitude of the two modes, as the second has a much smaller amplitude. This signal was further decreased by splitting the power. In order to minimize this issue, the power splitter was designed so that 90% of the signal was sent on the RSA which measured the second mode and 10% to the RSA measuring the fundamental mode. The sensitivity of the measurement was sufficient so that 10% were enough to measure the fundamental mode reliably. Note that which mode was measured with the RSA connected to ViBR is not critical, as long as the higher order mode was fed with 90% of the total power.

Chapter 4

Results and discussion

The previous chapters described the theoretical background necessary for this thesis, and the experimental methods used. In the present chapter, we will describe and discuss the results we obtained by applying them. We will begin in 4.1 by describing the type of data typically obtained in our measurements, and showing how even the preliminary outputs such as an SEM image contain useful information on the dynamics of a nanowire. As we will then see in section 4.2, having a deeper understanding of thermal transport in the nanowire is possible using these data. Section 4.3 is focused on how dynamical back-action affects the measurement. We will describe the state of a self-oscillating nanowire and how the measurement can be affected by such large amplitudes of displacement. We will then propose a model based on thermo-mechanical effects, and discuss how they can be minimized. Finally, in section 4.4 will then present different models for the internal temperature of the resonator, starting from a naive approach and refining it by including local etching of the nanowire, which was detected in our measurement.

4.1 Output of a measurement

The first section of this chapter will be dedicated to the primary outputs that an SEM-based measurement can provide, even before applying the full protocol described in chapter 3 and doing scans on the nanowire. As we will see, an SEM image itself, and a spectrum of displacement of the resonator both provide insight on the dynamic behaviour of the system.

4.1.1 SEM image of an InAs nanowire

Before considering scanning a nanowire to extract its temperature profile, or even measuring its position fluctuations and their spectrum, it is a practical necessity to image the system. As we will see in this section, this simple fact, even with very standard operating conditions, provides signatures of the dynamical effects of the electro-mechanical interaction between the electron beam and the resonator.

To explain this, it is necessary to recall the way an SEM image is acquired. Contrary to a conventional photography in which the whole sample is illuminated, and the reflected photons are gathered by a detector, here the electron beam is scanned across the sample, and what we measure is the result of their interaction, at each position and for a duration – the dwell time of the beam – defined by the operator. In a way, in an SEM, one does not image the object, but the interaction between the probe and the object.

Now if the object considered is of nanometric dimensions, it is necessary to use a probe with a sufficient resolution, typically smaller than its width and length. This implies that the density of power received by the sample increases dramatically because the electron beam needs to be very tightly focused. Furthermore, nanometric objects are known for having a capacity of absorption (and dissipation) of heat much smaller than bulk materials. This may induce alterations of the behaviour of a resonator, damage or destruction of the sample, as is known to the imaging community [136]. However, in the context of nanomechanics, the dynamical effects associated with SEM imaging have remained mostly unknown, and are still often ignored.

Impact of dwell time on an SEM image. The reduced cross-section of nanometric objects (and in particular nanowires) forces the use of longer exposure times for optical imaging, or dwell time for the SEM. However, in the case of a nanoresonator, increasing the dwell time increases the effective incident power and leads to dynamical effects on these objects.

An example of such effects is presented in fig. 4.1. The first micrograph was acquired with a relatively short dwell time (a few hundreds of microseconds), while for the second the dwell time was 32 ms. In this case, the nanowire appears widened. These are actually areas in which the dynamical back-action drives the resonator into instability, with a lateral asymmetry similar to that which was presented in section 2.6.1. While this effect can seem similar to the

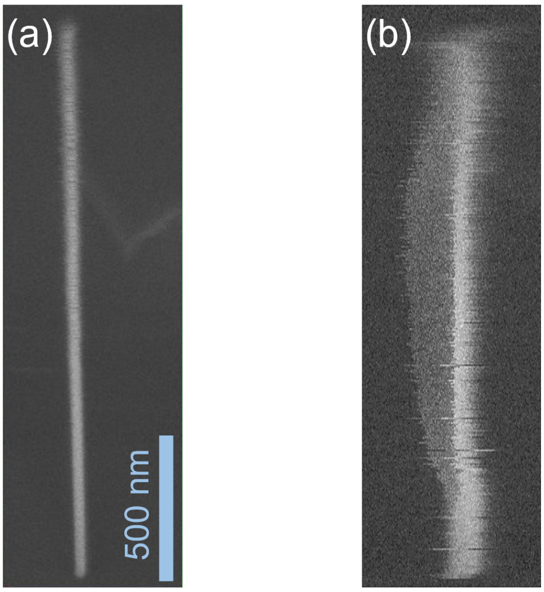

Figure 4.1: Impact of dwell time on an SEM image of a nanowire. (a) Fast image of an InAs nanowire. The free end of the nanowire (top of the image) is slightly out of focus due to the angle of incidence of the beam (15°). The lateral asymmetry due to back-action is not visible with such a short dwell time. (b) Slow image of the same nanowire (corrected to straighten the nanowire as presented in section 3.5.2). The left side is significantly more blurry due to dynamical back-action.

blur occurring when trying to take a photograph of an object moving at high speed with a long exposure time, we should remind once again that it is very different. Indeed, here the nature of the vibrational state of the resonator is directly changed by the electron beam which drives the resonances, which leads to instabilities. This topic will be more thoroughly discussed in section 4.3, but we see here that an image alone can be enough to detect dynamical back-action, and that the simple fact of imaging a resonator can have drastic consequences on its dynamics. Additionally, we see in fig. 4.1 another signature of the dynamical back-action effect described in section 2.6.1: the widening effect is more important on one side of the nanowire, revealing the lateral asymmetry of this effect.

4.1.2 Spectrum

A main objective of the present work is to add an extra dimension to SEM imaging, by recording, on top of the intensity of the SE for each point of the image, the corresponding spectrum of fluctuations. This spectrum contains a range of additional information, potentially related to temperature, mass, local composition of the sample, thermal conductivity, etc. A spectrum is therefore

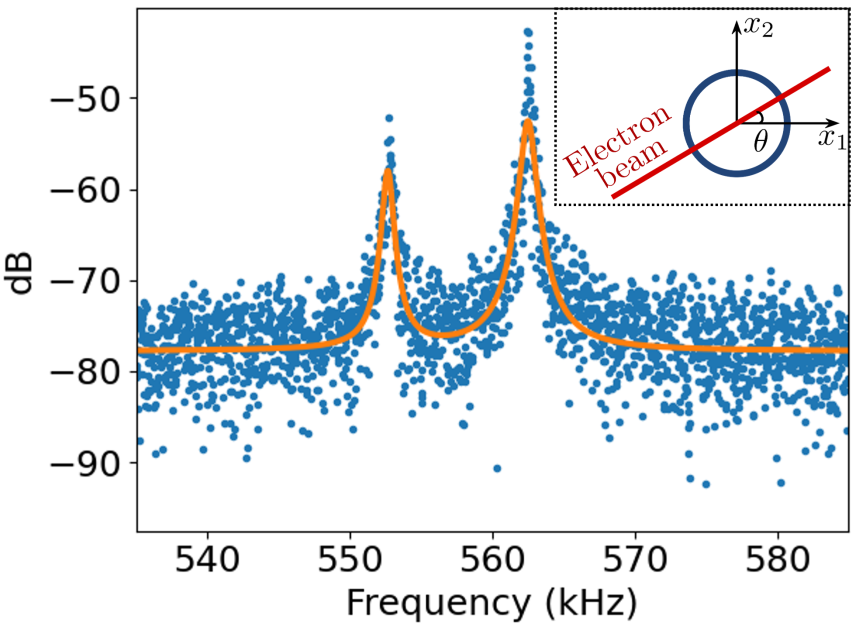

Figure 4.2: A typical spectrum, acquired with a RBW of 20 Hz during $\simeq$ 200 ms. The orange line is a fit with a double Lorentzian-shaped function. The inset schematizes a top view of the nanowire, where the directions of vibration x_1 and x_2 define an angle θ with the electron beam, which in turn defines the relative height of the two peaks.

acquired at each position along the length of the electron beam, and fig. 4.2 shows a typical spectrum of an InAs nanowire, with the associated fit.

As expected from sections 2.1 and 2.3, the spectrum presents two resonant peaks, corresponding to the two directions of vibration. Each of these peaks has a Lorentzian shape, as highlighted by the fit, in very good agreement with the data. This fit is characterized by three values: the resonant angular frequency Ω_0, the damping rate Γ and the amplitude of the peak A. The first two can be used to determine the mechanical quality factor of each mode (typically, $Q \simeq 1000$ in our experiments), while the latter is related to the sensitivity of the measurement as well as the amplitude of displacement of the nanowire at the position of the measurement beam, as illustrated in fig. 4.3. As was presented in section 1.5, the sensitivity of the measurement is directly proportional to the absolute value of the gradient of the image in the direction of vibration (the x axis in our case), $\partial I/\partial x$, which is maximal at the edges of the nanowire. This explains why the resonances of the nanowire are only detected when the electron beam is placed in these positions. Additionally, as the detection beam gets closer to the clamping point of the nanowire, the amplitude of displacements decreases exponentially (or equivalently the effective mass of the mode

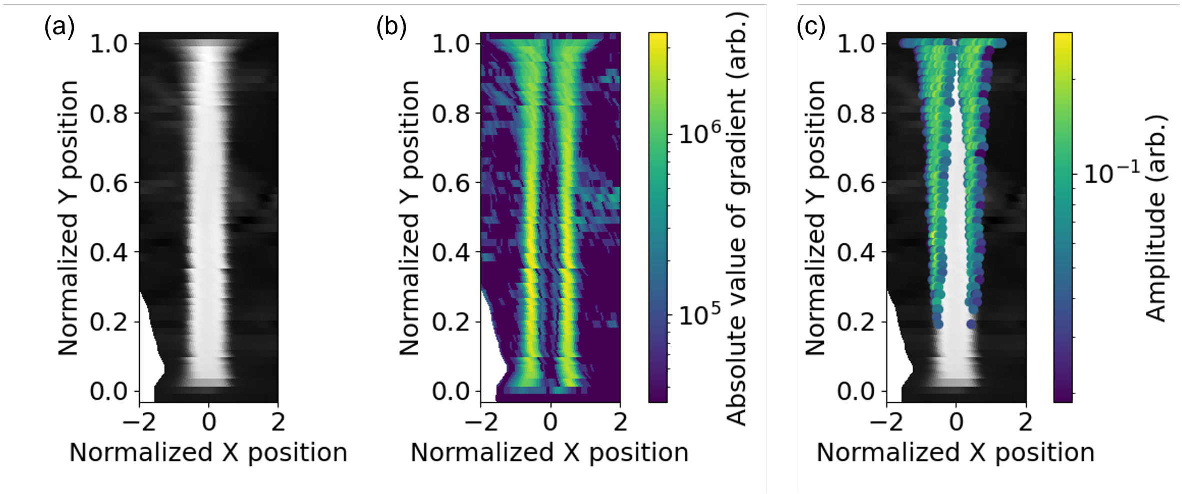

Figure 4.3: Sensitivity of a measurement. (a) Raw image of a typical measurement. (b) Logarithmic plot of the gradient of the previous image along the x-axis. This quantity is directly proportional to the sensitivity of the measurement. (c) Amplitude of one of the modes, as a function of the beam position. The amplitude depends both on the sensitivity (hence the higher amplitude at the edges of the nanowire) and on the amplitude of displacements (hence the loss of signal close to the clamping at y=0).

increases), which leads to smaller and smaller peaks.

The ratio between the heights of the two peaks gives information about the directions of vibration relative to the axis of the electron beam. Indeed, as explained in section 2.3, each mechanical mode of a vibrating beam is a doublet corresponding to two orthogonal directions determined by the geometry of the resonator, and the displacement measured is actually a projection of the motion of the nanowire on the plane orthogonal to the electron beam. If the electron beam is not aligned with one of the directions of vibration, both modes are visible, with a reduced amplitude proportional to the sine of the angle they define with the beam for one, and the cosine of this angle for the other [107] (see inset of fig. 4.2).

As was explained in section 2.1.4, in order to have a full characterization of the dynamics of the resonator, it is necessary to measure its vibrations for a duration several times larger than their characteristic time $2\pi/\Gamma$. A preliminary measurement of the resonance might be necessary to have an estimate of the appropriate RBW required to measure the spectrum. This is a crucial point as it gives a lower bound to the dwell time of the electron beam in each position, thus putting a lower limit on the overall duration of a measurement and impacts the appearance of instabilities, as we will see in section 4.3.

4.2 Effects of heating on the mechanical properties of the nanowire

A question arises from the presence of peaks in the spectra presented so far: are they due solely to the Brownian motion of the nanowire, or are they a consequence of the interaction with the electron beam? Indeed, electron microscopy is a technique in which the probe is almost completely absorbed, which generates heating. In typical working conditions (voltage of the order of 1 kV and current of a few hundreds of pA), the incident power on the sample is of the order of 1 µW. In this case, a model based on Fourier's physics predicts an increase of temperature of several hundred kelvin, as we will see in the following section. This heating would have important effects both on the crystalline structure of the resonator, its aspect ratio (through thermal expansion) and on the material constants such as Young's modulus. Additionally, the deformations induced by heating lead to a shift of the resonant frequencies of the nanowire [105, 107].

In the present section, we will present a more rigorous model for thermal transport inside a nanowire, and how its resonant modes are affected.

4.2.1 Model of "mode temperature"

Previous works have demonstrated that the temperature experienced by each mechanical mode of a resonator can be different from the local temperature distribution inside it [71–73, 109]. In this section, we will first see how one can use Fourier's Heat Equation to calculate the local temperature, and how it differs from the temperature experienced by the first mechanical modes. This model is the result of a collaboration with Ludovic Bellon's team in Lyon, and in particular by his former student Alex Fontana.

We will assume a one-dimensional nanowire of length L that lies along the y axis, with a circular cross-section of diameter D. The thermal conductivity of the material is $\kappa(T(y))$, which is a function of temperature and hence of the local temperature $T(y)$. The electron beam is a Gaussian beam of waist w perpendicular to the axis of the nanowire.

Assuming a steady state has been reached, the heat equation for this system

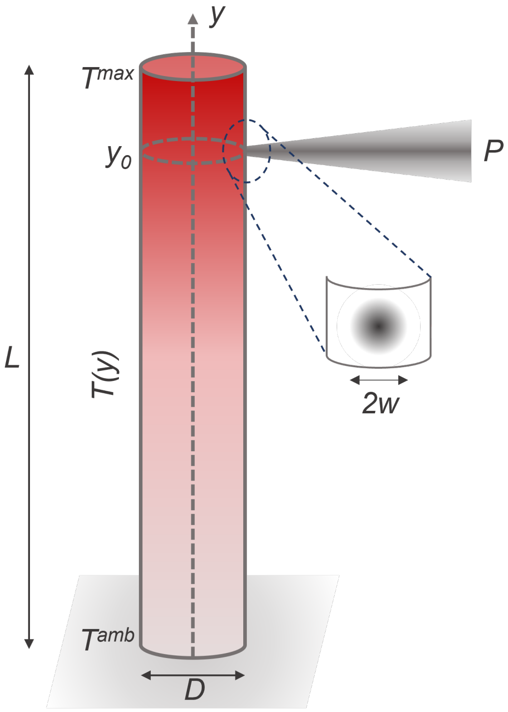

Figure 4.4: Notations for the heat equation. A nanowire of length L and diameter D is illuminated at position y_0 by an electron beam of radius w, absorbing a power P. T^{amb} is the ambient temperature, defining that of the clamping point, and $T(y)$ the local temperature.

takes the form

$$\frac{\partial}{\partial y}\left(\kappa(T(y))\frac{\partial T}{\partial y}\right)+\frac{4\epsilon\sigma_{SB}}{D}\left(T(y)^4-(T^{amb})^4\right)+\frac{4P}{\pi D^2}S(y)=0. \tag{4.1}$$

The first term of eq. (4.1) represents conduction, the second, radiation (with T^{amb} the ambient temperature) and the last, the source, with $S(y)$ normalized such that $\int_0^L S(y)dy = 1$:

$$S(y)=\sqrt{\frac{2}{\pi w^2}}e^{-2\frac{(y-y_0)^2}{w^2}}. \tag{4.2}$$

where y_0 is the position of the beam along the nanowire, see fig. 4.4 for the geometry considered. Note that P is the absorbed power at position y_0, ϵ the emissivity of the material, and σ_{SB} the Stephen-Boltzmann constant.

The objective is to numerically solve eq. (4.1) to obtain $T(y)$ for a given value of the position of the beam y_0. However, to do so we need to know the dependency of the thermal conductivity κ on temperature, which translates into a spatial dependency through the position of the beam. We used tabulated data from [144] from which we fitted a cubic extrapolation. The lack of experimental data at high temperature limits the validity of this extrapolation above $T \simeq 1100K$.

The results of the numerical computation of eq. (4.1) are displayed in fig. 4.5, for

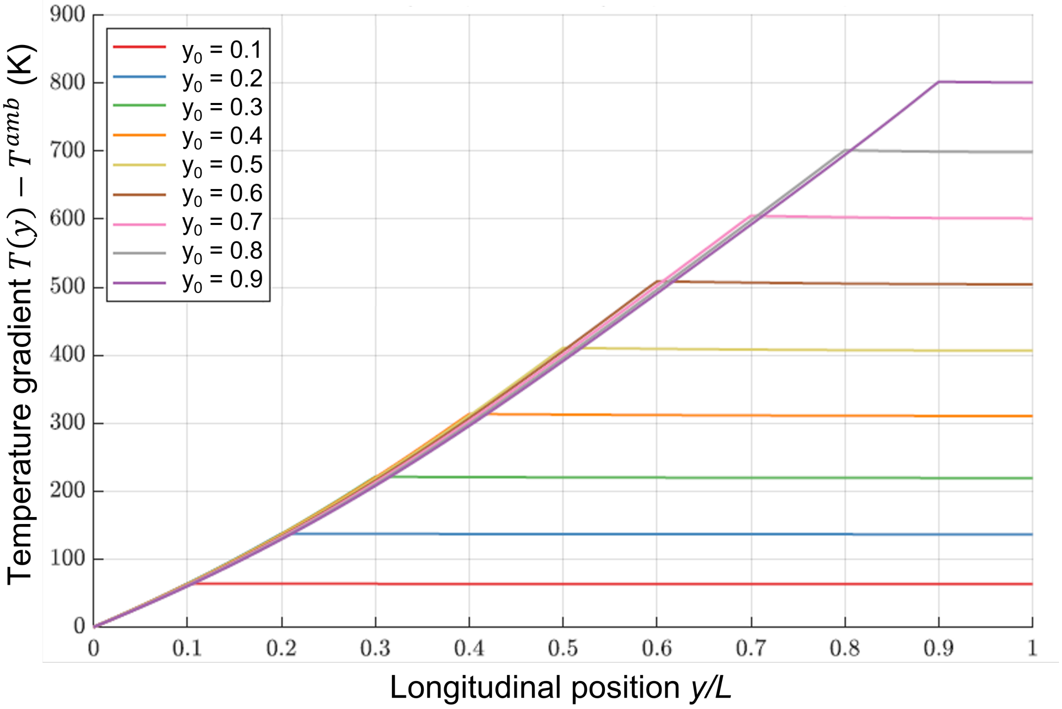

Figure 4.5: Local temperature gradient $T(y) - T^{amb}$ inside a nanowire, for different positions y_0 of the electron beam (each curve corresponds to a given value of y_0), for a 12 µm-long, 60 nm-thick InAs nanowire of WZ phase assuming an absorbed power of 0.7 µW.

the wurtzite phase of InAs (the material used in our samples), with dimensions comparable to the nanowires we measured (L = 12 µm, D = 60 nm). The power was estimated using the typical intensity and acceleration voltage of the electron beam as $P \simeq 1\mu W$. We obtain a temperature difference $\Delta T = T(y) - T^{amb}$ as high as 800 K when the SEM is applied at $y_0 = 0.9L$. This result is surprisingly high, especially when compared to the melting point of InAs (942 ℃). It demonstrates the potential of the SEM-based technique to serve as a tool for producing and studying far-from-equilibrium thermal effects in a nanomechanical system, but it also highlights the need for comprehensive studies of this effect, given that the conditions considered in this study are very standard for SEM imaging.

Figure 4.5 contains several other important pieces of information. First, since conduction can only occur between the heating point and the substrate at room temperature, the only heat flux between the heating point and the free end of the nanowire is due to radiation. However, this effect is negligible as shown by the flat curves above the heating points. Radiation will hence be ignored for rest the present study. Secondly, the evolution of the local temperature between the clamping at y = 0 and the heating point can be evaluated in first approximation by a linear slope constant for all positions of the heating point. This is equivalent to ignoring the temperature dependence of κ and setting an effective thermal conductivity. Consequently, in the rest of this thesis the local temperature is assumed to be linear and only characterized by the maximal temperature shift when the beam is located at the end of the nanowire (y = L), which we will note ΔT_{max}.

It is also interesting to note that this temperature distribution is consistent with the consequences of over-heating that were described earlier (cf section 3.3.4). Indeed, in the case of the destroyed nanowire, its tip was exposed to a high-power electron beam, which lead to to its vaporization above a certain position y_v. This point is likely to be the one at which the local temperature was equal to the melting point of InAs, and with a temperature distribution similar to that of fig. 4.5 (only with a higher maximum due to the much higher incident power), the melting temperature was exceeded for all positions $y > y_v$, leading to the destruction of the nanowire, while it remained unchanged below.

In practice, we do not have access to the local temperature profile. What we measure is the frequency shift of a given mechanical mode under the effect of heating on the Young's modulus of the material, from which we want to deduce the local temperature. However, the conversion from heating to frequency shift and vice versa is not straightforward. Indeed, as shown in section 2.5, the temperature of each mode involves its local curvature and the distribution of the losses inside the resonator, $k^i(y)$. For a crystalline homogeneous material as our InAs nanowires, these losses are of thermoelastic nature. Since the elastic properties of the InAs, depend only weakly on the temperature, we can make the simplest assumption that k^i is independent of the temperature and thus of the position y. The temperature for the n-th mechanical mode is then obtained by simplifying eq. (2.85) into

$$T_n(y_0) = \frac{\int_0^L \phi_n''(y)^2 T(y, y_0) dy}{\int_0^L \phi_n''(y)^2 dy}, \tag{4.3}$$

where $T(y, y_0)$ is the local temperature, dependent on the position of the heat source y_0. As an example, the first two mode temperatures are plotted in fig. 4.6 as a function of the position of the heating source, and compared to the average temperature of the nanowire, exhibiting a strong difference for all positions, even though T_2 remains close to the average temperature on a larger part of the nanowire.

Figure 4.6 also shows that the temperature dependence on the position of the

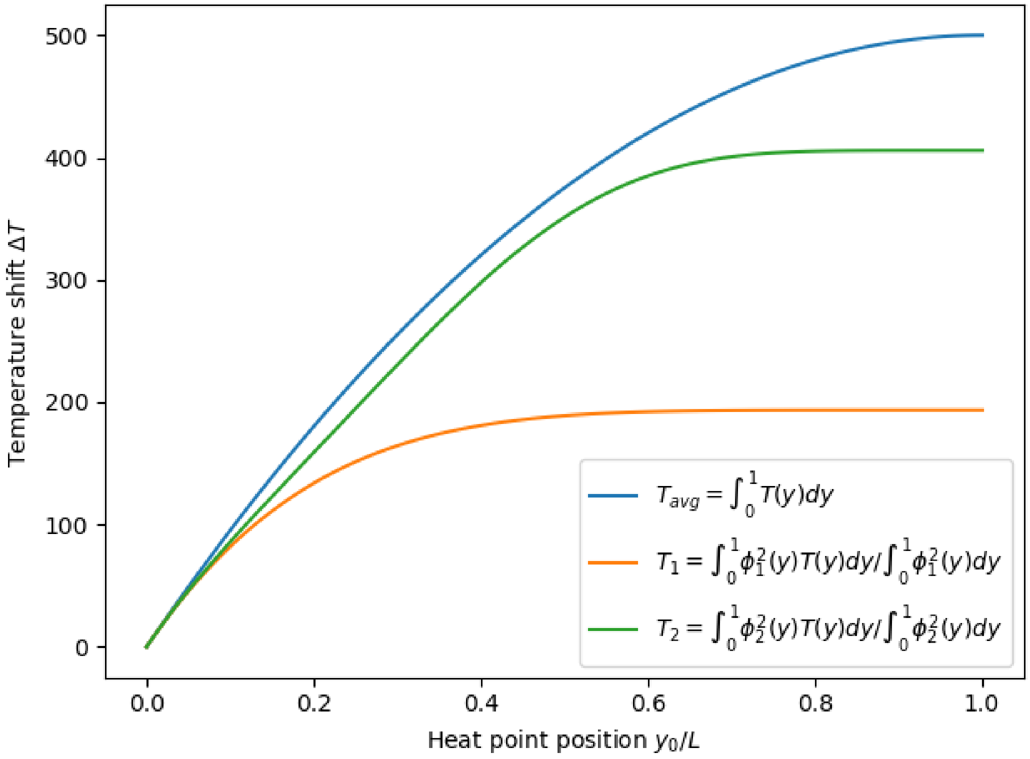

Figure 4.6: Mode temperatures for the first two flexural modes of a cantilevered beam (orange and green curves), compared to the average temperature inside the nanowire (blue curve), as a function of the position of the electron beam. The parameters of the incident beam and thermal conductivity are the same as for fig. 4.5.

heating source is basically null as it gets close to the free end of the nanowire, especially for the fundamental flexural mode. Conversely, the temperature sensitivity to the position of the source is maximal close to the clamping. This is because the mode temperature is the local temperature weighted by the curvature, which for this mode is maximal at $y = 0$ and minimal at $y = L$. The consequence of this is that in order to be sensitive to a shift of the mode temperature as the electron beam is scanned along the nanowire, one needs to have a good enough sensitivity as close to the clamping as possible, where the effective mass is maximal. The SEM, in addition to being a very efficient heating source as we have demonstrated here, presents a sufficient sensitivity to carry such measurements. As shown in section 4.1.2, the motion of the nanowire is detected as close to the clamping point as $\simeq 15-20\%$ of its length.

4.2.2 From temperature to frequency shift

Equation (4.3) gives us the temperature of a given mechanical mode, and its evolution under the displacement of a heat source along the nanowire. In order to translate this temperature shift into a frequency shift, one more step is required.

We start with the equipartition of energy, stating that the elastic energy U equals the kinetic energy K inside the resonator. For a nanowire whose displacements $u(y,t)$ are characterized by the mode shape $\phi_n(y)$ and resonant frequency Ω_n as $u(y,t) = u_0\phi_n(y)\sin(\Omega_n t)$, we can write

$$U = \left\langle \int_0^L \frac{1}{2} EI \left(\frac{\partial u}{\partial y}\right) dy \right\rangle = \frac{1}{4} u_0^2 \int_0^L EI\phi_n''(y)^2 dy \tag{4.4}$$

$$K = \left\langle \int_0^L \frac{\rho\pi R^2}{2} \left(\frac{\partial u}{\partial t}\right)^2 dy \right\rangle = \frac{1}{4} u_0^2 \Omega_n^2 \rho\pi R^2 \int_0^L \mu\phi_n(y)^2 dy, \tag{4.5}$$

where E is the material's Young modulus, $I = \pi R^4/4$ the second moment of inertia, and ρ the material density.

Equating eqs. (4.4) and (4.5) gives the following expression for the resonant frequency of mode n:

$$\Omega_n^2 = \frac{\int_0^L ER^4\phi_n''(y)^2 dy}{4\int_0^L \rho R^2\phi_n(y)^2 dy}. \tag{4.6}$$

Assuming that under the effect of heating, the Young's modulus is modified in a position-dependent way as $E = E_0(1 + \delta_E)$, the resonant frequency would then become $\Omega_n = \Omega_{n,0}(1 + \delta_{\Omega_n})$ with

$$\delta_{\Omega_n} = \frac{1}{2} \frac{\int_0^L \delta_E \phi_n''(y)^2 dy}{\int_0^L \phi_n''(y)^2 dy}. \tag{4.7}$$

Equation (4.7) can then be linked to the local temperature by assuming $\delta_E(y) = \alpha_E \Delta T(y, y_0)$, where $\alpha_E = \left(\frac{1}{E}\right)\left(\frac{\partial E}{\partial T}\right) \simeq -1.2 \times 10^{-4} K^{-1}$ for InAs is assumed independent of the temperature, and y_0 is the position of the heating source. The normalized frequency shift δ_{Ω_n} can then be expressed thanks to the variation of the Young modulus as

$$\delta_{\Omega_n} = \frac{\alpha_E}{2} \frac{\int_0^L \phi_n''(y)^2 \Delta T(y, y_0) dy}{\int_0^L \phi_n''(y)^2 dy}. \tag{4.8}$$

The result obtained here is directly proportional to the increase in mode temperature as defined in eq. (4.3). Measuring the frequency shift of a given mode thus gives a good estimation of the corresponding mode temperature.

4.2.3 Experimental results

Using the homemade software described in section 3.5.3, a scan was performed on an InAs nanowire of length 8.3 µm and diameter 67 nm. The diaphragm used on the SEM was of 20 µm, leading to a current of approximately 6 pA, and the acceleration voltage was 3 kV so that the incident power on the nanowire is approximately 18 nW, which is much lower than what was considered earlier. The spectra of vibration were recorded for each position of the electron beam, and wherever peaks were detected, a Lorentzian fit was performed in order to extract the resonant frequency.

The result of this scan is presented as a function of the beam longitudinal position in fig. 4.7a and b for the two directions of vibration of the fundamental doublet (first flexural mode of the nanowire), respectively. A fit was then performed using eq. (4.8), with two free parameters: ΔT_{max}, the maximal temperature gradient reached at the end of the nanowire and $\Omega_{i,0}$ the unperturbed frequency the i-th peak. Note that the increased scatter of data points close to the free end of the nanowire is due to the larger amplitude of displacement at these positions, making it possible to measure the resonances for more lateral positions.

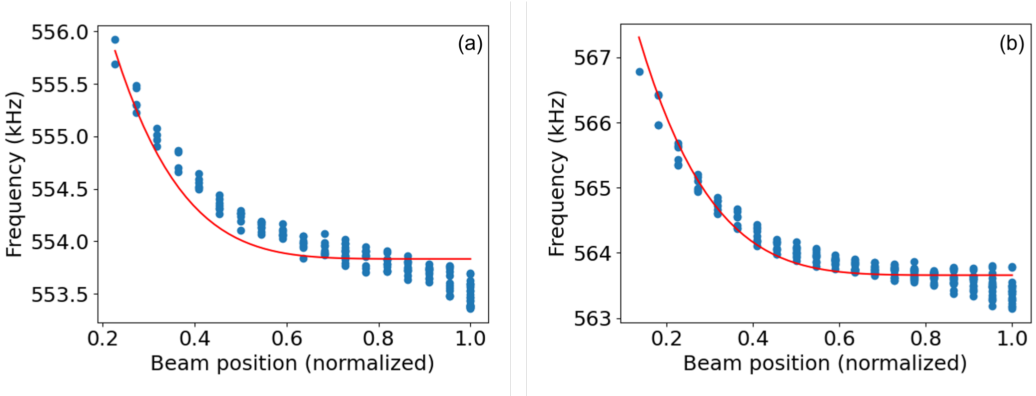

Figure 4.7: Temperature effect on the resonant frequency of an InAs nanowire during a scan, performed from the free end ($y/L = 1$) to the clamping ($y/L = 0$). The blue dots are the experimental data, the red lines are a fit according to eq. (4.8), for the two directions of vibration of the fundamental doublet (a) and (b), respectively. The fit is in good qualitative agreement, however the corresponding temperature is 1185 K, which is above the melting point of InAs and indicates that a more refined model is required.

The fit is in reasonable qualitative agreement with the data, however the numerical value obtained, $\Delta T_{max} \simeq 1185K$ is surprising given the low incident power. Indeed, the same calculation as in section 4.2.1 predict for this incident power a gradient $\simeq$ 10 K (see appendix A for details). Other acquisitions not displayed here gave a similarly satisfying fit, but with numerical values sometimes as high as 4000 K. The explanation for this variation is not clear, but it is possible that the electron beam damages the nanowire, thus varying its properties over time (see section 4.4). The value of ΔT_{max} should be compared on the one hand with the melting point of InAs (1215 K at atmospheric pressure) and the expected value calculated from the mode temperature model, i.e. $\simeq$ 10 K.

Additionally, fig. 4.7 presents features that are not picked up by the model presented so far. All these elements suggest that more phenomena take place during the measurement and that a more refined model is required. We will propose such a model in the next sections.

4.3 Signatures of dynamical back-action

When the amplitude of displacements of the resonator exceeds the size of the probe beam, as is the case for an InAs nanowire in an SEM, the heating generated by the probe will be modulated by these displacements. This will lead to dynamical effects similar to those studied in sections 2.2 and 2.6. In the present section we will see how the vibrational state of the nanowire is affected, leading to a parametric instability, and we will describe how the self-oscillating state that emerges can be characterized. We will then propose a thermo-mechanical model for dynamical back-action below the instability threshold before discussing how to minimize the effects of back-action.

4.3.1 Characterization of a parametric instability

A number of elements in our measurements strongly suggested a state of instability of the resonator, such as the blurred image presented in section 4.1. Additionally, the resonance peaks display a peculiar behaviour: even though there is no reason a priori for them to behave differently, their appearance often differed, as shown for example in fig. 4.8. Such a behaviour is typical of the presence of dynamical back-action, which translates into a modification of the response of the system through an effective damping rate defined by $\Gamma_{eff} = \Gamma_0 + \Gamma_{ba}$, with Γ_0 the unperturbed damping rate and Γ_{ba} the back-action caused modification, which can be negative. This value can be different for each mode, and if it reaches zero the corresponding mode becomes unstable.

In this case, the amplitude of movement becomes (theoretically) infinite. In practice, non-linear terms become more important in the response of the oscillator, and the displacements remain bound [114]. This translates into a spectrum of displacements which has an extremely thin and high peak, which was often observed in our first measurements (see fig. 4.8). The width of the peak then becomes smaller than the RBW of the spectrum analyser, making a Lorentzian fit impossible and suggests a state of parametric instability. However, in order to confirm that the motion of the resonator is no longer in a thermal state, we need to go beyond this spectral analysis. A possibility is to use a temporal analysis of the fluctuations, using the phase space representation which was introduced in section 2.1.5.

The extraction of the quadratures of the motion was easily available with the RSA we used. As was previously explained, in the case of thermal equilibrium, the quadratures explore an area of phase space centered around the origin, and the histograms of their trajectories have a Gaussian shape. On the contrary, if the resonator undergoes an instability, the quadratures diverge from the origin, and are only bound by the non-linear terms of the response of the oscillator (see section 2.1.5).

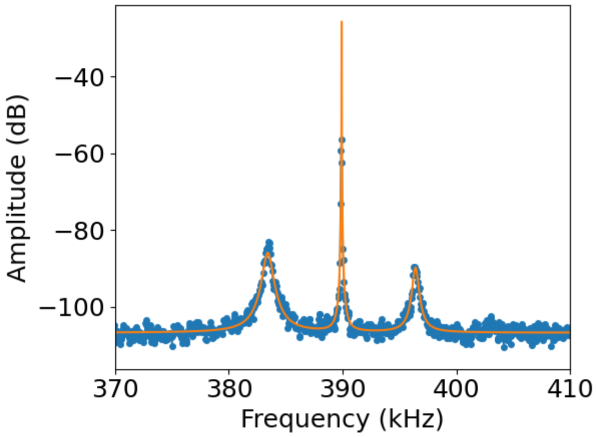

Figure 4.8: Spectrum presenting instabilities. The blue dots are the experimental data, while the orange line is the best fit possible, using a Lorentzian-shaped function for each peak. Data display a third peak, which is a sideband due to detection non-linearities, as explained in section 4.3.2. While the first mode is accurately fitted (with a quality factor $Q \simeq 600$), the second mode presents a suspicious width, smaller that the RBW of the spectrum analyser which causes the Lorentzian fit to fail, suggesting that the second mode is self-oscillating. The sideband at $\simeq 396.4$ kHz is the result of non-linearities of detection.

Figure 4.9 displays both behaviours, for a single nanowire. The behaviour depends on the position of the SEM beam along the nanowire: for two positions (noted 1 and 3 on panel (a)), the quadratures (here labeled I and Q) present a thermal equilibrium behaviour. The dispersion of the points is narrower for position 3 simply because the amplitude of displacements is smaller at this position along the nanowire when compared to position 1. On the other hand, at position 2 the behaviour of the system diverges clearly from a Gaussian. Both quadratures have an increased probability of being at extreme values, and the phase space explored is a limit circle with a Gaussian width, as expected for a resonator that has gone through an instability and started self-oscillating [106].

A self-oscillating system is characterised by an oscillation with a roughly fixed amplitude and frequency whose phase diffuses slowly over time. The result in the phase space depends on the measurement time t_{meas} compared to the phase diffusion time t_{phase}. For $t_{meas} \ll t_{phase}$, a Gaussian at a finite position is expected, similar to a driven oscillator (see section 2.1.5). On the other hand, for $t_{meas} \gg t_{phase}$, a ring with a Gaussian width is expected. The data presented in fig. 4.9 is intermediate between these two examples, as the initial Gaussian started to smear around a circle with a fixed amplitude. It shows phase diffusion having an effect but not having enough time to produce a uniform ring, as we will show more carefully in section 4.3.3. This phenomenon is standard for

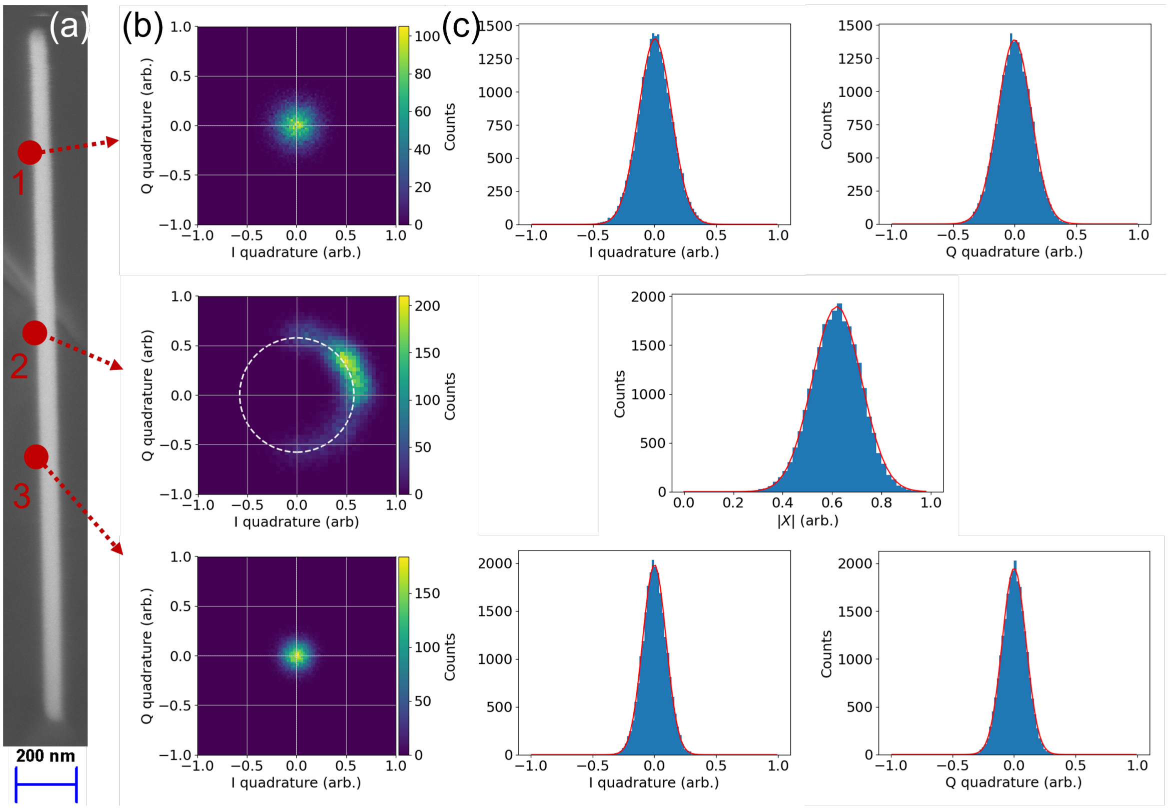

Figure 4.9: Identifying the state of a vibrational mode with quadratures. (a) Fast SEM image of the nanowire (the stage is tilted by 15° leading to smaller apparent length of the nanowire). Each dot corresponds to a position at which the IQ measurement was performed. (b) 2D histograms of the phase space. Positions 1 and 3 show the standard behaviour of a resonator at thermal equilibrium, with a Gaussian statistics centered around the origin. On the contrary, position 2 shows a clear self-oscillation behaviour, and the trajectory of the resonator in phase space explores a limit circle (highlighted in white). This suggests a parametric instability associated with dynamical back-action, which is studied in the next section. (c) Histograms of the I and Q quadratures for positions 1 and 3, and of the amplitude $|X(t)| = \sqrt{I(t)^2 + Q(t)^2}$ for position 2, i.e. the thickness of the trace along the limit circle. The red lines are Gaussian fits to the data, in excellent agreement.

self-sustained oscillations, and is known for example for lasers [145, p342] or torsional SQUID resonators [116]. In appendix B, we present another data set in which the measurement time is longer than the phase diffusion time by an order of magnitude, leading to the limit circle being fully explored.

These results allow us to conclude the presence of strong back-action effects in our measurement. It shows that the instability threshold can be reached even for relatively small incident powers (here the standard conditions were used, $P \simeq 1$ µW). However, they raise new questions, the first being that it is surprising to see these effects being localized around the middle of the nanowire, contrary to previous experiments [105] in which the dynamical back-action was inversely proportional to the effective mass of the mode, and hence maximal at the tip of the nanowire. This peculiar behaviour was observed on multiple nanowires – but not all – a fact that could be explained by the presence of previously undetected defects in the structure of the nanowire, leading to an excess of sensitivity to absorption in these positions.

In conclusion, strong back-action effects including signatures of an instability leading to self-oscillation of the nanowire are observed in this experiment. However, the domains of instability seem random, and the intensity of the phenomenon vary from one sample to another. This suggests the presence of defects in the structure of the nanowires that were previously undetected and are randomly distributed. In section 4.3.4 we will propose a model for how these defects play a role in the dynamical back-action mechanism, through thermo-elastic deformation. However, before that we will focus on the detection non-linearities that arise from the large amplitude of displacement due to one of the modes passing through an instability and undergoing self-oscillation.

4.3.2 Non-linearities of detection and sidebands

The spectrum presented in fig. 4.8 displays a peculiar behaviour that has not yet been explained in this thesis: the presence of a sideband on next to the two main peaks corresponding to the nearly-degenerate modes. As explained below, this phenomenon can be explained by the increased amplitude of displacement of the mode after it passes through the instability, which explores large areas of the probe beam, causing detection non-linearities to appear. Below we propose a simple, quantitative approach accounting for the spectral distortions associated with the non-linear transduction of a self-oscillating vibration state. Note that the calculation can be straightforwardly adapted to any vibrational state.

In this section we present a non-linear analysis of the intensity of the secondary electron beam to show that the appearance of these sidebands is due solely to detection non-linearity, and estimate the amplitude of the non-linearity directly from the spectrum presented in fig. 4.8.

So far, the intensity of the SE signal was approximated as [105]

$$I(t) = I(x_0) + \left.\frac{\partial I}{\partial x}\right|_{x_0} x(t), \tag{4.9}$$

where x_0 is the average position of the cantilever across its transverse direction in the electron beam, and $x(t)$ its planar displacement such that its position can be expressed as $x_{tot} = x_0 + x$. At this point, it is convenient to express the intensity as a Taylor series (which exists and converges, since the intensity is a bounded function defined over a compact support):

$$\begin{aligned} I(x_0 + x) = &\; I(x_0) + I'(x_0)x + \frac{I''(x_0)}{2}x^2 + ... + \frac{I^{(k)}(x_0)}{k!}x^k && (4.10) \\ = &\; \sum_{k=0}^{+\infty} \frac{I^{(k)}(x_0)}{k!}x^k, && (4.11) \end{aligned}$$

where $I^{(k)}$ denotes the k-th derivative of the intensity with respect to x.

Because the amplitude of displacement is so large, the transduction of the two non-degenerate modes are not independent anymore, and both need to be considered in eq. (4.11). We will note $x = x_1 + x_2$, with x_i the displacement associated with mode i, defining an angle θ with the electron beam as explained in section 4.1.2. We assume that the second mode has passed an instability (so that $x_2 \gg x_1$).

It is important to keep in mind that the measurement is sensitive to the displacement in one direction, which is orthogonal to the electron beam axis, but is not necessarily aligned with the direction of vibration of either of the two modes. In fact, since we see two peaks in the spectrum before any instability is reached, we know they are not aligned as discussed in section 4.1.2. In this case, x_1 and x_2 are projections of the actual displacement: $x_1 = \cos\theta \hat{x_1}$ and $x_2 = \sin\theta \hat{x_2}$. However, for the sake of simplicity of notations, we will simply use x_1 and x_2.

In this case, and using $x_2 \gg x_1$, the intensity becomes

$$\begin{aligned} I(x_0 + x_1 + x_2) = &\; \sum_{k=0}^{+\infty} \frac{I^{(k)}(x_0)}{k!}(x_1 + x_2)^k && (4.12) \\ \simeq &\; \sum_{k=0}^{+\infty} \frac{I^{(k)}(x_0)}{k!}x_2^k(1 + k\frac{x_1}{x_2}) && (4.13) \\ = &\; \sum_{k=0}^{+\infty} \frac{I^{(k)}(x_0)}{k!}x_2^k + \sum_{k=1}^{+\infty} \frac{I^{(k)}(x_0)}{(k-1)!}x_2^{k-1}x_1. && (4.14) \end{aligned}$$

We define $A(x_2) = \sum_{k=0}^{+\infty} \frac{I^{(k)}(x_0)}{k!}x_2^k$ and write $x_2(t) = r_2 \cos\Omega_2 t$ so that $A(x_2)$ contains only terms oscillating at frequencies that are multiple of Ω_2. The first term of this sum accounts for the amplitude of the peak at Ω_2.

We can expand the powers of x_2 as

$$\begin{aligned} x_2^k(t) =& \left(r_2\frac{e^{i\Omega_2 t}+e^{-i\Omega_2 t}}{2}\right)^k & (4.15)\\ =& \left(\frac{r_2}{2}\right)^k \sum_{p=0}^{k} C_k^p e^{i(2p-k)\Omega_2 t}, & (4.16)\end{aligned}$$

where $C_k^p = \frac{n!}{k!(n-k)!}$ is the binomial coefficient.

Introducing eq. (4.16) into eq. (4.14) yields

$$\begin{aligned} I(x_0+x_1+x_2) =& A(x_2) & (4.17)\\ &+\sum_{k=1}^{+\infty}\left[\frac{I^{(k)}(x_0)}{(k-1)!}x_1 \times \left(\frac{r_2}{2}\right)^{k-1} \sum_{p=0}^{k-1} C_{k-1}^p e^{i(2p-(k-1))\Omega_2 t}\right]. \end{aligned}$$

Similarly to x_2, we can write $x_1(t) = r_1\cos\Omega_1 t = (r_1/2)(e^{i\Omega_1 t}+e^{-i\Omega_1 t})$. With this notation, one can identify in the sum of eq. (4.17) terms oscillating at $(2p-k+1)\Omega_2+\Omega_1$ and $(2p-k+1)\Omega_2-\Omega_1$. However, not all of these terms need to be considered.

Indeed, only need to consider the terms oscillating at frequencies close to the natural frequencies of the system, i.e. such that $(2p-k+1)\Omega_2 \pm \Omega_1 \in \{\pm\Omega_2, \pm(2\Omega_2-\Omega_1)\}$ (the negative frequencies must be included since I is a complex signal). This translates to

$$2p-k+1 \in \{0,2,-2\}. \qquad (4.18)$$

Finally, we can isolate terms that satisfy this condition by setting $k = 2n+1$ (i.e. k is odd), and $p \in \{n\pm 1, n\}$ and eq. (4.17) becomes

$$\begin{aligned} I(x_0+x_1+x_2) =& A(x_2)\\ &+\sum_{n=0}^{+\infty}\left[\frac{I^{(2n+1)}(x_0)}{(2n)!}x_1\left(\frac{r_2}{2}\right)^{2n}\left(C_{2n}^{n-1}e^{-2i\Omega_2 t}+C_{2n}^{n}+C_{2n}^{n+1}e^{2i\Omega_2 t}\right)\right]\\ =& A(x_2)+\left\{I'(x_0)+\sum_{n=1}^{+\infty}\frac{I^{(2n+1)}(x_0)}{(2n)!}\left(\frac{r_2}{2}\right)^{2n}C_{2n}^{n}\right\}x_1\\ &+\left\{\sum_{n=0}^{+\infty}\frac{I^{(2n+1)}(x_0)}{(2n)!}\left(\frac{r_2}{2}\right)^{2n}C_{2n}^{n-1}\right\}2\cos(2\Omega_2 t)x_1, & (4.19)\end{aligned}$$

where we isolated the term $n = 0$ in the second term of eq. (4.19) in order to highlight the linear transduction of x_1.

We can then define

$$\alpha_{NL} = \sum_{n=1}^{+\infty} \frac{I^{(2n+1)}(x_0)}{(2n)!} \left(\frac{r_2}{2}\right)^{2n} C_{2n}^{n-1} \tag{4.20}$$

$$\beta_{NL} = \sum_{n=1}^{+\infty} \frac{I^{(2n+1)}(x_0)}{(2n)!} \left(\frac{r_2}{2}\right)^{2n} C_{2n}^{n}, \tag{4.21}$$

and use the quadratures $X_{1,1}$ and $X_{1,2}$ of x_1 such that $x_1(t) = X_{1,1}\cos(\Omega_1 t) + X_{1,2}\sin(\Omega_1 t)$, as well as the mode splitting $\Delta = \Omega_2 - \Omega_1$ so that the intensity becomes, when only keeping the terms at frequencies $\simeq \Omega_1,\ \Omega_2$,

$$\begin{aligned} I(x_0 + x_1 + x_2) = \ & A(x_2) + (I'(x_0) + \beta_{NL})(X_{1,1}\cos\Omega_1 t + X_{1,2}\sin\Omega_1 t) \\ & + \alpha_{NL}(X_{1,1}\cos(\Omega_2 + \Delta)t - X_{1,2}\sin(\Omega_2 + \Delta)t) \end{aligned} \tag{4.22}$$

In conclusion, the spectrum presents a sideband at $\Omega_2 + \Delta$, of amplitude α_{NL}, and another sideband of amplitude β_{NL}, superimposed with the linear transduction of the first mode at Ω_1. Considering that the spectrum is actually the Power Spectral Density of the intensity, the ratio between the two sidebands is equal to

$$S_{II}[\Omega_1]/S_{II}[\Omega_2 + \Delta] = \left(\frac{I'(x_0) + \beta_{NL}}{\alpha_{NL}}\right)^2. \tag{4.23}$$

By using an image of the nanowire, extracting $I'(x_0)$ from the intensity profile at the position of measurement and computing this ratio, one can thus deduce the amplitude of the non-linearities. This is the purpose of the next section.

Amplitude of the non-linearity

In this section we will show how an image of the nanowire and a spectrum are sufficient to evaluate the detection non-linearity intensity. To calculate α_{NL} and β_{NL} as defined in eqs. (4.20) and (4.21), we need to access the derivatives of the profile of the electron beam at the position at which the spectrum was acquired.

This profile was extracted from an image of the nanowire, taken with a sufficiently short exposure time to not trigger the instability. To remove noise, the profile was averaged over several lines around the position of interest. We then

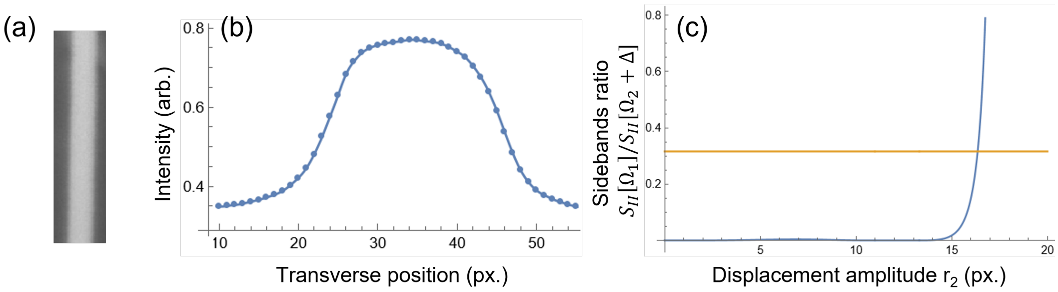

Figure 4.10: Using the intensity profile across the nanowire to calculate the amplitude of displacement. (a) SEM image from which the profile was extracted. The diameter of the nanowire is $\simeq$ 70 nm. (b) The profile extracted from the averaging of 185 lines (dots) and the polynomial interpolation of order 30 (line). (c) Ratio of the sidebands vs. the displacement amplitude r_2 (blue line). The orange line corresponds to the value measured, allowing us to identify a single valid value, $r_2 \simeq 38.5$ nm.

used a polynomial interpolation to access the spatial derivatives of the profile, as shown in fig. 4.10a.

α_{NL} and β_{NL} can then be computed as a function of the amplitude of displacement of the mode undergoing the self-sustained oscillations, r_2. This amplitude can be deduced by calculating the ratio of the sidebands as a function of r_2 using eq. (4.23) and comparing it to the experimental value obtained from fig. 4.8, as presented in fig. 4.10c. We obtain a value $r_2 \simeq 38.5$ nm.

As a comparison, the range on which the detection is linear (corresponding to the range on which the intensity profile of fig. 4.10b can be approximated as a line) is $r_{lin} \simeq 9.3$ nm. This shows that the linear approximation is no longer valid when the resonator undergoes self-oscillation as the amplitude of displacement r_2 is more that 4 times larger than the linear range r_{lin}.

4.3.3 Phase diffusion

Figure 4.9 also displays other interesting features of a mechanical mode that has started to self oscillate. In particular, we do not see a Gaussian at some finite amplitude, which is expected for a thermal state (see section 2.1.5). Instead, we observe a peak smeared out around part of a ring of constant amplitude, thus exploring a partial limit cycle, which strongly suggests that the dynamics is subject to phase diffusion. This well-known phenomenon is due to the presence of a white noise on the phase of the signal, which can be expressed with a time-varying phase: $X(t) = \tilde{X}(t) \times e^{i\phi(t)}$, where $\tilde{X}(t)$ is the coherently driven value. If the phase noise is due to a white noise such as thermal noise, then it

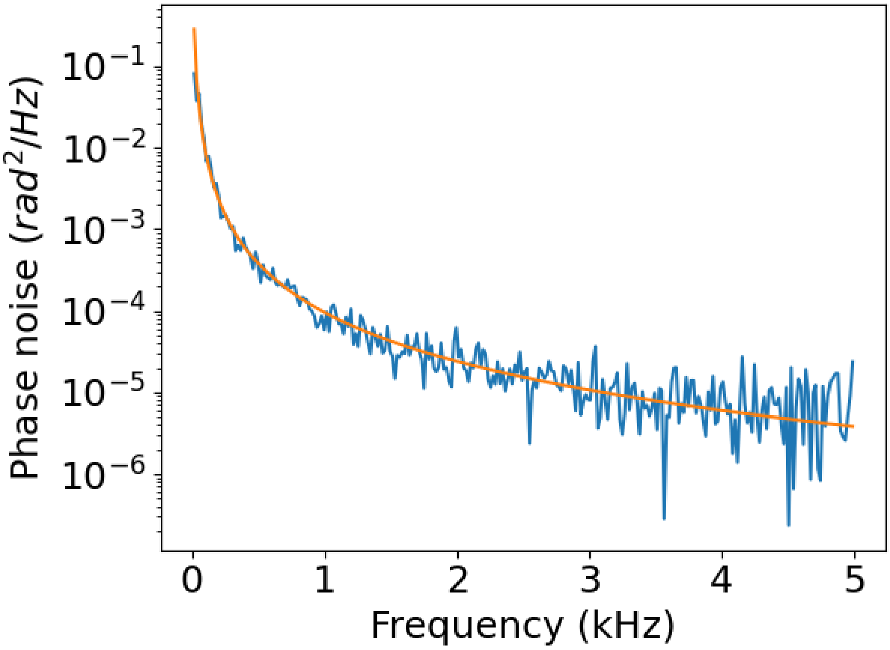

Figure 4.11: Phase diffusion in instability. The blue line is the spectrum of the phase evolution, the orange line is a $1/f^2$ fit, yielding a diffusion constant $D \simeq 48\ \mathrm{s}^{-1}$.

becomes equivalent to Einstein diffusion with constant D [146, 147].

In this case, Leeson's model for phase noise [148] can be applied, and for a large frequency $\Omega \gg D$, the noise spectrum of the phase is simply expressed as

$$S_{\phi\phi}[\Omega] = \frac{2D}{\Omega^2}. \tag{4.24}$$

The phase of the signal can be calculated from the quadratures as $\phi = \arctan(Q/I)$, from where its spectrum can be easily calculated. Figure 4.11 shows the phase noise spectrum of the data presented in fig. 4.9 (position 2) with a fit using eq. (4.24), giving a phase diffusion constant of $D \simeq 48\ \mathrm{s}^{-1}$, giving a characteristic time of evolution $t_{phase} = 1/D \simeq 21$ ms. This result is coherent with the measurement duration, which was of $t_{meas} \simeq 54$ ms and the fact that the limit circle in the phase space is not fully explored, as was discussed in section 4.3.1.

Additionally, the diffusivity of the phase noise can be used to define the state of the oscillator. Indeed, for an oscillator in thermal equilibrium it can be shown that [147]

$$D = \frac{E_{thermal}}{E_{oscillator}} \frac{\Omega_0}{Q}, \tag{4.25}$$

where the ratio between the thermal energy and the oscillator energy is equal to the ratio of the variances of the amplitudes of displacement: $E_{thermal}/E_{oscillator} = \langle x_{th}^2 \rangle / \langle x_{oscillator}^2 \rangle$, Ω_0 the resonant frequency and Q is the intrinsic quality factor of the resonator.

Using the calculations of section 4.3.2, the amplitude of displacement of the self-oscillating mode can be estimated as $\langle x_{oscillator}^2 \rangle \simeq (38.5 \text{ nm})^2$. To calculate the amplitude of thermal motion, we can use the equipartition theorem eq. (2.20) (using the effective mass, which at the position in which the measurement was taken, 57% of the length, is $\simeq 1.28$ times larger than the physical mass), yielding $\langle x_{th}^2 \rangle \simeq (1.71 \text{ nm})^2$. Finally, using the non-self-oscillating mode to estimate the quality factor, one can find $D \simeq 3.7 \text{ s}^{-1}$, which is much smaller than the value obtained from the fit in fig. 4.11.

This discrepancy shows that in these conditions the coupling is $\simeq 13$ times larger than that with the thermal bath when the nanowire is in thermodynamical equilibrium. In other words, the origin of the fluctuations measured when the nanowire is in a self-oscillating state is drastically different from thermodynamical equilibrium. It also shows that the oscillator is in a strong coupling regime, since the coupling obtained from the experimental result is 13 times larger than the intrinsic damping.

4.3.4 Back-action below the instability threshold

In this section we will present a particular data set, shown in fig. 4.12, which displays several interesting features: a clear asymmetry between behaviour observed when the SEM beam is moved from one side of the nanowire to the other and, importantly, no instabilities. As discussed in section 2.6.1, the asymmetry strongly suggests the presence of dynamical back-action, which we will now focus on.

In order to study the effects of back-action, it is convenient to study the splitting between the two nearly-degenerate mechanical modes of the resonator, as was introduced in section 2.6. The splitting $\Omega_2 - \Omega_1$ between the two peaks of the fundamental doublet is shown in the left panel of fig. 4.12, and we extended this approach by considering also the difference between the damping rates $\Gamma_2 - \Gamma_1$ (middle panel) and the ratio of the amplitudes of the peaks (right panel). All these quantities display the same asymmetry, which is characteristic of dynamical back-action.

This phenomenon could be explained, in a qualitative way, by the combined

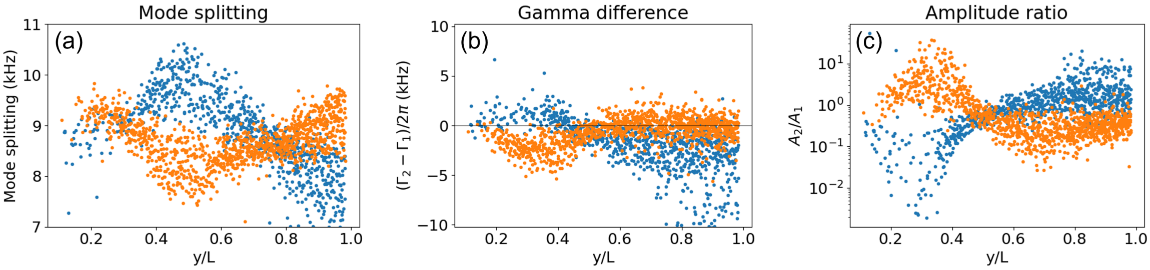

Figure 4.12: Back-action below the instability threshold. (a) Mode splitting. (b) Difference of the damping rates. (c) Ratio of peaks amplitude. Blue dots are the left side of the nanowire, orange dots the right side. All three quantities exhibit clear asymmetries which are signatures of back-action.

effects of a localised defect and thermo-mechanical back-action, as we will now explain. This model was proposed by L. Bellon from ENS Lyon.

Model for thermo-mechanical back-action

Similarly to section 4.2.1, we start with the heat equation, noting that $T(y,t)$ is the local temperature along the nanowire. However, here we directly assume that the radiation term is negligible and the thermal conductivity κ independent of temperature, and we add a dynamical term:

$$\frac{\partial}{\partial y}\left(\kappa\frac{\partial T}{\partial y}\right)=\rho C_P\frac{\partial T}{\partial t}, \tag{4.26}$$

where κ is the thermal conductivity, ρ the density and C_P the heat capacity of the material. The beam, of power P_0, being at position y_0, we can write the boundary conditions as

$$\begin{cases} T(0,t)=T^{amb} \\ \left[\kappa\frac{\partial T}{\partial y}\right]_{y_0}=\frac{aP_0}{\pi R^2} \\ \kappa\frac{\partial T}{\partial y}(L,t)=0, \end{cases} \tag{4.27}$$

where a is a parameter representing the fraction of the incident power that is absorbed by the nanowire, and T^{amb} the ambient temperature.

In the stationary case, eq. (4.26) becomes

$$\frac{\partial}{\partial y}\left(\kappa\frac{\partial T}{\partial y}\right)=0, \tag{4.28}$$

and the boundary conditions are unchanged. Equation (4.28) can be solved on $y \in [0, y_0]$ and in $y \in [y_0, L]$, giving a linear result on the former and a constant on the latter, i.e. the result derived in section 4.2.1.

In the non-stationary case, let us assume that the displacements of the nanowire's tip are defined by a function $\delta(t) = \delta_0 e^{i\Omega t}$. This will modulate the absorbed energy as

$$a(t) = \frac{da}{d\delta}\delta_0 e^{i\Omega t}, \tag{4.29}$$

hence periodically modifying the boundary conditions of the system.

We then define ΔT as $T(y,t) = T_s(y,t) + \Delta T(y,t)$ with T_s the stationary temperature. Assuming the thermal conductivity does not depend on the position, and using a separation of variables $\Delta T = \Delta T_y e^{i\Omega t}$ with ΔT_y independent from t, the heat equation can be written as

$$\frac{\partial^2 \Delta T_y}{\partial y^2} = i\Omega \frac{\rho C_P}{\kappa}\Delta T_y = \alpha^2 \Delta T_y, \tag{4.30}$$

where we defined a complex parameter α such that $\alpha^2 = i\Omega\frac{\rho C_P}{\kappa}$. Using the boundary conditions, we can then write

$$\Delta T(y,t) = \begin{cases} \Delta T_\Omega \frac{\sinh \alpha y}{\sinh \alpha y_0} e^{i\Omega t} & \text{if } y < y_0 \\ \Delta T_\Omega \frac{\cosh \alpha (y-L)}{\sinh \alpha (y_0 - L)} e^{i\Omega t} & \text{if } y > y_0, \end{cases} \tag{4.31}$$

with

$$\Delta T_\Omega = \frac{P_0}{\kappa \pi R^2} \frac{\sinh \alpha y_0 \cosh \alpha (y_0 - L)}{\alpha \cosh \alpha L} \frac{\partial a}{\partial \delta}\delta_0. \tag{4.32}$$

The total temperature then oscillates around the stationary temperature, at frequency Ω, and with an amplitude determined by ΔT_Ω. Figure 4.13 schematizes the results of this calculation. Note that the term $\frac{\partial a}{\partial \delta}$ (a being the proportion of absorbed power) changes sign when we change the side the nanowire considered, leading to the aforementioned asymmetry.

From temperature to back-action. We now have a description of the temperature inside the nanowire, taking into account its displacements and the absorption. Let us now focus on how it translates into a change of the resonant frequencies of the nanowire. To do so, let us assume that the temperature

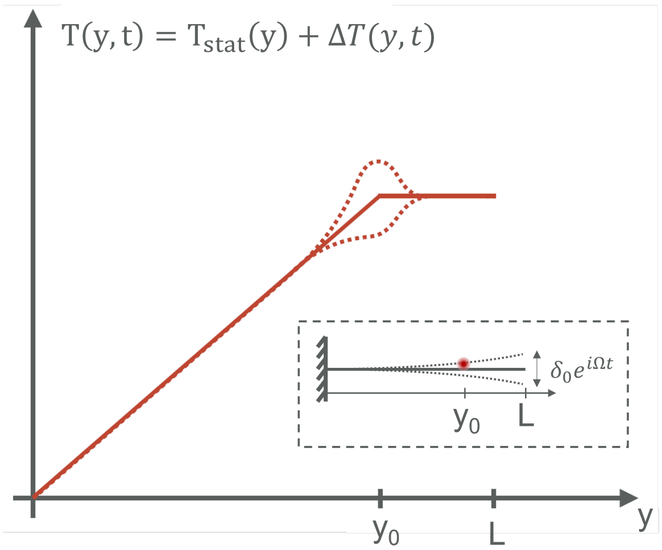

Figure 4.13: Temperature with thermal back-action. The solid line is the stationary temperature, linear by parts. The dashed lines include the non-stationary term ΔT_Ω and represent the envelope of the oscillations of the total temperature. The inset schematizes the geometry considered.

change $\Delta T(y,t)$ induces a curvature $\delta(y,t)$ such that

$$\frac{\partial^2 \delta}{\partial y^2} = \beta(y) \Delta T(y,t), \tag{4.33}$$

with some function $\beta(y)$ which remains to be determined and represents the sensitivity of the material to temperature.

For example, for a bimetal-like nanowire, e.g. a nanowire coated on one side with gold, β would be uniform. For a localized defect in the structure of the nanowire, this function would be a Dirac function $\beta(y) = \beta_D \delta(y - y_D)$ with y_D the position of the defect. As we will see, this assumption gives good results considering the experimental data presented in fig. 4.12. From now on, we will assume that β takes this form.

Introducing eq. (4.33) into Euler-Bernoulli equation gives a modified version such that

$$\frac{\partial^2}{\partial y^2}\left[EI\left(\frac{\partial^2 \delta}{\partial y^2} - \beta \Delta T\right)\right] + \rho \pi R^2 \frac{\partial^2 \delta}{dt^2} = 0. \tag{4.34}$$

Using the definition of β to cancel its spatial derivatives and using the heat equation eq. (4.30), one can then derive

$$\begin{aligned}\frac{\partial^2\delta}{\partial y^4}+\frac{\rho\pi R^2}{EI}\frac{\partial^2\delta}{\partial t^2}=&\beta\frac{\partial^2\Delta T}{\partial y^2}\\ =&\beta\frac{\rho C_P}{\kappa}\frac{\partial\Delta T}{\partial t}\\ =&\beta\alpha^2\Delta T,\end{aligned}\tag{4.35}$$

which is simply the Euler-Bernoulli equation with an external force $f_{ext}(y,t)=EI\beta(y)\alpha^2\Delta T(y,t)$. The corresponding force acting on mode n (characterized by its mode shape $\phi_n(y)$) is then F_n such that

$$\begin{aligned}F_n e^{i\Omega t}&=\int_0^L f_{ext}(y,t)\frac{\phi_n(y)}{\phi_n(L)}dy\\ &=EI\alpha^2\int_0^L\beta(y)\Delta T(y,t)\frac{\phi_n(y)}{\phi_n(L)}dy.\end{aligned}\tag{4.36}$$

Using eq. (4.31), the integral can be separated in two segments $y\in[0,y_0]$ and $y\in[y_0,L]$, y_0 being the position of the electron beam. Equation (4.36) becomes

$$F_n=EI\alpha^2\Delta T_\Omega\left[\int_0^{y_0}\beta(y)\frac{\sinh\alpha y}{\sinh\alpha y_0}\frac{\phi_n(y)}{\phi_n(L)}dy+\int_{y_0}^L\beta(y)\frac{\cosh\alpha(y-L)}{\cosh\alpha(y_0-L)}\frac{\phi_n(y)}{\phi_n(L)}dy\right].\tag{4.37}$$

Finally, using the definition of ΔT_Ω from eq. (4.32), we can write eq. (4.37) as $F_n=-k_{ba}\delta_n$ with $\delta_n=\delta_0(\phi_n(L)/\phi_n(y_0))$ the amplitude of mode n and k_{ba} the effective back-action stiffness:

$$\begin{aligned}k_{ba}=&-EI\alpha\frac{\partial a}{\partial\delta}\frac{P_0}{\kappa\pi R^2}\frac{\sinh\alpha y_0\cosh\alpha(y_0-L)}{\cosh\alpha L}\frac{\phi_n(y_0)}{\phi_n(L)}\\ &\times\left[\int_0^{y_0}\beta(y)\frac{\sinh\alpha y}{\sinh\alpha y_0}\frac{\phi_n(y)}{\phi_n(L)}dy+\int_{y_0}^L\beta(y)\frac{\cosh\alpha(y-L)}{\cosh\alpha(y_0-L)}\frac{\phi_n(y)}{\phi_n(L)}dy\right].\end{aligned}\tag{4.38}$$

β being a Dirac function, the two integrals in eq. (4.38) simplify to

$$\int_0^{y_0}\beta(y)\frac{\sinh\alpha y}{\sinh\alpha y_0}\frac{\phi_n(y)}{\phi_n(L)}dy=\begin{cases}\beta_D\frac{\sinh\alpha y_D}{\sinh\alpha y_0}\frac{\phi_n(y_D)}{\phi_n(L)} & \text{if } y_D<y_0\\ 0 & \text{otherwise}\end{cases}\tag{4.39}$$

$$\int_{y_0}^L\beta(y)\frac{\cosh\alpha(y-L)}{\cosh\alpha(y_0-L)}\frac{\phi_n(y)}{\phi_n(L)}dy=\begin{cases}\beta_D\frac{\cosh\alpha(y_D-L)}{\cosh\alpha(y_0-L)}\frac{\phi_n(y_D)}{\phi_n(L)} & \text{if } y_D>y_0\\ 0 & \text{otherwise.}\end{cases}\tag{4.40}$$

k_{ba} is a complex number, and it determines the effect of thermal back-action: the modified resonant frequency is then governed by the real part of k_{ba} as $\Omega_n = \sqrt{\frac{k+\mathbb{R}(k_{ba})}{m}}$, where k is the unperturbed stiffness and m the mass. The imaginary part of k_{ba} is responsible for the change of damping rate, when this contribution is negative and has a magnitude as large as the non-thermal damping rate we can expect an instability to arise.

Interpretation

In summary, we have a thermo-mechanical coupling: the electron beam heats the nanowire, but the heating is modulated by the displacements of the nanowire. On the other hand, the increase of temperature induces strain on the resonator, which impacts its motion, thus closing the feedback loop. Note that in this case, because the heating is dominated by the electron beam, we neglect the thermo-elastic heating induced by the deformations of the nanowire.

In order to explain the features displayed in fig. 4.12, it is necessary to understand the phase relation between the two quantities involved (temperature and nanowire position). The antisymmetry between the two edges of the nanowire can be easily understood because a displacement in a given direction will have an opposite effect on the temperature depending on which side of the nanowire the electron beam is placed on, i.e. the phase relation is inverted.

However, we also notice that the effect of the thermo-mechanical coupling changes sign as the electron beam is scanned *along* the nanowire. To explain this behaviour, we need to take a closer look at the (position dependent) coupling factor $\beta(y)$. If we make the most simple assumption that $\beta(y) = \beta_0$ is independent of the position, then the amplitude of the effect of the coupling is simply determined by the amplitude of the modulation induced by the displacement of the nanowire. Since we consider the fundamental flexural mode, the amplitude of displacement increases monotonously as the position considered gets closer to the free end, and so does the coupling. Therefore, this assumption cannot explain the measured behaviour.

Another possibility, based on the locality of the instabilities presented in section 4.3.1, is to assume that the coupling is localized, for example because of the presence of a defect in the structure of the nanowire. This can be modeled by setting $\beta(y) = \delta(y - y_D)$ with δ the Dirac function and y_D the position of the defect. In this case, when the heating occurs a position y_0 different from

y_D, the heat has to travel all the way to the position of the defect before it has an effect on the mechanics. A phase delay is thus added, determined by the thermal conductivity of the material and the distance $y_0 - y_D$ between the electron beam and the defect. This means it can get to zero, or even change sign, as the beam is scanned along the nanowire. This assumption, even though the microscopic nature of the defect is unknown at this stage, is the most realistic to explain the results that were measured – and it is consistent with the results presented in section 4.3.1.

Qualitative test of the model

The first step to test the model presented above is to check if a qualitative agreement can be reach, given that a number of quantities are not well known for nanowire. For example, while the thermal properties such as diffusivity of bulk materials are known, their values for nano-structures are not. However, tests can be done by varying the value of the diffusivity (defined as $D = \kappa/\rho C_P$ so that $\alpha^2 = i\Omega/D$).

Figure 4.14 shows a comparison between the experimental data and the calculated values of the real and imaginary parts of k_{ba} assuming a defect at $y_D/L = 0.35$, for different values of diffusivity in a range around the bulk value of approximately 0.2 $\mathrm{cm^2\,s^{-1}}$ [149]. The curves show that for diffusivity values approximately 10 times lower than the bulk (blue curves), the effect agrees qualitatively with the data: it presents the right sign inversions and maxima. The results for β uniform are also included. They show very different behaviour which provides further indirect support for the defect model. Note that finding values of diffusivity 10 times lower in nanowires than in bulk is not overly surprising, as shown in other work on molybdenum nanowires [150] or diamond nanowires [151] for example.

These results allow to conclude on several points. First of all, the assumption of a localised defect is relevant, and it the best agreement was found for a position $y_D/L = 0.35$. Consequently, the model with a uniform distribution of coupling β is abandoned for this nanowire. Moreover, the diffusivity is estimated for the following as $D = 0.01$ $\mathrm{cm^2\,s^{-1}}$, i.e. a factor 20 below the bulk value.

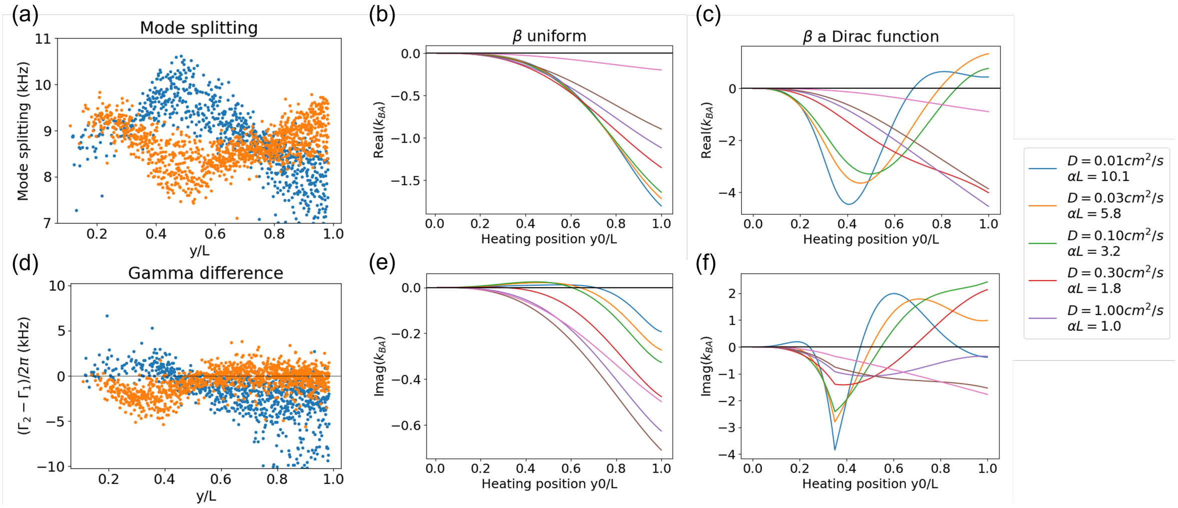

Figure 4.14: Thermal back-action. Experimental data for the mode splitting (a) and the difference in damping rates (d) are compared with (b-c) the real and (e-f) imaginary parts of k_{ba}, for different values of diffusivity and two cases for β: uniform along the nanowire or a Dirac δ function. A qualitative agreement is found with the case of a Dirac δ function, for the amplitude of the phenomenon and the inversion points, for a diffusivity approximately 10 times smaller than for bulk InAs (blue curve).

Quantitative test of the model

Having fixed the position of the defect and the value of the diffusivity, a more quantitative approach can be attempted, using eqs. (4.38) to (4.40). These equations give an additional stiffness that should be added to the natural stiffness of the fundamental mode. A development can then be made for the resonant frequency $\Omega_0 = \sqrt{\Re(k)/m}$ to extract the variation of frequency due to the thermo-mechanical back-action depending on the position of the electron beam y_0:

$$\delta\Omega_{ba}(y_0) = \frac{\Re\left[k_{ba}(y_0)\right]}{2m_{eff}(y_0)\Omega_0^2}, \tag{4.41}$$

where it is important to use the effective mass at the position of the electron beam, $m_{eff}(y_0)$. Focusing on the mode splitting allows to remove all other contributions to the evolution of the frequency other than the one in eq. (4.41). Additionally, since the qualitative agreement is better between the real part of k_{ba} and the splitting than between the imaginary part of k_{ba} and the evolution of the damping rates, it is a better candidate to evaluate the model.

However, an unknown parameter remains in the model: the strength of the coupling at the position of the defect, β_D. Allowing this value to vary, it is possible to fit the evolution of the mode splitting with a single additional

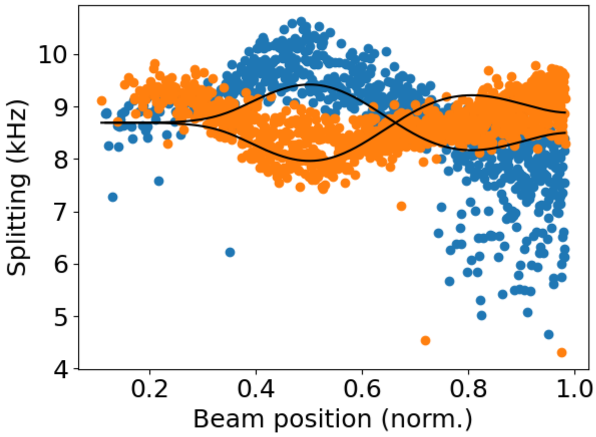

Figure 4.15: Quantitative testing of the thermo-mechanical back-action. The blue and orange dots are the experimental data for the mode splitting on the left and right side of the nanowire, respectively. Black lines are the best fit with a localised defect at $y_D/L = 0.35$, reaching a reasonable agreement.

fitting parameter being the unperturbed value of the mode splitting. The result of this fit is presented in fig. 4.15, giving a decent agreement with the model and yielding a value of $\beta_D \simeq 2.1 \times 10^7\ \text{K}^{-1}$.

This result further establishes the relevance of the model proposed, but a number of questions remain open. First of all, the absolute value of β_D returned by the fit seems high. However, to our knowledge no other experiment have measured this type of parameter before. Secondly, the shape of the measured evolution is not perfectly reproduced by the fit. This may be due to the uncertainty of the values taken for the diffusivity and y_D. Allowing these quantity to vary in the fit might lead to better result, even though it adds to the complexity of the procedure.

Furthermore, some assumptions were implicitly made to get to this result. First of all, the back-action force is assumed to have the same effect in amplitude (but with opposite sign) on the two modes of the fundamental doublet, which allowed to compare the mode splitting directly with eq. (4.41). However, this might not be the case, as this effect will depend on the direction of the resulting force relatively to the directions of vibration. More work, both theoretical and experimental, would be required to precisely identify this direction and the effect of an imbalance between the two modes.

Another possible improvement would be to take into account the transverse variation of the absorption of energy by the nanowire. This would lead to add a dependency on the transverse position x to the effective temperature and the back-action force and stiffness. That would require to refine the model, as for example the factor $da/d\delta$ present in eq. (4.38) would not only depend on the side considered, but on x.

Characterization of the structure of a nanowire

The results presented above establish that the evolution of the resonant frequency and damping rate of the fundamental mode of the nanowire can be explained with a thermo-mechanical back-action model, which includes *for this particular nanowire* a single defect located at 35% of its length.

Turning these results around, the present study can be seen as a first step towards a new interesting characterization technique for nanowires. Indeed, the imaginary part of k_{ba} presents a sharp peak at a position $y_{k^i_{ba}}$ which corresponds to the position at which the back-action effect is maximal. The signature of this effect is visible on the difference of the damping rates of the modes of the fundamental doublet. Figure 4.16(a) shows the evolution of the imaginary part of k_{ba} when the position of the defect y_D varies. as can be seen in fig. 4.16(b), the position of the minimum of $\Im[k_{ba}]$ coincides with the position of the defect, except when the defect is close to an extremity of the nanowire.

This approach is consistent with the results presented in 4.3.1, in which the behaviour of the nanowire varied drastically as the beam was moved along the nanowire. The instability zone was confined in a small portion of the nanowire, which suggests the presence of a defect at $y_D \simeq 0.57 \times L$ (position 2 in fig. 4.9). The fact that the nanowire of fig. 4.9 reached the instability threshold and not the one presented here can be explained by the fact that its defect is located further away from the clamping point, in a region where the heating is more important. This results in a stronger back-action force (as illustrated by fig. 4.16) which triggers the instability.

This model thus revealed the presence of a localized defect which was not visible on the standard SEM image nor expected given the growth technique of the nanowire. Once systematized, this could open the path to great advancements in the fabrication and characterization of nanostructures.

Second flexural mode. The expression for k_{ba} in eq. (4.38) is dependent on the mechanical mode considered. Furthermore, the second flexural mode is for a majority of positions of the heating point more sensitive to back-action than

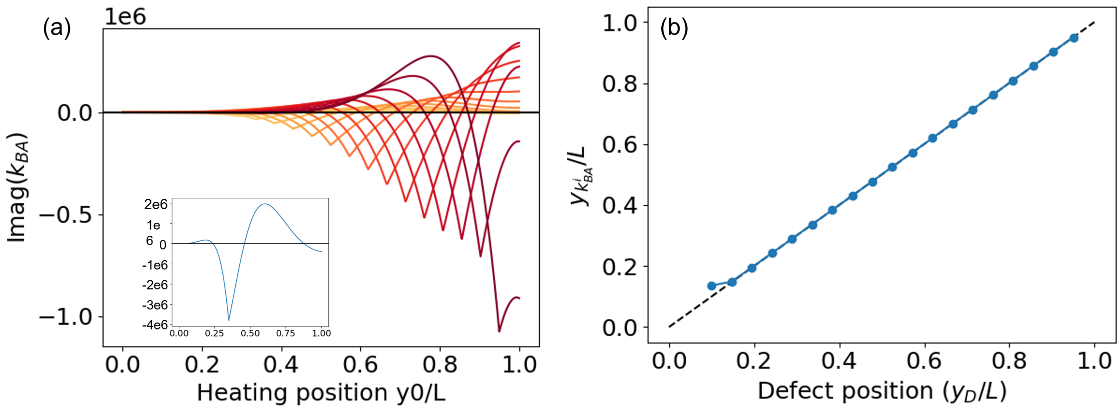

Figure 4.16: Thermal back-action dependence on the defect position. (a) $\Im[k_{ba}]$ for increasing positions of the defect, y_D. The effect of back-action is maximal at the position of the minimum of $\Im[k_{ba}]$, i.e. $y_{k^i_{ba}}$. The inset is the curve for $y_D = 0.35 \times L$, corresponding to the data experimental data presented in 4.14. (b) $y_{k^i_{ba}}$ versus the defect position y_D, showing exact correspondence on the majority of the length of the nanowire.

the fundamental mode. This is because, for a localized β function, the ratio between $k_{ba,2}$ and $k_{ba,1}$ equals

$$\frac{k_{ba,2}}{k_{ba,1}} = \frac{\phi_2(y_0)\phi_2(y_D)\phi_1(L)}{\phi_1(y_0)\phi_1(y_D)\phi_2(L)}. \tag{4.42}$$

This ratio is plotted in fig. 4.17(b), showing that indeed for application points of the SEM along almost all of the nanowire the second mode is more sensitive to back-action.

We measured the second mechanical mode on a separate nanowire, which presented very little or no effect on the fundamental mode (see 4.17(a)). Thanks to the amplification of the effect, the second mode, which was measured simultaneously, seems to display a behaviour closed to the calculated result of $k_{ba,2}$, for similar diffusivity value as previously (4.17(c) and (d)). However, technical limitations on the early versions of the experimental protocol limited the quality of the data and the number of points available. This result is however encouraging and certainly needs to be improved upon in future works.

4.3.5 Cryogenic measurements

In order to improve the effect of heating, one possibility is to increase the temperature gradient relative to the ambient temperature of the nanowire. As

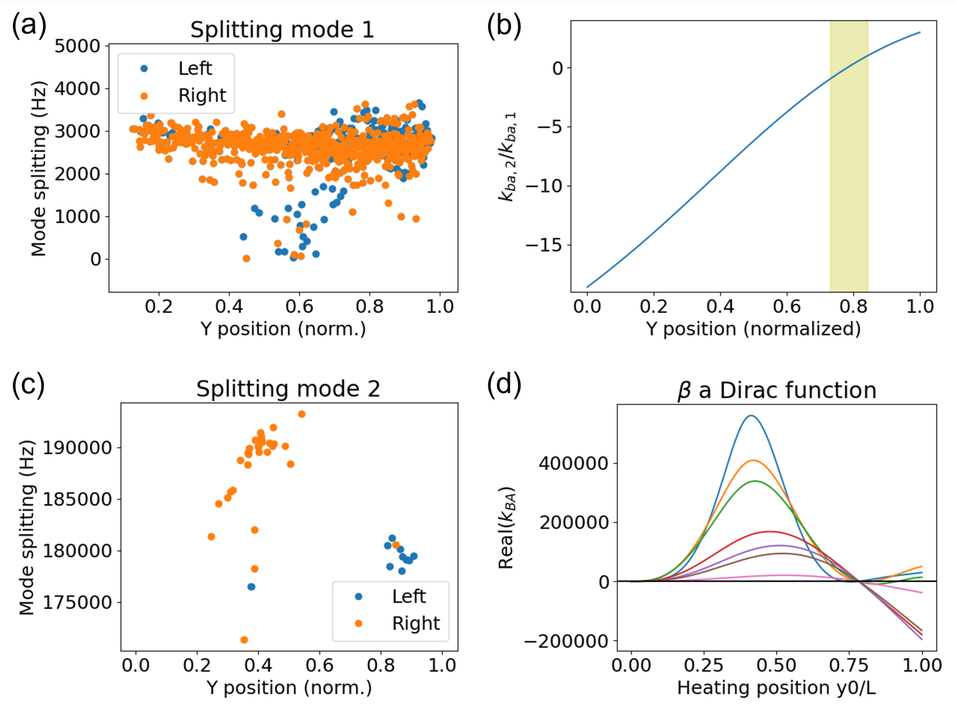

Figure 4.17: Thermal back-action for the second mechanical mode. (a) Mode splitting for the fundamental flexural mode of a cantilever, showing no clear effect. (b) Ratio $k_{ba,2}/k_{ba,1}$ of the back-action intensity for the first two flexural modes. The yellow shaded area is the zone in which the back-action is smaller for the second mode. (c) Splitting for the second mode, suggesting an enhanced effect compared with the first mode. (d) Calculated $k_{ba,2}$, for different values of diffusivity and a defect localized at $y_D = 0.35 \times L$.

explained in section 3.3.5, we had the opportunity to use an SEM capable of helium cooling, i.e. to reach 4.2 K. Under such conditions, the temperature gradient inside the nanowire would represent approximately a hundred-fold increase when compared to the ambient temperature, rather than the factor 2 or 3 that is reached when working at 300 K.

However, working in cryogenic environment has an impact on properties of the resonator. First of all, the mechanical quality factor is known to increase drastically at low temperatures [152, 153]. Additionally, the heat capacity of InAs decreases [154, 155], leading to increased thermal diffusion time. Both these effects contribute to increase the dissipative effects of the measurement back-action.

This is illustrated in fig. 4.18(a) and (b) where the result of a scan performed at 4.2 K is shown. The damping rate and the amplitude of the two peaks of the doublet of the fundamental flexural mode show two states: one with relatively high damping and low amplitude, and one with low damping and high amplitude. The latter is a clear sign of instability, which happens on large areas of the nanowire. Note that in this case, the numerical value of the damping rate extracted from a Lorentzian fit of each spectrum should not be trusted quantitatively, as the actual value might be much lower but the peak was not properly measured due to the value of the RBW.

This instability does not allow the study of dynamical back-action as in the previous section, however it is still possible to get some insight consistent with this model. Indeed, it would seem that this nanowire presents a defect similar to the one presented in section 4.3.4, but that due to the improvement of its mechanical properties the effect of the defect on dynamical back-action are felt on a much larger area and on an increased scale. In other words, because of the cryogenic environment, the nanowire is heated more (the temperature gradient is increased relatively to the environment temperature), and the quality factor is increased. This leads to a lowered threshold for instability and an increased sensitivity to dynamical back-action. The fact that instability occurs somewhere in the middle of the nanowire and not at its tip, where the effective mass is minimal is consistent with the localized defect model.

Because of the increased presence of instabilities, the cryogenic environment is not suitable for the thermodynamical studies that we want to perform in this work. Furthermore, another technical problem occurred during these measurements, as illustrated in fig. 4.18(c-g): this SEM is much more prone to global drifts, leading to uncertainty on the position of the beam with respect to the

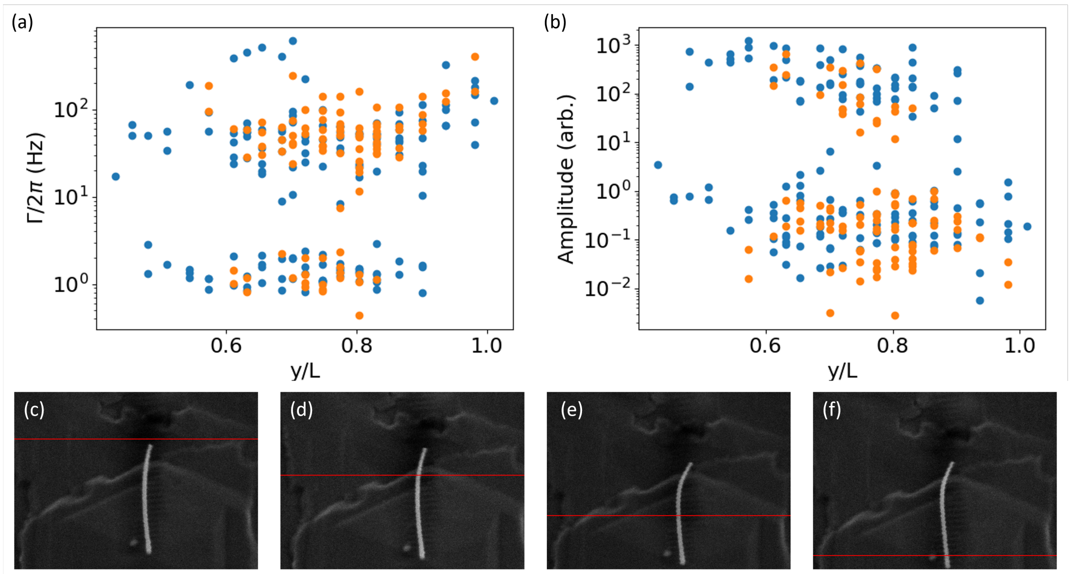

Figure 4.18: Scan of an InAs nanowire at 4.2 K. (a) Damping rate and (b) amplitude of the peaks, the fundamental flexural doublet (blue and orange dots). Both reveal the presence of instabilities on large areas of the nanowire. (c-f) Fast images acquired in the middle of the acquisition process, revealing global drifts of the sample as well as bending of the nanowire which lead to uncertainty on the position of the beam with respect to the nanowire. The red line highlights the proportion of the image that was scanned (scans acquired from the top of the image to the bottom).

nanowire. For these reasons, we decided to not push further in this direction and focus on minimizing the back-action at room temperature, as we will see in section 4.3.6.

Experimental determination of α_E. However, the cryogenic set-up could be used for other studies, and in particular for the experimental verification of a crucial material property of the nanowires: the dependency of the Young modulus on temperature, α_E. This parameter is crucial to obtain quantitative information on the heating occurring inside the nanowire during a measurement, since it makes the link between the temperature and the induced frequency shift (see eq. (4.8)).

In order to measure it, we used the lowest available power of the electron beam while keeping a sufficient sensitivity (current 17 pA and voltage 3 kV, i.e. power $\simeq 50$ nW. We then cooled our samples down to 4.2 K, and during the heating process to room temperature we measured the resonant frequency of the nanowire by performing a line scan close to its tip at successive environment temperatures.

The result is plotted in fig. 4.19a. The frequency reaches a maximum at $T \simeq 140$

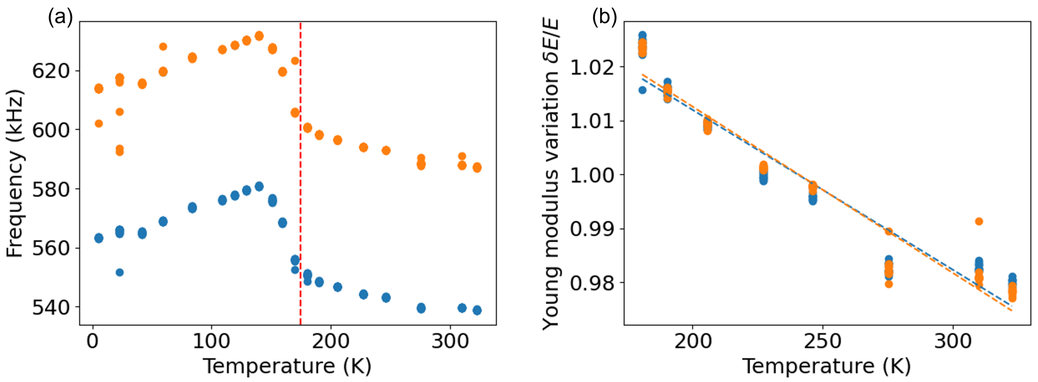

Figure 4.19: Experimental determination of α_E. (a) Resonant frequency as a function of temperature, for the two peaks of the fundamental flexural mode of an InAs nanowire. The evolution is linear above 175 K (dashed vertical line). (b) Relative variation Young's modulus calculated from the data in (a), normalized by the value at 300 K. The dashed lines are linear regressions corresponding to the first mode in blue and the second in orange, giving very similar results of $\alpha_E \simeq -3 \times 10^{-4}$.

K, before decreasing and reaching a linear regime above 175 K. We used this linear trend to extract the value of α_E when the environment temperature is close to 300 K (i.e. the experimental conditions used for all the other measurements).

In order to calculate α_E, we used the value of the resonant frequency predicted by Euler-Bernoulli beam theory (see section 2.3): $\Omega_n = \beta_n^2 \sqrt{EI/\mu}$ (I being the second moment of inertia and μ the mass per unit length), and assumed a linear dependency $E(T) = E_0(1 + \alpha_E \Delta T)$. The linear fit was performed on the relative change of the Young modulus, from the data for temperatures above 175 K, yielding $\alpha_E \simeq -3 \times 10^{-4}$, that is a factor 2.5 larger than the expected value of -1.2×10^{-4}.

However, the experimental protocol presented a number of limitations. First of all, the environment temperature was not accurately known, only the temperature of the cold finger in contact with helium and used to cool the sample, which is necessarily lower than the actual environment temperature. Additionally, as we have discussed previously, measuring the frequency at the tip of the nanowire leads to a lot of heating, meaning that this method might not be well suited for determining α_E. For these reasons, we decided for the rest of this thesis to stick to the value found in literature, i.e. $\alpha_E \simeq -1.2 \times 10^{-4}$.

4.3.6 Minimizing dynamical back-action

As we mentioned at the end of section 4.2, a number of other effects happen during the scan of a nanowire in addition to the back-action (this topic will be further discussed in section 4.4). These effects stack with the dynamical back-action discussed in section 4.3, which can even be enhanced if a defect is present in the nanowire. Simply moving away from the defects once they are detected could be a way to minimize the effects of back-action, however in order to study all the aforementioned effects in detail, it is necessary to scan the nanowire along its whole length which makes this first solution impractical. In this section we will discuss what can be done to tackle this issue.

The first way to minimize back-action has to do with the non-systematic nature of the back-action: the effects described in section 4.3 are complex and depend strongly on the nanowire under study. Indeed, as it was explained, a nanowire with a defect in its structure is expected to present strong back-action effects. On the contrary, if a nanowire does not have any defects, much weaker back action effects are expected. In fact, it could even more complex as the position of the defect inside the nanowire plays a role: if the back-action arises from the asymmetry in the structure, and if the defect is located perfectly in the centre of the nanowire, its mechanical response will not be modified [156]. This means that the choice of the sample is critical in order to select which effect to study. However, structural defects are not visible in preliminary measurements like a standard Secondary Electrons image, thus making the selection a trial and error process.

Another way of minimizing the back-action is to reduce the power received by the nanowire. That can be done by changing the SEM's acceleration voltage and current intensity in the range allowed by the manufacturer, even though the relation between these parameters and the energy absorbed by the sample is not straightforward [157]. Additionally, changing the operating conditions has multiple effects on the ability to image properly the sample. Those effects include changing the beam radius, the size of the electron–matter interaction volume and the yield of Secondary Electrons. Alternatively, one can act on the effective power received by the sample by reducing its exposure time to the beam. This was one of the main reasons for developing our homemade software ViBR (see section 3.5.3) which allowed us to control the number of measurement points on a sample as well as the dwell time of the beam at each positions, while better synchronizing the acquisition of spectra with the motion of the beam.

Overall, our approach was to minimize as much as possible the effective incident power, while still ensuring good enough coupling with the beam and heating of the sample. We selected the nanowires to be measured with this in mind, as well as choosing mechanical Q-factors such that they are in a range allowing a reasonable measurement time (which should be larger than $2\pi/\Gamma$), but not too large as it increases the sensitivity to back-action [34].

In the following section, we will present results obtained in cases where these conditions are met, and the nanowire presents no defect.

4.4 Visible structural effects

In the case where the back-action is minimized, a number of elements show that the model of mode temperature described in section 4.2 is not sufficient to explain the observed behaviour of the resonant frequencies of the nanowire during the measurement. First of all, as mentioned in section 4.2.3, the shape of the frequency curve as a function of the beam position exhibits finer features that are both reproducible and unexplained by the model. Secondly, section 4.3.5 showed that there is uncertainty about the dependence of the material's Young modulus on temperature.

However, the most important element became visible when the improvements of our software allowed us to perform the measurement in both directions: starting from the clamping point and scanning towards the free end of the nanowire showed some interesting results. Indeed, while the local and the mode temperatures should not be dependent on the scanning direction, the evolution of frequencies was drastically different, as shown in fig. 4.20.

It appears that the frequencies always increase during a scan, independently of the direction. Additionally, they do not reset between scans, which should be the case if only thermal effects were present. This suggests that some irreversible structural effects take place. Based on previous results obtained for the long exposure of a nanowire without moving the electron beam (see fig. 4.21), we suspect etching to occur. In the following sections we will propose some models to quantify this phenomenon.

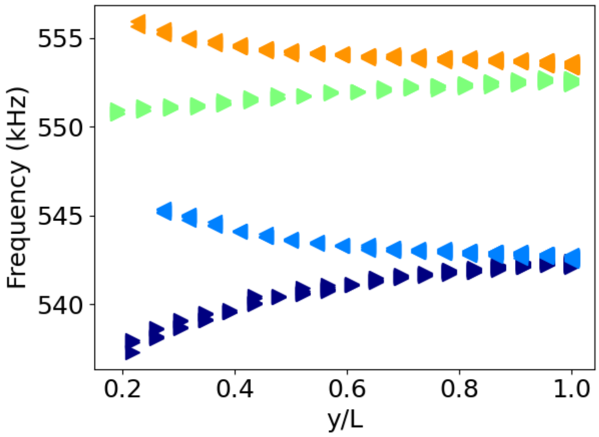

Figure 4.20: Multiple consecutive scans on a single nanowire, in both directions. Each set of points corresponds to a scan, chronologically sorted from first (dark blue) to last (orange) and in alternating directions (indicated by the direction of the arrows), for the first mode of the fundamental doublet. Frequencies always increase during the scan, and are not reset between consecutive acquisitions, which indicates an irreversible structural effect.

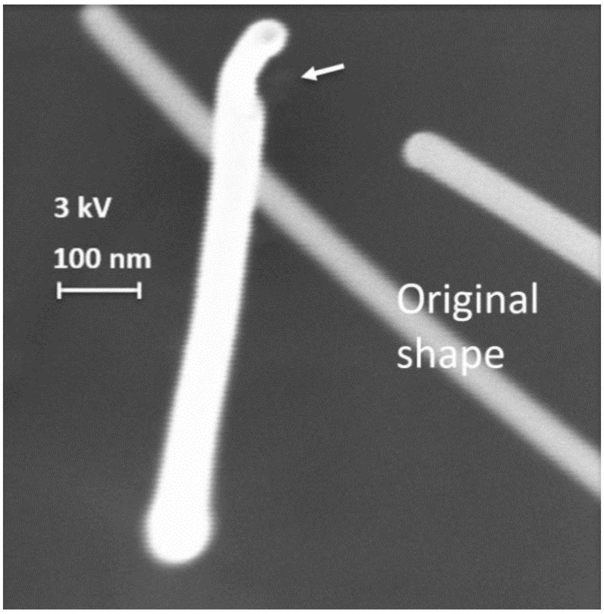

Figure 4.21: Etching of a nanowire after a long exposure time ($\simeq 45$ min). A hole is visible at the position of the electron beam (white arrow). Reproduced with permission from [158].

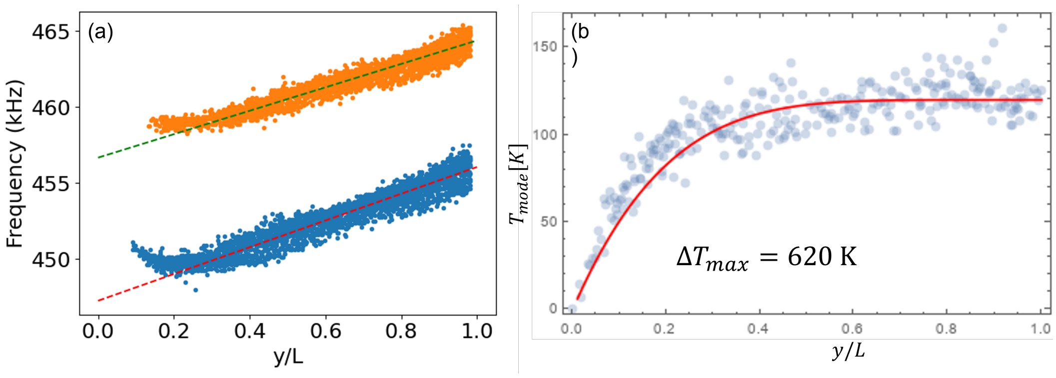

Figure 4.22: Experimental results assuming linear etching. Data acquired in the $y = 0 \longrightarrow 1$ direction, with the second generation of the software. (a) Frequency dependency on the position of the electron beam, for the two peaks of the fundamental doublet. Frequency converges to an asymptote (dashed lines) towards the free end of the nanowire. (b) Conversion of the frequency of the first mode into the mode temperature, with a fit in very good agreement with the data. In order to facilitate the fit, points were selected by keeping only a slice on each side of the nanowire.

4.4.1 First model: linear etching

A first, intuitive possibility is to assume that the effect of etching on the nanowire is linear with time. This idea was brought up when we were working with the second generation of the software (see section 3.5.2). Indeed, the measurements seemed to converge to a linear asymptote when the electron beam reached the upper half of the nanowire. In fig. 4.22a we present such a dataset, acquired by sweeping the SEM from the clamping point of the nanowire to its free end.

Then, if we subtract that asymptote from the frequencies, we should isolate the temperature contribution to their evolution. It is then possible to use the model presented in section 4.2.1 in order to fit them back into a temperature. The result of this procedure is presented in fig. 4.22b, in very good agreement with the data. Note that to get this result, the data points were selected to only include those at which the sensitivity was maximal, i.e. on a small band on each side of the nanowire. The maximal temperature difference obtained with this fit is 620 K, consistent with the predictions of section 4.2.1 (the input power matches the calculations).

However, this model relies on a very strong assumption – the linear effect of etching on the evolution of frequencies – which requires further confirmation before being adopted. Furthermore, this model did not explain the behaviour of our system in the $y = 1 \longrightarrow 0$ direction, and the measurement protocol was not completely refined, leading to uncertainties on the position of the points, and long exposure times of the nanowire. In order to improve on these aspects and to confirm or disprove this first model, the ViBR software presented in section 3.5.3 was developed. It allowed for a drastic reduction of the incident power and the measurement time, and gave us the results that were presented in section 4.2.3.

4.4.2 Refined model: localized etching

A more refined model can be inferred from the equipartition formula for the resonant frequency eq. (4.6). Indeed, it shows that there is a strong dependency of the resonant frequency on the radius of the nanowire, which is necessarily modified if etching occurs. We can then assume that it follows a similar evolution as the Young's modulus, as $R(y) = R_0(1 + \delta_R(y))$. A lowest order expansion assuming $\delta_R \ll 1$ of eq. (4.6) then yields

$$\delta_{\Omega_n} = \frac{\alpha_E}{2} \frac{\int_0^L \phi_n''(y)^2 \Delta T(y, y_0) dy}{\int_0^L \phi_n''(y)^2 dy} + \frac{\int_0^L \delta_R(y) \phi_n''(y)^2 dy}{\int_0^L \phi_n''(y)^2 dy} - \frac{\int_0^L \delta_R(y) \phi_n(y)^2 dy}{\int_0^L \phi_n(y)^2 dy}, \tag{4.43}$$

where the first term is the effect of temperature, similar to eq. (4.8), and the last two terms represent the effect of etching on elasticity and inertia, respectively.

In order to apply eq. (4.43), it is necessary to determine the function $\delta_R(y)$. To do so, we use the most simple assumptions: the etching is supposed to be local (the nanowire is etched only at the position of the electron beam), uniform (the radius is decreased by the same quantity everywhere) and continuous (the positions measured are close enough to assume we scan the whole nanowire). With this, δ_R can be expressed as a Heaviside step function, depending on the direction of measurement:

$$\delta_R(y) = \begin{cases} \delta_{R_0}(H(y - y_0) - 1) & \text{for } y_0 = 0 \longrightarrow 1 \\ -\delta_{R_0} H(y - y_0) & \text{for } y_0 = 1 \longrightarrow 0, \end{cases} \tag{4.44}$$

where δ_{R_0} is the amplitude of etching and y_0 is the position of the electron beam. The radius is thus reduced by a factor δ_{R_0} between the starting extremity of the nanowire and the electron beam, and unchanged between the electron beam and the end point of the scan.

The evolution of frequency under this effect is presented in fig. 4.23, for the first two mechanical modes of a nanowire. The results exhibits a strongly non-linear dependency on the position of the nanowire, which indicates that the "naive"

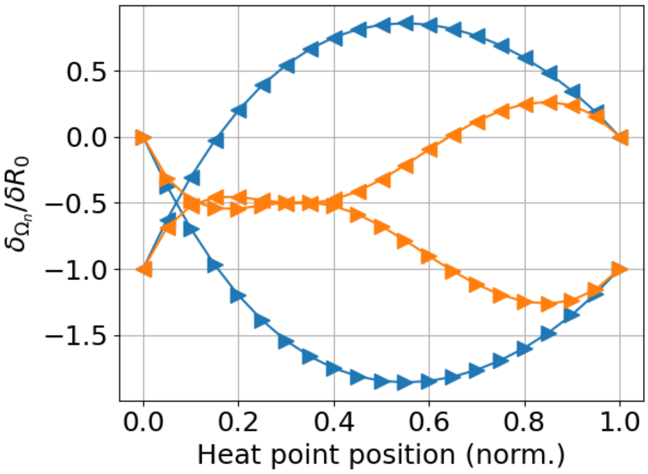

Figure 4.23: Relative variation of the resonant frequency δ_{Ω_n} of the first two flexural modes of a spherical nanowire (blue and orange triangles, respectively), under the effect of a localized, uniform, continuous etching inducing a relative change of radius δ_{R_0}. The arrows indicate the direction of the scan and the frequency shift is normalized by the etching amplitude.

approach of section 4.4.1 is not sufficient, if the assumptions made here are verified.

This model gives very good results for the $y_0 = 1 \longrightarrow 0$ direction, as shown in fig. 4.24, where a clear improvement is made on the quality of the fit compared with fig. 4.7. The free parameters of the fit are the unperturbed resonant frequencies $\Omega_{i,0}$ $(i = 1, 2)$, the amplitude of etching δ_{R_0} and the maximal temperature gradient ΔT_{max}.

While the fit follows the data points much better than the previous model, the numerical values obtained still raise some questions. Indeed, the etching amplitude would be $\delta_{R_0} \simeq 10^{-3}$, which corresponds for this nanowire to a reduction of radius of $\simeq$ 0.67 nm, which is only slightly bigger than the lattice constant if InAs (0.605 nm). Regarding temperature, the fit returns $\Delta T_{max} \simeq 1221K$, similar to what was obtained without the etching term but still surprising when compared to the melting point of InAs.

4.4.3 Limitations of the model

The model proposed in the previous section is a significant improvement over the first naive approach. However, it still presents a number of flaws. First of all, it fails to explain the behaviour of the system when the measurement is performed from the clamping to the free end of the nanowire ($y_0 = 0 \longrightarrow 1$

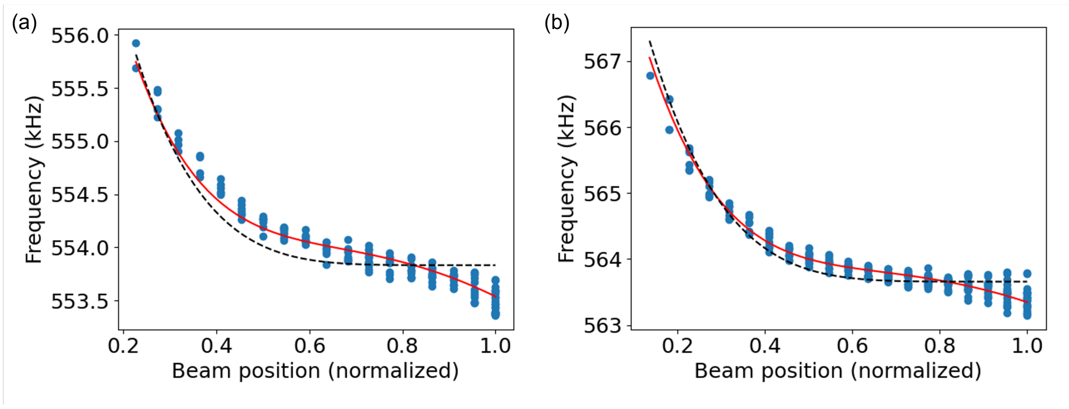

Figure 4.24: Evolution of resonant frequency of an InAs nanowire during a scan, including temperature and etching. (a) and (b) represent the two directions of vibration of the fundamental doublet, respectively. The blue dots are experimental data, the red lines a fit using eq. (4.43), in very good agreement with the data and improved from the fit with temperature only (dashed lines). The fit results give $\delta_{R_0} \simeq 10^{-3}$ and $\Delta T_{max} \simeq 1221K$. The data are the same as in fig. 4.7 and the scan was acquired in the $y_0 = 1 \longrightarrow 0$ direction.

direction). Indeed, in this case the data show a continuous increase of the frequency (see fig. 4.20) which is not predicted by this model.

Secondly, the etching model is heavily dependent on the mechanical mode considered. Using the latest development of the experimental protocol (section 3.5.4), we were able to measure the first two modes of the nanowire simultaneously. The result is presented in fig. 4.25(a) and (b) for the two directions of scan. The second mode is recognisable thanks to the node at $y/L \simeq 0.8$. Figure 4.25(c) and (d) present the corresponding evolution of the frequency as predicted by the model. While a qualitative agreement could be found in the $y_0 = 1 \longrightarrow 0$ direction, the model fails once again in the opposite direction.

4.4.4 Round-trip measurements, a solution ?

A possible solution to solve at least partially the issues in our model is to take advantage of the symmetries revealed in fig. 4.23. Indeed, the predictions for the evolution of the frequency are symmetric around a value corresponding to $\delta_{\Omega_n}/\delta_{R_0} = -0.5$. Even though the model is not completely successful in explaining the behaviour of the system, it is possible that this principle remains true.

By performing the measurement in both directions in close succession and averaging, one should then be able to remove the structural effect of etching and to

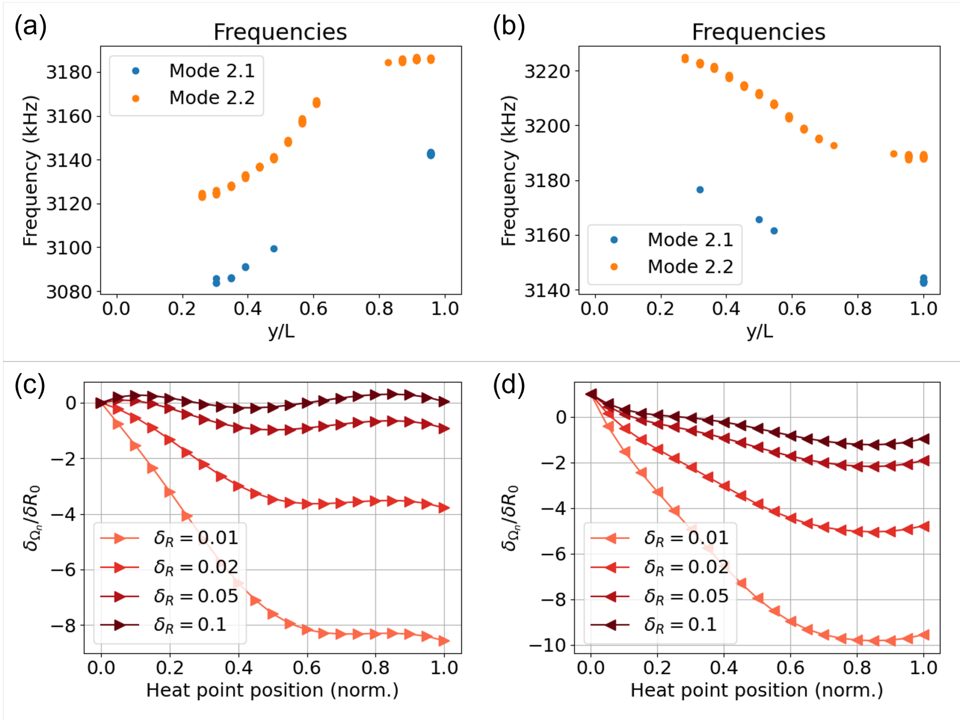

Figure 4.25: Etching model for the doublet of second flexural mode (2.1) and (2.2). (a) and (b) Measured resonant frequencies, in the $y_0 = 0 \longrightarrow 1$ and $y_0 = 1 \longrightarrow 0$ directions, respectively. (c) and (d) Predicted evolution of the resonant frequency, for a fixed maximal temperature ΔT_{max} and increasing values of δR_0.

isolate the contribution of temperature – which is independent of the scanning direction:

$$\frac{1}{2}(\delta_{\Omega}^{\leftarrow} + \delta_{\Omega}^{\rightarrow}) = \delta_{\Omega}^{(T)} + constant, \tag{4.45}$$

where the constant is the static residue due to etching. Applying this strategy yields the results presented in fig. 4.26: A fit in very good agreement with the data, and a maximal temperature of $\Delta T \simeq 528K$.

Conversely, one could choose to subtract one direction from the other in order to cancel the temperature contribution and to isolate the structural effects. The result is shown in fig. 4.27. The qualitative behaviour of this signal seems to be conserved through multiple acquisitions, and can be an indication of how the engraving affects the evolution of the resonant frequencies during the scan.

In conclusion, the electron beam of the SEM has a clear effect on the structure of the nanowire, which complicates the quantitative study of the thermal and thermodynamical state of the nanowire. Different models where proposed, but this effect proved a convoluted problem to quantify and eliminate. However, the recent developments of the experimental protocol, which include the ability to measure multiple modes simultaneously and scan the two directions along

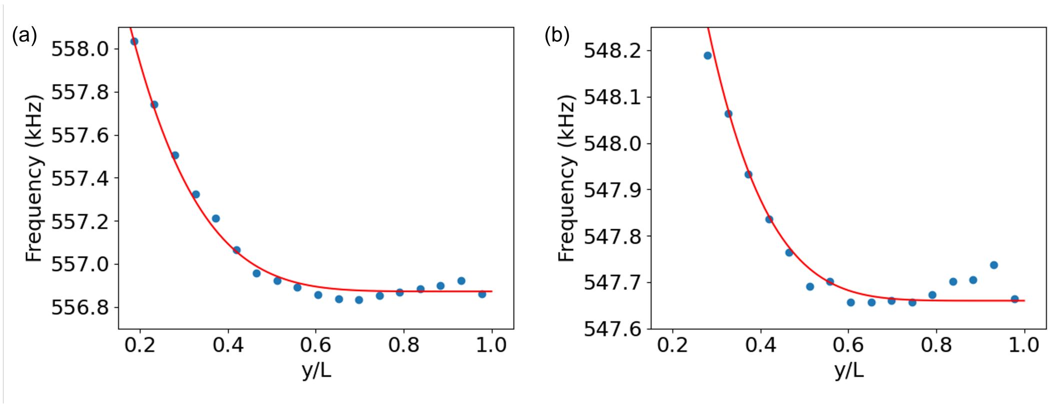

Figure 4.26: Round-trip measurement: isolation of temperature effect on the two peaks of the fundamental doublet. Blue dots are the experimental points; red lines are the fits, yielding $\Delta T_{max} \simeq 528K$.

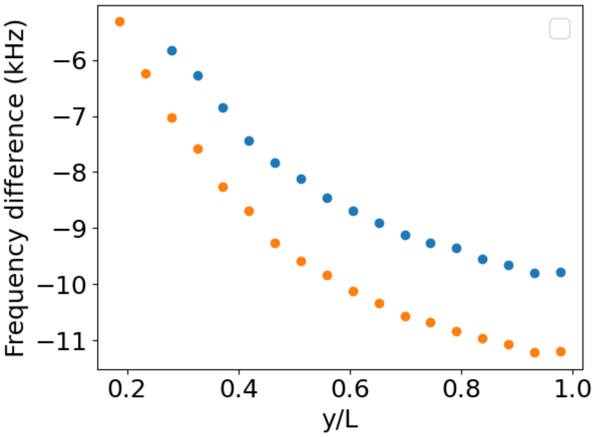

Figure 4.27: Round-trip measurement: difference between the two directions of scan, for the first and second mode of the doublet (blue and orange dots, respectively).

the nanowire back to back are promising and will help tackling this issue in the future.

4.4.5 Possible etching mechanisms

The model presented so far considers the etching simply as a diameter reduction during the acquisition, without focusing on the actual mechanism involved. In fact it can even be surprising that such phenomenon would occur in a SEM, as most radiation damages are known to require a higher beam energy and have been mostly studied TEM imaging [159, 160]. However, studies found that even at the relatively low energies involved in a SEM, some damage do occur to the sample [161, 162]. In the following paragraphs, we will list some effects that could cause the etching described in this section.

The first mechanism worth considering is the displacement effect and its consequence when it occurs in cascade, known as the knock-on effect. It is due to the elastic collisions between the incident electrons and the atomic nuclei of the object, which move the atoms into interstitial positions, which degrades the crystalline purity of the sample. The collisions which generate back-scattered electrons and involve a high amount of momentum exchange have the most impact for this effect. It was observed with low energy electrons for example within metallic samples [163]. If the displacement involves atoms close to the surface, they can be ejected from the sample, which is known as sputtering and can lead to a loss of material.

Another effect is known as radiolysis. It involves inelastic collisions which can ionize the atoms of the crystal. The surplus of energy can then be converted into kinetic energy through multiple mechanisms. For example, in alkali halides, the creation of an exciton state can lead to anion vacancies which can aggregate and create dislocation loops which will eventually diffuse to the surface [159]. Note that this effect can be temperature dependent [164] and increases as the sample is heated, which could make it a suitable candidate in our case.

An inelastic collision can also alter the chemical bounds between atoms, which in turn can lead to structural damage, mass loss, reduction in crystallinity, or contamination [137]. However, this effect is mostly known to occur in organic samples, which would rule it out for InAs nanowires.

Note that a mass loss is not the only possible result of ionization. Indeed, it may also lead to hydrocarbon contamination, when molecules are polymerized at the surface of the sample by the incoming (or outgoing) electrons. This is a well-known effect in SEM imaging and would result in a gain of mass for the resonator. This effect could be treated with the model presented in section 4.4.2 by setting a negative δ_R, which is equivalent to considering the opposite direction of measurement.

Finally, even though etching appeared as the most likely explanation of the evolution of frequency that was measured, it might not be the only structural effect taking place in the SEM. On top of the possible gain of mass mentioned above, the presence of an oxide or hydrocarbon layer on the nanowire would also change its mechanical properties such as its Young's modulus. Additionally, if the displacements of the nanowire are too important, for example because of an instability, work hardening – i.e. irreversible change of mechanical properties due to bending – could occur [111, 165].

All these effects might have an impact on the dynamics of the nanowire as it is measured and as they possibly occur concomitantly. Identifying which one – or which ones – are actually relevant would require further studies, and possibly an atomic scale model for the electron-matter interaction in these particular conditions.

Chapter 5

Conclusions and perspectives

This thesis presented a study of the thermodynamical effects affecting an InAs nanowire when measured in a Scanning Electron Microscope. We began by discussing theoretically the mechanical properties of a nanowire, its resonances and its thermal noise spectrum. We then explained the experimental setup that we used to measure this spectrum, based on the coupling between a focused electron beam and the nanowire. The very small size of the beam ($\simeq 1$ nm) allows for particularly high displacement sensitivity when compared with standard optomechanical systems, which let us resolve all the dimensions of the resonator at scales well below the optical diffraction limit.

We found a clear dependency of the resonant frequencies on the position of the electron beam. This can in part be explained by the heating of the nanowire due to the dissipative nature of the electron-matter interaction. Similar to what was previously observed on a larger scale [71, 72, 109], the effect of heating on a given mechanical mode is a function of the distribution of the losses inside the nanowire. In the simplest case where the losses are assumed to be thermoelastic, they are characterized by the local curvature of each mode, which plays a key role in defining the mode temperature, that is the temperature effectively "perceived" by the mode and is different from both the local temperature at a particular point along the wire or the average temperature in the nanowire. This leads to a theoretical model which enables measurements of shifts in the wire's frequency to be connected to changes in both the mode temperature and the local temperature.

By scanning the length of the nanowire with a heating source and recording its resonant frequencies, one should therefore be able to reconstruct its local temperature. We developed a platform that allows us to do this with a very high degree of spatial resolution, using a commercial SEM and a Real-time Spectrum Analyser, and we created a software interface controlling them both. Several versions were developed, with the interfacing being first made via a python script, before custom LabView software was created in Grenoble. The technical issues encountered, as well as the features of the final version are discussed in chapter 3. The development of this software is continued in Grenoble, and could lead to a new accurate way of characterizing the structure of nano-objects and opens the possibility to serialize this measurement on batches of samples.

The experimental measurements of the frequency led to values for the temperature that are too high to be physically plausible. This suggests that the model of mode temperature based on thermo-elastic effects could not fully explain the behaviour of the resonator (section 4.2). Indeed, the electron-matter interaction generates strong back-action mechanisms which go well beyond heating of the nanowire. These effects can, in some cases, lead to parametric instability of the nanowire, which results in huge amplitudes of displacements visible on the secondary electrons image of the resonator. In section 4.3 we discussed the signatures of back-action and characterized the state of a mechanical mode that has passed through an instability and displays self-sustained oscillations, by studying the phase space of its displacement and characterizing its phase noise. We also found that the occurrence of self-sustained oscillations depended very strongly on the precise position of the SEM beam, suggesting that localised defects within the nanowire may be playing a role.

The response of the measurement was characterized when the resonator undergoes self-sustained oscillations. The large displacement amplitudes require the inclusion of non-linear terms in the transduction of the motion into the Secondary Electrons (SE) current. It was shown that these terms give rise to sidebands around the nearly-degenerate fundamental modes, spaced by the splitting between these modes. These sidebands can then be used to calculate the amplitude of displacement. This result can be extended to any system in which the amplitude of displacement surpasses the linear response range of the detection.

We then discussed how thermal back-action can affect a nanowire when the incident power is below the instability threshold, and proposed a model explaining it for the case of a localized defect in the structure of the nanowire, which fitted the pattern of observations quite well. These results have great interest for the characterization of the structural properties of nano-objects as they provide a way to reveal features that were invisible until now when using only the SE image. Additionally, being able to control or minimize the back-action effects could help the microscopy community to develop new tools in order to improve the images of movable objects, for example by reducing thermal vibrations.

In order to focus on the thermal effect of the measurement, we tried to minimize the back-action effects. This lead to restrictions on the type of nanowire that could be used: defects have to be avoided, and a very high quality factor enhances the back-action more than it increases the sensitivity of the measurement. However, once the proper sample is selected, another effect inherent to the electron beam measurement remains: the etching of the nanowire. This problem proved highly complex as the dimensions and mechanical properties of the resonator were modified as it was measured. A model was proposed and experimentally tested in section 4.4, then refined by including assumptions on the locality and uniformity of the etching. It was found that whilst this model had some explanatory power, it was not able to fully describe the results.

This work is at the interface of multiple domains of physics and could lead to improvements in several fields. First of all, as mentioned before the microscopy community will be interested in the ability to properly image vibrating objects, if the back-action processes are understood and controlled. Then, from the material point of view, the present work proposes new ways of characterizing nano-objects, to control their structure and to measure the thermal properties of materials, which are in most cases still unknown at nanometric scale. Finally, on a more fundamental side, thermal effects are one of the main limitations in the quantum experiments with ultra-high sensitivity. Understanding the thermodynamics involved is then critical for these experiment to exceed their current limitations and achieve even better force and displacement sensitivity. Although taking place in a very different temperature range, our results may contribute to this.

5.1 Possible future works

A number of questions remain open, and improvements can be made to both the models and the experimental protocols. From the theoretical point of view, a number of assumptions were made concerning the mode temperature. The thermo-elastic damping of the nanowire was assumed to be constant, which is true in first approximation, but recent works have begun to include a dependence on temperature [73], and could be adapted for the nanowire system. Additionally, including the presence of defects that were detected into a position-dependent thermo-elastic damping could lead to more accurate predictions of the mode temperature. This, along with refinements on the model created to describe the thermo-mechanical back-action could lead to a better understanding of the fundamental effects of the electro-mechanical motion detection method in the SEM. These refinements could include taking into account the transverse coordinate dependence of the thermo-mechanical coupling in the fit of the experimental data.

The etching model also requires some improvements, which could include taking into account the thermal expansion of the nanowire, and challenging the assumption of local and uniform etching. Finalizing the inclusion of the measurement of higher order modes, possibly going further than the second flexural mode, would provide valuable data for this purpose. Additionally, identifying the actual mechanism responsible for this etching, even though it was out of the scope of the present work, could lead to valuable research in the future.

The experimental protocols could be upgraded to enable extensive characterization of the mechanical and structural properties of multiple nanowires in a single acquisition. Because of the etching that was detected, this would require optimizing the exposure time of each nanowire and possibly reducing further the input power in order to minimize this effect. It would also involve improving the software controlling the acquisition.

In conclusion, this work provided new insights into the interaction between the electron beam and a nanomechanical resonator embedded in a SEM. Dynamical back-action is better understood and significant progress has been made towards the mapping of the internal temperature of a nanowire resonator. However, additional effects occur beyond those included so far in the models, which are not yet fully understood and this calls for more theoretical work.

Bibliography

[1] N. Ghaemi, A. Nikoobin, and M. R. Ashory, "A Comprehensive Categorization of Micro/Nanomechanical Resonators and Their Practical Applications from an Engineering Perspective: A Review," *Advanced Electronic Materials*, vol. 8, no. 11, p. 2 200 229, 2022 (cit. on p. 1).

[2] A. Bachtold, J. Moser, and M. Dykman, "Mesoscopic physics of nanomechanical systems," *Rev. Mod. Phys.*, vol. 94, no. 4, p. 045 005, 2022 (cit. on pp. 1, 7).

[3] S. Barzanjeh *et al.*, "Optomechanics for quantum technologies," *Nat. Phys.*, vol. 18, no. 1, pp. 15–24, 2022 (cit. on p. 1).

[4] M. Poot and H. S. van der Zant, "Mechanical systems in the quantum regime," *Physics Reports*, vol. 511, no. 5, pp. 273–335, 2012 (cit. on pp. 1, 7).

[5] M. Carlesso *et al.*, "Present status and future challenges of non-interferometric tests of collapse models," *Nat. Phys.*, vol. 18, no. 3, pp. 243–250, 2022 (cit. on p. 1).

[6] A. A. Clerk *et al.*, "Introduction to quantum noise, measurement, and amplification," *Rev. Mod. Phys.*, vol. 82, no. 2, pp. 1155–1208, 2010 (cit. on pp. 1, 6).

[7] M. Aspelmeyer, T. J. Kippenberg, and F. Marquardt, "Cavity optomechanics," *Rev. Mod. Phys.*, vol. 86, no. 4, pp. 1391–1452, 2014 (cit. on pp. 1, 6, 29, 32).

[8] J. Müller *et al.*, "Lunar Laser Ranging: A tool for general relativity, lunar geophysics and Earth science," *J Geod*, vol. 93, no. 11, pp. 2195–2210, 2019 (cit. on p. 2).

[9] I. Newton, *PhilosophiæNaturalis Principia Mathematica*. London, 1687 (cit. on p. 2).

[10] P. Gassendi, *Syntagma Philosophicum*. Turnhour, 1657 (cit. on p. 2).

[11] C. Huygens, *Traité de la Lumière*. Leiden, 1690 (cit. on p. 2).

[12] T. Young, "The Bakerian lecture. On the theory of light and colours," *Philosophical transactions of the Royal Society of London*, no. 92, pp. 12–48, 1802 (cit. on p. 2).

[13] A. Fresnel, *Oeuvres Complètes d'Augustin Fresnel*. Paris, 1868 (cit. on p. 2).

[14] W. Geiner, *Quantum Mechanics: an Introduction*, Springer. 2001 (cit. on p. 2).

[15] A. Einstein, "Approximative integration of the field equations of gravitation," *Sitzungsber. Preuss. Akad. Wiss. Berlin (Math. Phys.)*, vol. 1916, no. 688-696, p. 1, 1916 (cit. on p. 2).

[16] A. Einstein, "Über gravitationswellen," *Sitzungsber. Preuss. Akad. Wiss. Berlin (Math. Phys.)*, vol. 1918, no. 154, p. 1, 1918 (cit. on p. 2).

[17] V. B. Braginsky, F. Y. Khalili, and K. S. Thorne, *Quantum measurement*. Cambridge, 1992 (cit. on p. 2).

[18] B. Abbott *et al.*, "Observation of Gravitational Waves from a Binary Black Hole Merger," *Phys. Rev. Lett.*, vol. 116, no. 6, p. 061 102, 2016 (cit. on p. 2).

[19] A. A. Michelson and E. W. Morley, "On the relative motion of the earth and of the luminiferous ether," *Sidereal Messenger, vol. 6, pp. 306-310*, vol. 6, pp. 306–310, 1887 (cit. on p. 3).

[20] C. Fabry and A. Pérot, "Theorie et applications d' une nouvelle methods de spectroscopie intereferentielle," *Ann. Chim. Ser. 7*, vol. 16, pp. 115–144, 1899 (cit. on p. 4).

[21] G. Grynberg, C. Fabre, and A. Aspect, *Introduction aux lasers et à l'optique quantique*. 1997 (cit. on p. 4).

[22] N. Ismail *et al.*, "Fabry-Pérot resonator: Spectral line shapes, generic and related Airy distributions, linewidths, finesses, and performance at low or frequency-dependent reflectivity," *Opt. Express, OE*, vol. 24, no. 15, pp. 16 366–16 389, 2016 (cit. on p. 4).

[23] T. Briant, "Caractérisation du couplage optomécanique entre la lumière et un miroir : bruit thermique et effets quantiques," Theses, Université Pierre et Marie Curie - Paris VI, 2003 (cit. on pp. 5, 26).

[24] A. Dorsel *et al.*, "Optical bistability and mirror confinement induced by radiation pressure," *Phys. Rev. Lett.*, vol. 51, pp. 1550–1553, 17 1983 (cit. on p. 5).

[25] B. S. Sheard *et al.*, "Observation and characterization of an optical spring," *Phys. Rev. A*, vol. 69, p. 051 801, 5 2004 (cit. on p. 6).

[26] T. Corbitt *et al.*, "An all-optical trap for a gram-scale mirror," *Phys. Rev. Lett.*, vol. 98, p. 150 802, 15 2007 (cit. on p. 6).

[27] P. F. Cohadon, A. Heidmann, and M. Pinard, "Cooling of a mirror by radiation pressure," *Phys. Rev. Lett.*, vol. 83, pp. 3174–3177, 16 1999 (cit. on p. 6).

[28] T. Corbitt *et al.*, "Optical dilution and feedback cooling of a gram-scale oscillator to 6.9 mk," *Phys. Rev. Lett.*, vol. 99, p. 160 801, 16 2007 (cit. on p. 6).

[29] C. M. Mow-Lowry *et al.*, "Cooling of a gram-scale cantilever flexure to 70 mk with a servo-modified optical spring," *Phys. Rev. Lett.*, vol. 100, p. 010 801, 1 2008 (cit. on p. 6).

[30] V. B. Braginsky and A. B. Manukin, *Measurement of weak forces in physics experiments*, Chicago, University of Chicago Press, 1977. 161 p. Translation. 1977 (cit. on pp. 6, 29).

[31] C. M. Caves, "Quantum-Mechanical Radiation-Pressure Fluctuations in an Interferometer," *Phys. Rev. Lett.*, vol. 45, no. 2, pp. 75–79, 1980 (cit. on p. 6).

[32] C. M. Caves, "Quantum-mechanical noise in an interferometer," *Phys. Rev. D*, vol. 23, no. 8, pp. 1693–1708, 1981 (cit. on p. 6).

[33] C. H. Metzger and K. Karrai, "Cavity cooling of a microlever," *Nature*, vol. 432, no. 7020, pp. 1002–1005, 2004 (cit. on pp. 6–7).

[34] O. Arcizet *et al.*, "Radiation-pressure cooling and optomechanical instability of a micromirror," *Nature*, vol. 444, no. 7115, pp. 71–74, 2006 (cit. on pp. 6, 56, 120).

[35] T. J. Kippenberg and K. J. Vahala, "Cavity Optomechanics: Back-Action at the Mesoscale," *Science*, 2008 (cit. on p. 7).

[36] C. B. Møller *et al.*, "Quantum back-action-evading measurement of motion in a negative mass reference frame," *Nature*, vol. 547, no. 7662, pp. 191–195, 2017 (cit. on pp. 7–8).

[37] U. B. Hoff *et al.*, "Quantum-enhanced micromechanical displacement sensitivity," *Opt. Lett., OL*, vol. 38, no. 9, pp. 1413–1415, 2013 (cit. on p. 7).

[38] M. T Jaekel and S Reynaud, "Quantum Limits in Interferometric Measurements," *Europhys. Lett.*, vol. 13, no. 4, pp. 301–306, 1990 (cit. on p. 7).

[39] S. Gigan *et al.*, "Self-cooling of a micromirror by radiation pressure," *Nature*, vol. 444, no. 7115, pp. 67–70, 2006 (cit. on p. 7).

[40] A. H. Safavi-Naeini *et al.*, "Laser noise in cavity-optomechanical cooling and thermometry," *New J. Phys.*, vol. 15, no. 3, p. 035 007, 2013 (cit. on p. 7).

[41] S. S. Verbridge *et al.*, "High quality factor resonance at room temperature with nanostrings under high tensile stress," *Journal of Applied Physics*, vol. 99, no. 12, p. 124 304, 2006 (cit. on p. 8).

[42] R. S. Jacobsen *et al.*, "Strained silicon as a new electro-optic material," *Nature*, vol. 441, no. 7090, pp. 199–202, 2006 (cit. on p. 8).

[43] A. H. Ghadimi, "Ultra-coherent nano-mechanical resonators for quantum optomechanics at room temperature," Ph.D. dissertation, EPFL, Lausanne, 2018 (cit. on pp. 8–9).

[44] G. Anetsberger *et al.*, "Measuring nanomechanical motion with an imprecision below the standard quantum limit," *Phys. Rev. A*, vol. 82, no. 6, p. 061 804, 2010 (cit. on p. 8).

[45] J. Huber *et al.*, "Spectral Evidence of Squeezing of a Weakly Damped Driven Nanomechanical Mode," *Phys. Rev. X*, vol. 10, no. 2, p. 021 066, 2020 (cit. on p. 8).

[46] K. Makles *et al.*, “2d photonic-crystal optomechanical nanoresonator,” *Opt. Lett.*, vol. 40, no. 2, pp. 174–177, 2015 (cit. on p. 8).

[47] X. Chen *et al.*, “High-finesse Fabry–Perot cavities with bidimensional Si3N4 photonic-crystal slabs,” *Light: Science & Applications*, vol. 6, no. 1, e16190–e16190, 2017 (cit. on p. 8).

[48] C. Reinhardt *et al.*, “Ultralow-noise sin trampoline resonators for sensing and optomechanics,” *Phys. Rev. X*, vol. 6, p. 021 001, 2 2016 (cit. on p. 8).

[49] C. H. Bui *et al.*, “High-reflectivity, high-q micromechanical membranes via guided resonances for enhanced optomechanical coupling,” *Applied Physics Letters*, vol. 100, no. 2, p. 021 110, 2012 (cit. on p. 8).

[50] R. A. Norte, J. P. Moura, and S. Gröblacher, “Mechanical resonators for quantum optomechanics experiments at room temperature,” *Phys. Rev. Lett.*, vol. 116, p. 147 202, 14 2016 (cit. on p. 8).

[51] T. P. Purdy, R. W. Peterson, and C. A. Regal, “Observation of radiation pressure shot noise on a macroscopic object,” *Science*, vol. 339, no. 6121, pp. 801–804, 2013 (cit. on p. 8).

[52] L. G. Villanueva and S. Schmid, “Evidence of surface loss as ubiquitous limiting damping mechanism in sin micro- and nanomechanical resonators,” *Phys. Rev. Lett.*, vol. 113, p. 227 201, 22 2014 (cit. on p. 8).

[53] Y. Tsaturyan *et al.*, “Ultracoherent nanomechanical resonators via soft clamping and dissipation dilution,” *Nature Nanotech*, vol. 12, no. 8, pp. 776–783, 2017 (cit. on p. 8).

[54] D. Mason *et al.*, “Continuous force and displacement measurement below the standard quantum limit,” *Nature Physics*, vol. 15, no. 8, pp. 745–749, 2019 (cit. on p. 8).

[55] I. Galinskiy *et al.*, “Phonon counting thermometry of an ultracoherent membrane resonator near its motional ground state,” *Optica*, vol. 7, no. 6, pp. 718–725, 2020 (cit. on p. 8).

[56] A. H. Ghadimi *et al.*, “Elastic strain engineering for ultralow mechanical dissipation,” *Science*, vol. 360, no. 6390, pp. 764–768, 2018 (cit. on p. 9).

[57] L. Sementilli, E. Romero, and W. P. Bowen, “Nanomechanical Dissipation and Strain Engineering,” *Advanced Functional Materials*, vol. 32, no. 3, p. 2 105 247, 2022 (cit. on p. 9).

[58] M. Croquette *et al.*, “Recent advances toward mesoscopic quantum optomechanics,” *AVS Quantum Sci.*, vol. 5, no. 1, p. 014 403, 2023 (cit. on p. 9).

[59] F. J. Giessibl, “The qPlus sensor, a powerful core for the atomic force microscope,” *Review of Scientific Instruments*, vol. 90, no. 1, p. 011 101, 2019 (cit. on p. 9).

[60] F. J. Giessibl, “Atomic Resolution of the Silicon (111)-(7×7) Surface by Atomic Force Microscopy,” *Science*, vol. 267, no. 5194, pp. 68–71, 1995 (cit. on p. 9).

[61] M. Emmrich *et al.*, "Subatomic resolution force microscopy reveals internal structure and adsorption sites of small iron clusters," *Science*, vol. 348, no. 6232, pp. 308–311, 2015 (cit. on p. 9).

[62] M. Ternes *et al.*, "The Force Needed to Move an Atom on a Surface," *Science*, vol. 319, no. 5866, pp. 1066–1069, 2008 (cit. on p. 9).

[63] L. Gross *et al.*, "The Chemical Structure of a Molecule Resolved by Atomic Force Microscopy," *Science*, vol. 325, no. 5944, pp. 1110–1114, 2009 (cit. on p. 9).

[64] J. Welker and F. J. Giessibl, "Revealing the Angular Symmetry of Chemical Bonds by Atomic Force Microscopy," *Science*, vol. 336, no. 6080, pp. 444–449, 2012 (cit. on p. 9).

[65] K. Pürckhauer *et al.*, "Imaging in Biologically-Relevant Environments with AFM Using Stiff qPlus Sensors," *Sci Rep*, vol. 8, no. 1, p. 9330, 2018 (cit. on p. 9).

[66] M. Allegrini *et al.*, "Laser thermal effects on atomic force microscope cantilevers," *Ultramicroscopy*, vol. 42-44, pp. 371–378, 1992 (cit. on p. 9).

[67] O. Marti *et al.*, "Mechanical and thermal effects of laser irradiation on force microscope cantilevers," *Ultramicroscopy*, vol. 42-44, pp. 345–350, 1992 (cit. on p. 9).

[68] D. Ramos *et al.*, "Photothermal excitation of microcantilevers in liquids," *Journal of Applied Physics*, vol. 99, no. 12, p. 124 904, 2006 (cit. on p. 9).

[69] D. Kiracofe *et al.*, "High efficiency laser photothermal excitation of microcantilever vibrations in air and liquids," *Review of Scientific Instruments*, vol. 82, no. 1, p. 013 702, 2011 (cit. on p. 9).

[70] B. A. Bircher *et al.*, "Photothermal excitation of microcantilevers in liquid: Effect of the excitation laser position on temperature and vibrational amplitude," *Micro & Nano Letters*, vol. 8, no. 11, pp. 770–774, 2013 (cit. on p. 9).

[71] M. Geitner *et al.*, "Low thermal fluctuations in a system heated out of equilibrium," *Phys. Rev. E*, vol. 95, no. 3, p. 032 138, 2017 (cit. on pp. 9, 13, 41–42, 44, 54, 61, 87, 130).

[72] B. Pottier *et al.*, "Silicon cantilevers locally heated from 300 K up to the melting point: Temperature profile measurement from their resonances frequency shift," *Journal of Applied Physics*, vol. 129, no. 18, p. 184 503, 2021 (cit. on pp. 9, 13, 54, 87, 130).

[73] A. Fontana and L. Bellon, "Linking fluctuation and dissipation in spatially extended out-of-equilibrium systems," *Phys. Rev. E*, vol. 107, no. 3, p. 034 118, 2023 (cit. on pp. 9, 54, 87, 133).

[74] J. Moser *et al.*, "Ultrasensitive force detection with a nanotube mechanical resonator," *Nature Nanotechnology*, vol. 8, 493 EP –, 2013 (cit. on p. 9).

[75] S. Stapfner *et al.*, "Cavity-enhanced optical detection of carbon nanotube Brownian motion," *Applied Physics Letters*, vol. 102, no. 15, p. 151 910, 2013 (cit. on p. 9).

[76] A. W. Barnard *et al.*, "Fluctuation broadening in carbon nanotube resonators," *Proceedings of the National Academy of Sciences*, vol. 109, no. 47, pp. 19 093–19 096, 2012 (cit. on p. 9).

[77] J. Moser *et al.*, "Nanotube mechanical resonators with quality factors of up to 5 million," *Nature Nanotechnology*, vol. 9, 1007 EP –, 2014 (cit. on p. 9).

[78] S. L. de Bonis *et al.*, "Ultrasensitive Displacement Noise Measurement of Carbon Nanotube Mechanical Resonators," *Nano Letters*, vol. 18, no. 8, pp. 5324–5328, 2018 (cit. on p. 9).

[79] J. Chaste *et al.*, "A nanomechanical mass sensor with yoctogram resolution," *Nature Nanotech*, vol. 7, no. 5, pp. 301–304, 2012 (cit. on p. 9).

[80] G. Gruber *et al.*, "Mass Sensing for the Advanced Fabrication of Nanomechanical Resonators," *Nano Letters*, vol. 19, no. 10, pp. 6987–6992, 2019 (cit. on p. 10).

[81] A. Tavernarakis *et al.*, "Optomechanics with a hybrid carbon nanotube resonator," *Nat Commun*, vol. 9, no. 1, p. 662, 2018 (cit. on p. 10).

[82] K. J. Vahala, "Optical microcavities," *Nature*, vol. 424, no. 6950, pp. 839–846, 2003 (cit. on p. 10).

[83] J. Hofer, A. Schliesser, and T. J. Kippenberg, "Cavity optomechanics with ultrahigh-Q crystalline microresonators," *Phys. Rev. A*, vol. 82, p. 031 804, 3 2010 (cit. on p. 10).

[84] L. Ding *et al.*, "Wavelength-sized gaas optomechanical resonators with gigahertz frequency," *Applied Physics Letters*, vol. 98, no. 11, p. 113 108, 2011 (cit. on p. 10).

[85] R. Ma *et al.*, "Radiation-pressure-driven vibrational modes in ultrahigh-q silica microspheres," *Opt. Lett.*, vol. 32, no. 15, pp. 2200–2202, 2007 (cit. on pp. 10, 32).

[86] Y.-S. Park and H. Wang, "Resolved-sideband and cryogenic cooling of an optomechanical resonator," *Nature Phys*, vol. 5, no. 7, pp. 489–493, 2009 (cit. on p. 10).

[87] M. Tomes and T. Carmon, "Photonic micro-electromechanical systems vibrating at X-band (11-ghz) rates," *Phys. Rev. Lett.*, vol. 102, p. 113 601, 11 2009 (cit. on p. 10).

[88] D. K. Armani *et al.*, "Ultra-high-Q toroid microcavity on a chip," *Nature*, vol. 421, no. 6926, pp. 925–928, 2003 (cit. on p. 10).

[89] T. J. Kippenberg, S. M. Spillane, and K. J. Vahala, "Demonstration of ultra-high-Q small mode volume toroid microcavities on a chip," *Applied Physics Letters*, vol. 85, no. 25, pp. 6113–6115, 2004 (cit. on p. 10).

[90] T. Carmon *et al.*, "Temporal behavior of radiation-pressure-induced vibrations of an optical microcavity phonon mode," *Phys. Rev. Lett.*, vol. 94, p. 223 902, 22 2005 (cit. on p. 10).

[91] A. Schliesser *et al.*, "Resolved-sideband cooling of a micromechanical oscillator," *Nature Phys*, vol. 4, no. 5, pp. 415–419, 2008 (cit. on p. 10).

[92] H. Fan *et al.*, "Controllable coupling between an ultra-high-q microtoroid cavity and a graphene monolayer for optical filtering and switching applications," *Opt. Express*, vol. 28, no. 6, pp. 7906–7916, 2020 (cit. on p. 10).

[93] H. S. Dutta *et al.*, "Coupling light in photonic crystal waveguides: A review," *Photonics and Nanostructures - Fundamentals and Applications*, vol. 20, pp. 41–58, 2016 (cit. on p. 10).

[94] T. F. Krauss, "Slow light in photonic crystal waveguides," *Journal of Physics D: Applied Physics*, vol. 40, no. 9, pp. 2666–2670, 2007 (cit. on p. 10).

[95] T. Stomeo *et al.*, "Fabrication of force sensors based on two-dimensional photonic crystal technology," *Microelectronic Engineering*, vol. 84, no. 5, pp. 1450–1453, 2007 (cit. on p. 10).

[96] J. Garcia-Rupérez *et al.*, "Label-free antibody detection using band edge fringes in soi planar photonic crystal waveguides in the slow-light regime," *Opt. Express*, vol. 18, no. 23, pp. 24 276–24 286, 2010 (cit. on p. 10).

[97] Y. Akahane *et al.*, "High-Q photonic nanocavity in a two-dimensional photonic crystal," *Nature*, vol. 425, no. 6961, pp. 944–947, 2003 (cit. on p. 10).

[98] A. H. Safavi-Naeini *et al.*, "Optomechanics in an ultrahigh-q two-dimensional photonic crystal cavity," *Applied Physics Letters*, vol. 97, no. 18, p. 181 106, 2010 (cit. on p. 10).

[99] E. Gavartin *et al.*, "Optomechanical coupling in a two-dimensional photonic crystal defect cavity," *Phys. Rev. Lett.*, vol. 106, p. 203 902, 20 2011 (cit. on p. 10).

[100] H. Ren *et al.*, "Two-dimensional optomechanical crystal cavity with high quantum cooperativity," *Nat Commun*, vol. 11, no. 1, p. 3373, 2020 (cit. on p. 10).

[101] H. Ren *et al.*, "Topological phonon transport in an optomechanical system," *Nat Commun*, vol. 13, no. 1, p. 3476, 2022 (cit. on p. 10).

[102] R. Burgwal and E. Verhagen, *Enhanced nonlinear optomechanics in a coupled-mode photonic crystal device*, 2022 (cit. on p. 10).

[103] E Buks and M. L Roukes, "Metastability and the Casimir effect in micromechanical systems," *Europhys. Lett.*, vol. 54, no. 2, pp. 220–226, 2001 (cit. on p. 11).

[104] E. Buks and M. L. Roukes, "Stiction, adhesion energy, and the Casimir effect in micromechanical systems," *Phys. Rev. B*, vol. 63, no. 3, p. 033 402, 2001 (cit. on p. 11).

[105] A. Niguès, A. Siria, and P. Verlot, "Dynamical backaction cooling with free electrons," *Nat Commun*, vol. 6, no. 1, p. 8104, 2015 (cit. on pp. 11–13, 28, 44–46, 48, 56, 60, 87, 97–98).

[106] I. Tsioutsios *et al.*, "Real-Time Measurement of Nanotube Resonator Fluctuations in an Electron Microscope," *Nano Lett.*, vol. 17, no. 3, pp. 1748–1755, 2017 (cit. on pp. 11, 96).

[107] S. Pairis *et al.*, "Shot-Noise-Limited Nanomechanical Detection and Radiation Pressure Backaction from an Electron Beam," *Phys. Rev. Lett.*, vol. 122, no. 8, p. 083 603, 2019 (cit. on pp. 11, 28, 45, 49–51, 60, 77, 86–87).

[108] T. Liu *et al.*, "Visualization of Subatomic Movements in Nanostructures," *Nano Lett.*, vol. 21, no. 18, pp. 7746–7752, 2021 (cit. on p. 11).

[109] F. Aguilar Sandoval *et al.*, "Resonance frequency shift of strongly heated micro-cantilevers," *Journal of Applied Physics*, vol. 117, no. 23, p. 234 503, 2015 (cit. on pp. 13, 41, 54, 87, 130).

[110] D. W. Ricker, *Echo Signal Processing*. 2003 (cit. on p. 17).

[111] A. N. Cleland, *Foundations of Nanomechanics* (Advanced Texts in Physics). Berlin, Heidelberg, 2003 (cit. on pp. 18, 33, 36, 129).

[112] H. B. Callen and T. A. Welton, "Irreversibility and generalized noise," *Phys. Rev.*, vol. 83, pp. 34–40, 1 1951 (cit. on p. 19).

[113] R. K. Pathria, *Statistical Mechanics*. 1972 (cit. on p. 20).

[114] T. Briant *et al.*, "Optical phase-space reconstruction of mirror motion at the attometer level," *Eur. Phys. J. D*, vol. 22, no. 1, pp. 131–140, 2003 (cit. on pp. 25, 27–28, 95).

[115] E. Gavartin, P. Verlot, and T. J. Kippenberg, "Stabilization of a linear nanomechanical oscillator to its thermodynamic limit," *Nat Commun*, vol. 4, no. 1, p. 2860, 2013 (cit. on pp. 25–26).

[116] S. Etaki *et al.*, "Self-sustained oscillations of a torsional SQUID resonator induced by Lorentz-force back-action," *Nat Commun*, vol. 4, no. 1, p. 1803, 2013 (cit. on pp. 26, 97).

[117] J. Cripe *et al.*, "Measurement of quantum back action in the audio band at room temperature," *Nature*, vol. 568, no. 7752, pp. 364–367, 2019 (cit. on p. 28).

[118] A. Naik *et al.*, "Cooling a nanomechanical resonator with quantum backaction," *Nature*, vol. 443, no. 7108, pp. 193–196, 2006 (cit. on p. 28).

[119] M. L. Juan *et al.*, "Self-induced back-action optical trapping of dielectric nanoparticles," *Nature Phys*, vol. 5, no. 12, pp. 915–919, 2009 (cit. on p. 28).

[120] J. Chan *et al.*, "Laser cooling of a nanomechanical oscillator into its quantum ground state," *Nature*, vol. 478, no. 7367, pp. 89–92, 2011 (cit. on p. 32).

[121] L. Meirovitch, *Elements of Vibration analysis.* New York, 1975 (cit. on p. 37).

[122] M. Pinard, Y. Hadjar, and A. Heidmann, "Effective mass in quantum effects of radiation pressure," *Eur. Phys. J. C*, vol. 7, no. 1, pp. 107–111, 1999 (cit. on p. 37).

[123] P. Paolino and L. Bellon, "Frequency dependence of viscous and viscoelastic dissipation in coated micro-cantilevers from noise measurement," *Nanotechnology*, vol. 20, no. 40, p. 405 705, 2009 (cit. on p. 39).

[124] K. Yamamoto *et al.*, "Experimental study of thermal noise caused by an inhomogeneously distributed loss," *Physics Letters A*, vol. 280, no. 5, pp. 289–296, 2001 (cit. on p. 39).

[125] K. Yamamoto *et al.*, "Study of the thermal noise caused by inhomogeneously distributed loss," *Class. Quantum Grav.*, vol. 19, no. 7, p. 1689, 2002 (cit. on p. 39).

[126] D. M. Photiadis and J. A. Judge, "Attachment losses of high Q oscillators," *Applied Physics Letters*, vol. 85, no. 3, pp. 482–484, 2004 (cit. on p. 40).

[127] R. Lifshitz and M. L. Roukes, "Thermoelastic damping in micro- and nanomechanical systems," *Phys. Rev. B*, vol. 61, no. 8, pp. 5600–5609, 2000 (cit. on p. 40).

[128] S. Kasas *et al.*, "Detecting nanoscale vibrations as signature of life," *Proceedings of the National Academy of Sciences*, vol. 112, no. 2, pp. 378–381, 2015 (cit. on p. 41).

[129] E. Dieterich *et al.*, "Single-molecule measurement of the effective temperature in non-equilibrium steady states," *Nature Phys*, vol. 11, no. 11, pp. 971–977, 2015 (cit. on p. 41).

[130] L. Bellon, S. Ciliberto, and C. Laroche, "Violation of the fluctuation-dissipation relation during the formation of a colloidal glass," *EPL*, vol. 53, no. 4, p. 511, 2001 (cit. on p. 41).

[131] D. Loi, S. Mossa, and L. F. Cugliandolo, "Non-conservative forces and effective temperatures in active polymers," *Soft Matter*, vol. 7, no. 21, pp. 10 193–10 209, 2011 (cit. on p. 41).

[132] L. Conti *et al.*, "Effects of breaking vibrational energy equipartition on measurements of temperature in macroscopic oscillators subject to heat flux," *J. Stat. Mech.*, vol. 2013, no. 12, P12003, 2013 (cit. on p. 41).

[133] J. M. Nichol *et al.*, "Displacement detection of silicon nanowires by polarization-enhanced fiber-optic interferometry," *Applied Physics Letters*, vol. 93, no. 19, p. 193 110, 2008 (cit. on p. 49).

[134] M. Liu, L. Xu, and X. Lin, "Heating effect of electron beam bombardment," *Scanning*, vol. 16, no. 1, pp. 1–5, 1994 (cit. on p. 54).

[135] S. Zaitsev, O. Shtempluck, and E. Buks, "Effects of electron beam induced carbon deposition on the mechanical properties of a micromechanical oscillator," *Sensors and Actuators A: Physical*, vol. 179, pp. 237–241, 2012 (cit. on p. 54).

[136] H. J. Yang *et al.*, "Thermodynamic patterns during in-situ heating of InAs nanowires encapsulated in Al2O3 shells," *Nanotechnology*, vol. 33, no. 2, p. 025 702, 2021 (cit. on pp. 54, 69, 83).

[137] A. Ul-Hamid, *A Beginners' Guide to Scanning Electron Microscopy*. Cham, 2018 (cit. on pp. 56, 61, 67, 128).

[138] A.-H. Chen, "Croissance et caractérisation de nanofils coeur/coquille semiconducteur/supraconducteur pour les technologies quantiques," Ph.D. dissertation, Université Grenoble Alpes, Grenoble, 2022 (cit. on p. 58).

[139] R. S. Wagner and W. C. Ellis, "Vapor-liquid-solid mechanism of single crystal growth," *Appl. Phys. Lett.*, vol. 4, no. 5, pp. 89–90, 1964 (cit. on p. 58).

[140] W. Zhou *et al.*, "Fundamentals of Scanning Electron Microscopy (SEM)," in *Scanning Microscopy for Nanotechnology: Techniques and Applications*, W. Zhou and Z. L. Wang, Eds., New York, NY, 2007, pp. 1–40 (cit. on p. 61).

[141] K. Lahcen and M. Christian, *La microscopie électronique à balayage sous environnement gazeux (MEB-EG) - Du principe à l'étude optimisée des matériaux*. Paris, 2017 (cit. on p. 61).

[142] "Fundamentals of real-time spectrum analysis," Tektronix, https://www.tek.com/en/doc
real-time-spectrum-analysis, Primer 37W-17249-5, 2015 (cit. on p. 71).

[143] A. Oppenheim and R. Schafer, "Discrete-time signal processing," in 1989, p. 474 (cit. on p. 73).

[144] F. Zhou *et al.*, "Thermal conductivity of indium arsenide nanowires with wurtzite and zinc blende phases," *Phys. Rev. B*, vol. 83, no. 20, p. 205 416, 2011 (cit. on p. 88).

[145] M. O. Scully and M. S. Zubairy, *Quantum Optics*. Cambridge, 1997 (cit. on p. 97).

[146] T. Lee and A. Hajimiri, "Oscillator phase noise: A tutorial," *IEEE Journal of Solid-State Circuits*, vol. 35, no. 3, pp. 326–336, 2000 (cit. on p. 103).

[147] D. Ham and A. Hajimiri, "Virtual damping and Einstein relation in oscillators," *IEEE Journal of Solid-State Circuits*, vol. 38, no. 3, pp. 407–418, 2003 (cit. on p. 103).

[148] D. Leeson, "A simple model of feedback oscillator noise spectrum," *Proceedings of the IEEE*, vol. 54, no. 2, pp. 329–330, 1966 (cit. on p. 103).

[149] M. Bertolotti *et al.*, "New photothermal deflection method for thermal diffusivity measurement of semiconductor wafers," *Review of Scientific Instruments*, vol. 68, no. 3, pp. 1521–1526, 1997 (cit. on p. 110).

[150] S. Soumya *et al.*, "Thermal diffusivity of molybdenum oxide nanowire film: A photothermal beam deflection study," *Optics & Laser Technology*, vol. 139, p. 106 993, 2021 (cit. on p. 110).

[151] L. Arnoldi *et al.*, "Thermal diffusivity of diamond nanowires studied by laser assisted atom probe tomography," *Appl. Phys. Lett.*, vol. 112, no. 14, p. 143 104, 2018 (cit. on p. 110).

[152] A. K. Hüttel *et al.*, "Carbon Nanotubes as Ultrahigh Quality Factor Mechanical Resonators," *Nano Lett.*, vol. 9, no. 7, pp. 2547–2552, 2009 (cit. on p. 116).

[153] W.-C. Li *et al.*, "Quality factor enhancement in micromechanical resonators at cryogenic temperatures," in *TRANSDUCERS 2009 - 2009 International Solid-State Sensors, Actuators and Microsystems Conference*, 2009, pp. 1445–1448 (cit. on p. 116).

[154] A. R. Degheidy *et al.*, "Temperature dependence of phonons and related crystal properties in InAs, InP and InSb zinc-blende binary compounds," *Computational Condensed Matter*, vol. 16, e00308, 2018 (cit. on p. 116).

[155] O. Bourgeois *et al.*, "Reduction of phonon mean free path: From low-temperature physics to room temperature applications in thermoelectricity," *Comptes Rendus Physique*, Mesoscopic thermoelectric phenomena / Phénomènes thermoélectriques mésoscopiques, vol. 17, no. 10, pp. 1154–1160, 2016 (cit. on p. 116).

[156] P.-L. de Assis *et al.*, "Strain-Gradient Position Mapping of Semiconductor Quantum Dots," *Phys. Rev. Lett.*, vol. 118, no. 11, p. 117 401, 2017 (cit. on p. 119).

[157] P. Yuan *et al.*, "Adapting the Electron Beam from SEM as a Quantitative Heating Source for Nanoscale Thermal Metrology," *Nano Lett.*, vol. 20, no. 5, pp. 3019–3029, 2020 (cit. on p. 119).

[158] S. Pairis, "Chemical and physical characterization using scanning electron microscopy and electron probe microanalysis," 2019 (cit. on p. 121).

[159] R. F. Egerton, P. Li, and M. Malac, "Radiation damage in the TEM and SEM," *Micron*, International Wuhan Symposium on Advanced Electron Microscopy, vol. 35, no. 6, pp. 399–409, 2004 (cit. on p. 128).

[160] F. Fang *et al.*, "Towards atomic and close-to-atomic scale manufacturing," *Int. J. Extrem. Manuf.*, vol. 1, no. 1, p. 012 001, 2019 (cit. on p. 128).

[161] H. Nykänen *et al.*, "Low energy electron beam induced damage on gallium nitride based materials," *physica status solidi c*, vol. 9, no. 7, pp. 1563–1565, 2012 (cit. on p. 128).

[162] N. Tanaka, H. K. H. Kawanishi, and T. I. T. Ishikawa, "Photoluminescence Study of Electron-Beam-Induced Damage in GaAs/AlGaAs Quantum-Well Structures," *Jpn. J. Appl. Phys.*, vol. 32, no. 1S, p. 540, 1993 (cit. on p. 128).

[163] H. Gu *et al.*, "Considerable knock-on displacement of metal atoms under a low energy electron beam," *Sci Rep*, vol. 7, no. 1, p. 184, 2017 (cit. on p. 128).

[164] L. Hobbs, "Murphy's Law and the Uncertainty of Electron Probes," *Scanning Microscopy*, vol. 1990, no. 4, 1990 (cit. on p. 128).

[165] L. Philippe *et al.*, "Nanomechanics of rhenium wires: Elastic modulus, yield strength and strain hardening," *Acta Materialia*, vol. 57, no. 14, pp. 4032–4035, 2009 (cit. on p. 129).

Appendices

Appendix A

Mode temperature for reduced input power

In this section we provide the result of the calculation presented in section 4.2.1, adapted for the input power and geometry of the experimental results of section 4.2, i.e. $P = 18$ nW, $D = 67$ nm and $L = 8.3$ um.

Figure A.1 show the local temperature gradient $\Delta T(y) = T(y) - T_{amb}$, where T_{amb} is the ambient temperature. In this conditions, a gradient of only $\simeq 10$ K is expected, in stark contrast with the experimental result of 4.2. The effect is even smaller on the mode temperature T_1 for the first flexural mode, as shown in fig. A.2: it increases by less than 2 K with respect to the ambient temperature $T_{amb} = 295$ K.

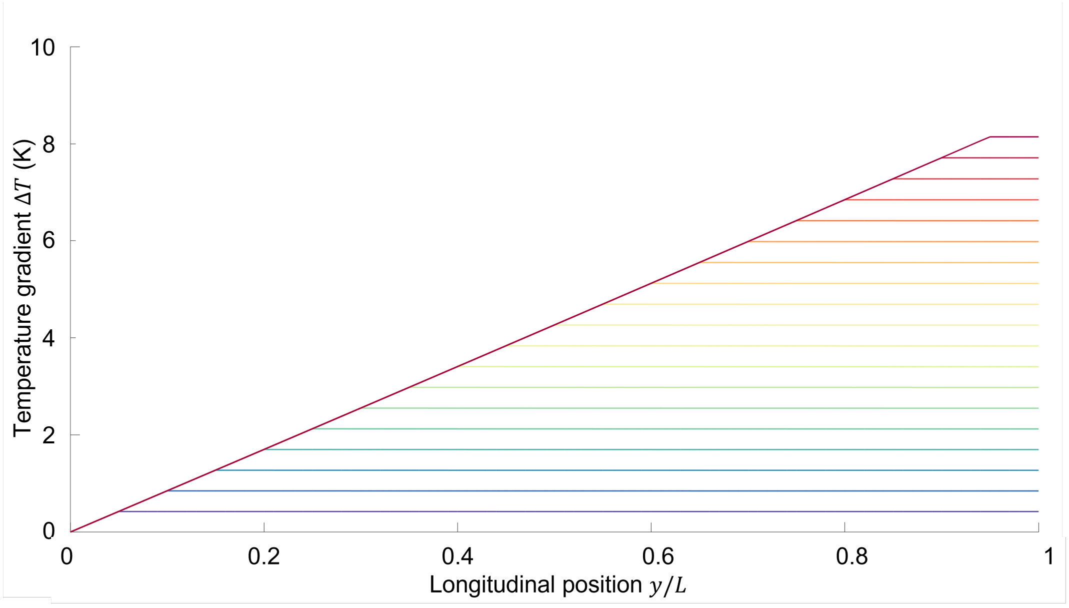

Figure A.1: Temperature profile with an input power $P = 18$ nW, for a Wurtzite-phased InAs nanowire, of length $L = 8.3$ um and diameter $D = 67$ nm. The position of the heating source is varied from $y_0/L = 0.05$ (purple curve) to $y_0/L = 0.95$ (red curve).

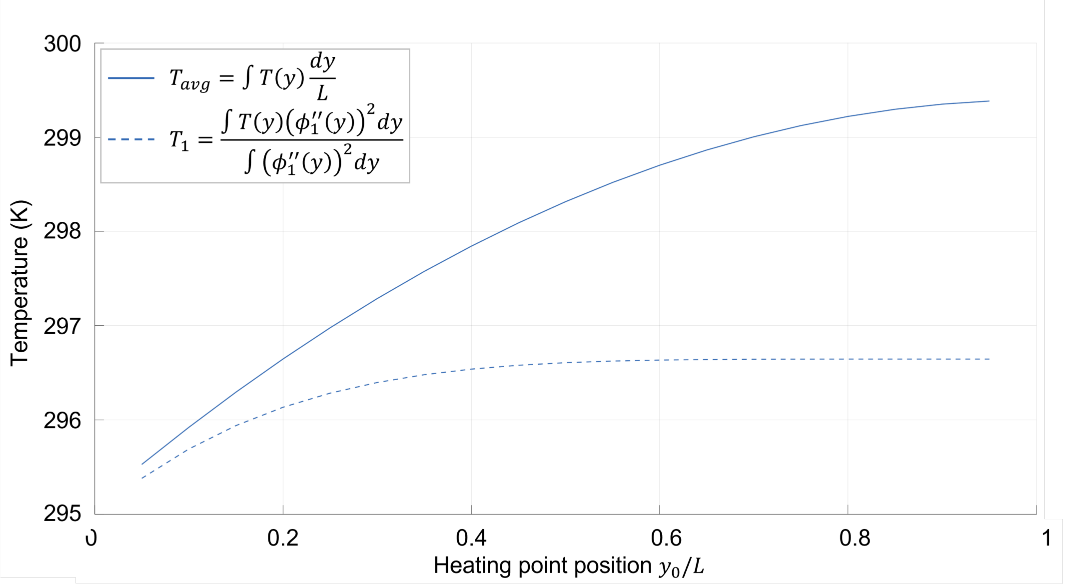

Figure A.2: Average temperature (solid line) and mode temperature for the first flexural mode (dashed line) of an InAs nanowire, of length $L = 8.3$ um and diameter $D = 67$ nm, with an incident power $P = 18$ nW.

Appendix B

Additional data on self-sustained oscillation

In this section we provide the data for another nanowire undergoing self-sustained oscillations. The nanowire is 9.66 um long, and the measurement point is at 43 % of its length (see fig. B.1a). With the same protocol as in 4.3.1, we measured the quadratures of the displacement of the nanowire. The acquisition time is 473 ms.

Figure B.1a-b show the trajectory of the motion in phase space and the histogram of the trajectory. Contrary to the results presented in section 4.3.1, the limit circle is fully explored. This suggests that the measurement time t_{meas} is longer than the characteristic time of the phase diffusion t_{phase}. Figure B.1d shows the histogram of the amplitude of the trajectory in phase space, $|X| = \sqrt{I^2 + Q^2}$, i.e. the thickness of the trace along the limit circle, and a Gaussian fit to this histogram, in very good agreement.

To confirm this result, we study the phase diffusion. We extract the phase from the quadratures of motion and perform a $1/f^2$ fit according to eq. (4.24). The result is presented in fig. B.2 and shows an excellent agreement with the data, yielding a diffusion constant $D \simeq 22.5$ s^{-1}. We can then calculate the characteristic time as $t_{phase} = 1/D \simeq 44.5$ ms, which is approximately 10 times smaller than the measurement time and explains why the limit circle is complete in this acquisition.

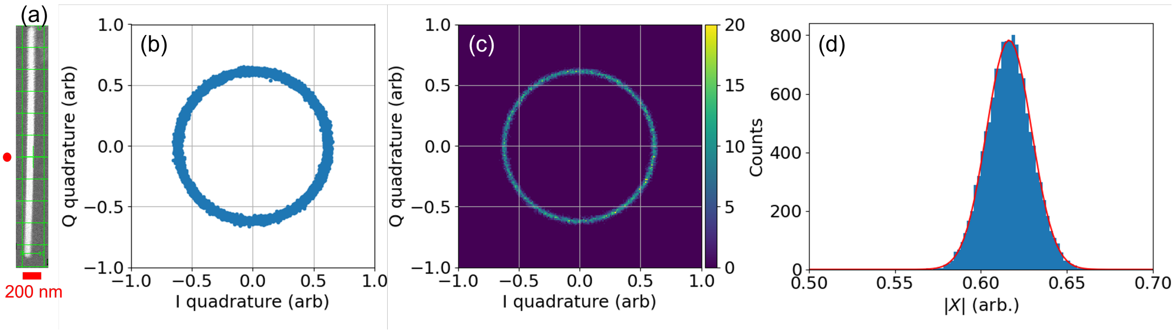

Figure B.1: (a) Micrograph of another nanowire undergoing self-sustained oscillations when the electron beam is placed at $\simeq 43$ % of its length (red dot). (b) Trajectory and (c) histogram of the trajectory of the motion in phase space, revealing the limit circle, which is fully explored by the system during the acquisition time $t_{meas} = 473$ ms. (d) Histogram of the amplitude of the displacement. The red line is a Gaussian fit, in excellent agreement.

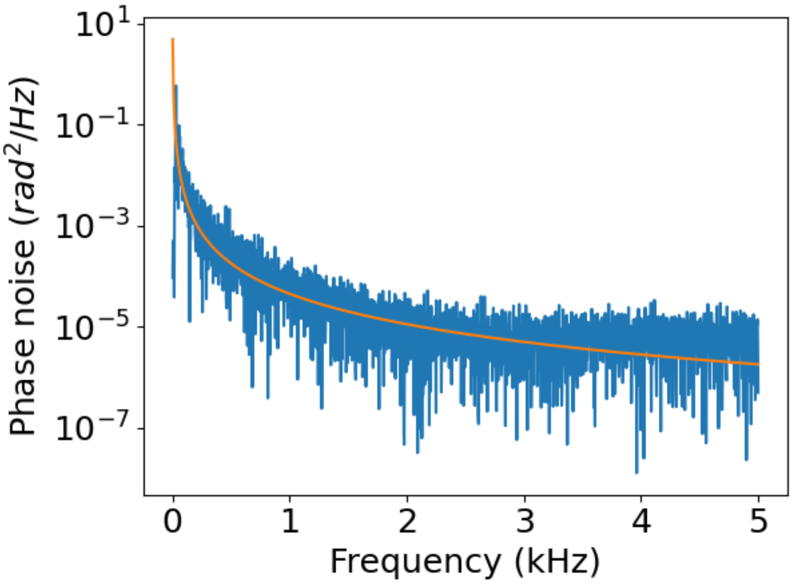

Figure B.2: Power Spectral Density of the phase of the motion (blue). The orange curve is a $1/f^2$ fit to the data, in excellent agreement, yielding a diffusion constant $D \simeq 22.5$ s^{-1}.